A COMPARISON OF THE CORROSION PRODUCTS AND MECHANISMS OF VARIOUS FORMS OF DEPOSIT-INDUCED CORROSION AT 700^{o}C

by

Bradley Scott Lutz

B.S. Materials Science and Engineering, Purdue University, 2009

Submitted to the Graduate Faculty of

The Swanson School of Engineering in partial fulfillment

of the requirements for the degree of

Master of Science

University of Pittsburgh

2012

UNIVERSITY OF PITTSBURGH

SWANSON SCHOOL OF ENGINEERING

This thesis was presented

by

Bradley Scott Lutz

It was defended on

September 12, 2012

and approved by

Brian Gleeson, Ph.D., Professor, Department of Mechanical Engineering and Materials Science

Jung-Kun Lee, Ph.D., Assistant Professor, Department of Mechanical Engineering and Materials Science

Thesis Co-Advisor: Frederick S. Pettit, Ph.D., Professor Emeritus, Department of Mechanical Engineering and Materials Science

Thesis Co-Advisor: Gerald H. Meier, Ph.D., Professor, Department of Mechanical Engineering and Materials Science

A COMPARISON OF THE CORROSION PRODUCTS AND MECHANISMS OF VARIOUS FORMS OF DEPOSIT-INDUCED CORROSION AT 700°C

Bradley Scott Lutz, M.S.

University of Pittsburgh, 2012

Tests were performed on selected steel and Ni-based alloys in simulated fireside corrosion conditions with synthetic coal ash deposits. The tests provide fireside corrosion information as well as insights on corrosion mechanisms for guiding materials development. General mechanisms for the different types of hot corrosion caused by Na_2SO_4 deposits were inferred; although, in some cases, specifics were unclear. Tests were also conducted on MCrAlY alloys and Ni-based disk alloys under simulated hot corrosion conditions at 700°C.

The experimental conditions simulated fireside corrosion by varying deposit compositions, temperatures, and gas atmospheres until the most severe corrosion environment was found. This was determined to be at 700°C with a deposit consisting of K_2SO_4:Na_2SO_4:Fe_2O_3 in a 1.5:1.5:1.0 molar ratio in a gas atmosphere containing oxygen with 1000ppm SO_2. Once this was determined, the effects of alloy composition on the resistance to corrosion were obtained, and a mechanism for the corrosion was deduced. An SO_2 threshold value in the gas atmosphere for severe corrosion to occur was also observed. Each of the alloys suffered corrosion in the form of pits similar to those found during Type II hot corrosion.

A variety of disk alloys typical of those used in gas turbine engines were exposed to aggressive corrosion conditions. The exposure conditions at 700°C included air oxidation, oxidation with Na_2SO_4 salt deposits in air, and O_2 + 1000ppm SO_2. The Mo-containing alloys suffered degradation with the salt deposits in air, without the presence of SO_2. The attack was

similar to alloy-induced acidic fluxing usually observed around 900^{o}C. Each of the alloys was significantly degraded under the Type II hot corrosion conditions, with the Mo-containing alloys experiencing more corrosion than the other alloys.

The corrosion products and mechanisms for the various forms of corrosion were compared. Fireside corrosion was found to be very similar to Type II hot corrosion. The Mo-containing disk alloys which were exposed in air with Na_2SO_4 salt deposits were found to undergo alloy-induced acidic fluxing even at 700^{o}C. The corrosion of the disk alloys under Type II hot corrosion conditions was found to be similar to Type II hot corrosion of NiCrAlY.

TABLE OF CONTENTS

ACKNOWLEDGEMENTS XV

1.0 INTRODUCTION 1

2.0 BACKGROUND 5

2.1 FORMATION OF DEPOSITS ON BOILER TUBES 5

2.2 FUEL 8

2.2.1 Coal 9

2.2.2 Other Types of Fuels 14

2.3 FIRESIDE CORROSION 16

2.3.1 Sulfur and Sulfates 17

2.3.1.1 Pyrosulfates 22

2.3.1.2 Alkali Iron Trisulfates 24

2.3.2 Mechanism of Corrosion 25

2.3.2.1 Gas-Phase Oxidation 26

2.3.2.2 Liquid-Phase Corrosion 29

2.3.3 Alloys For Use in Boilers and Gas Turbine Hardware 38

2.4 SODIUM SULFATE-INDUCED HOT CORROSION 44

2.4.1 Stages of Corrosion 45

2.4.1.1 Initiation Stage 47

2.4.1.2 Propagation Stage 50
2.4.2 Type I Hot Corrosion 57
2.4.2.1 Basic Fluxing 57
2.4.2.2 Alloy-Induced Acidic Fluxing 64
2.4.3 Type II Hot Corrosion 68
2.4.3.1 Gas-Phase Induced Acidic Fluxing 68
2.4.4 Disk Corrosion 76
3.0 RESEARCH OBJECTIVES 78
4.0 EXPERIMENTAL PROCEDURE 80
4.1 MATERIALS PREPARATION 80
4.2 FIRESIDE CORROSION TESTS 82
4.3 TYPE II HOT CORROSION TESTS 85
4.4 ANALYTICAL PROCEDURE 86
5.0 RESULTS AND DISCUSSION 88
5.1 FIRESIDE CORROSION 88
5.1.1 Initial Tests: Finding the right corrosion environment 88
5.1.1.1 Slurry Coating Deposition Tests 88
5.1.1.2 Powder-Crucible Deposition Tests 90
5.1.2 FeNiCr 103
5.1.3 T92 106
5.1.4 Ni-Cr 109
5.1.5 IN-617 114
5.1.6 NiCrAl 117

5.1.7 NiCrAlMo 119

5.2 TYPE II HOT CORROSION 121

5.3 TYPE II HOT CORROSION OF DISK ALLOYS 125

5.3.1 Oxidation of Alloys in Air 125

5.3.2 Oxidation of Alloys in Air with Na_2SO_4 Deposit 127

5.3.3 Type II Hot Corrosion of Disk Alloys 129

5.4 COMPARISON OF THE CORROSION MICROSTRUCTURES AND MECHANSIMS 132

5.4.1 Fireside Corrosion and Type II Hot Corrosion 133

5.4.2 Corrosion of Mo-Containing Disk Alloys in Air and Alloy-Induced Acidic Fluxing Type I Hot Corrosion 137

5.4.3 Corrosion of Disk Alloys in SO_2 and Type II Hot Corrosion 140

5.5 CONCLUSIONS 142

BIBLIOGRAPHY 146

LIST OF TABLES

Table 1: Elemental Analysis of Major Fuel (wt%) 10

Table 2: Occurance of Minerals in Coal 11

Table 3: Reactions in the Oxidation of Sulfur 19

Table 4: Melting Point of Complex Sulfates 24

Table 5: Nominal Alloy Compositions 80

Table 6: Equilibrium SO_3 Partial Pressures at Experimental Temperatures and Gas Atmospheres 84

Table 7: Comparison of the Characteristics, Corrosion Products, and Mechanisms for Each Type of Corrosion Tested 133

LIST OF FIGURES

Figure 1: Schematic of oxy-fuel combustion 2

Figure 2: Rate of Change of Heat Flux with Accumulation of Slag 6

Figure 3: Deposits and Corrosion Area for Typical Reheater Tube 8

Figure 4: Calculated Flue Gas Composition Upon Coal Combustion 9

Figure 5: Mineral Matter Transformation Mechanism 13

Figure 6: Calculated Molar Quantity of Pure Compounds of Condensed Phases in Equilibrium with the Flue Gas upon Combustion of 100g of the Coal Shown in Table 1 14

Figure 7. Fireside corrosion regimes in coal-fired boilers 17

Figure 8: Formation of SO_3 in Thin Stabilized Flame of H_2S-O_2-N_2 20

Figure 9: Melting Points in the System Na_2SO_4-SO_3 and K_2SO_4-SO_3 23

Figure 10: The Iron-Oxygen Phase Diagram 27

Figure 11: The General Temperature Distribution Through a Superheater Tube, the Oxide, and the Deposit 30

Figure 12: Mechanism of Fireside Corrosion of Steel Surfaces by Removal of Oxide Film to Form $K_3Fe(SO_4)_3$ 32

Figure 13: Coal-ash Corrosion Cycle 34

Figure 14: Oxidatio Kinetics of Fe-10Al Alloy exposed to O_2-0.5% (SO_2+SO_3) at 650^{o}C: (a) Na_2SO_4-K_2SO_4, (b) Na_2SO_4 alone, and (c) K_2SO_4 alone 36

Figure 15: SO_3 Levels Required to Stabilize Eutectic Melts: (a) Na_2SO_4-iron trisulfates and (b) K_2SO_4-iron trisulfates 37

Figure 16: Evolution of Ferritic Steels for Boilers 39

Figure 17: Allowable Stress for Various Classes of Alloys 41

Figure 18: Isothermal Mass Change versus time for IN-738. The data consists of an initiation stage and a propagation stage with large weight changes (dashed line gives arbitrary end of initiation stage)..... 46

Figure 19: Thermodynamic Stability Diagram for the Na-O-S system at Constant Temperature 48

Figure 20: Isothermal Stability Diagram of the Cr-O-S System Superimposed onto the Na_2SO_4 Portion of the Na-S-O Stability Diagram for T=1200K 52

Figure 21: Measured Oxide Solubilities in Na_2SO_4 at 927^oC and 1 atm O_2..... 53

Figure 22: Conditions in the Na_2SO_4 Salt the Satisfy the Rapp-Goto Criterion..... 56

Figure 23: Phase Stability Diagram for the Na-Ni-S-O System at 1000^oC 59

Figure 24: Model for Na_2SO_4-induced Accelerated Oxidation of Nickel 62

Figure 25: Comparison of Isothermal Hot Corrosion of Na_2SO_4-Coated Ni-CrAl and Ni-Cr-Al-Mo 67

Figure 26: The $CoSO_4$-Na_2SO_4 Phase Diagram..... 69

Figure 27: The SO_3 Partial Pressure Required to Form Various Species 71

Figure 28: Schematic of Horizontal Tube Furnace Apparatus for Fireside Corrosion Tests 83

Figure 29: Modified Quartz Rod for Crucible Fireside Corrosion Tests..... 85

Figure 30: Fireside Corrosion at 650^oC with Deposit D slurry coated in O_2 + 100ppm SO_2 for 100hrs for (a.) FeNiCr, (b.) IN-617, (c.) Ni-Cr, (d.) T92, and (e.) NiCrAl 89

Figure 31: Fireside corrosion at 700°C with Deposit D slurry coated in O_2 + 100ppm SO_2 for 100hrs of (a.) FeNiCr, (b.) IN-617, (c.) Ni-22Cr, (d.) T92, and (e.) NiCrAl..... 90

Figure 32: Fireside corrosion of selected alloys at 650°C with Deposit D powder in a crucible in O_2 + 100ppm SO_2 for 160hrs..... 91

Figure 33: Fireside Corrosion of Ni-22Cr at 650°C with Deposit D powder in a crucible in O_2 +100ppm SO_2 for 160 hours..... 92

Figure 34: Fireside Corrosion of (a.) Ni-22Cr and (b.) T92 at 650°C with the standard corrosion mix powder in a crucible in O_2 + 100ppm SO_2 for 100hrs..... 93

Figure 35: Fireside Corrosion of FeNiCr at 650°C with the standard corrosion mix powder in a crucible in O_2 + 100ppm SO_2 for 160 hours..... 94

Figure 36: Fireside Corrosion of FeNiCr at 700°C with the standard corrosion mix deposit in a crucible in O_2 + 100ppm SO_2 for 160 hours in 20 hour cycles..... 95

Figure 37: Fireside Corrosion of FeNiCr at 700°C in O_2 + 1000ppm SO_2 with the standard corrosion mix powder in a crucible for 160 hours isothermally..... 96

Figure 38: BSE surface SEM images of Fireside Corrosion of FeNiCr at 700°C in O_2 + 1000ppm SO_2 with the standard corrosion mix powder in a crucible for 160 hours isothermally... 97

Figure 39: BSE cross-sectional SEM images of Fireside Corrosion of FeNiCr at 700°C in O_2 + 1000ppm SO_2 with the standard corrosion mix powder in a crucible for 160 hours isothermally..... 98

Figure 40: Fireside Corrosion of FeNiCrAl at 650°C with the standard corrosion mix powder in a crucible for 160 hours in O_2 + 1000ppm SO_2..... 99

Figure 41: Oxidation of FeNiCr at 650°C in O_2 + 1000ppm SO_2 with no deposit for 160 hours..... 100

Figure 42: Fireside Corrosion of T92 at 700^{o}C with the standard corrosion mix powder in a crucible for 160 hours in 20 hour cycles in O_2 + 1000ppm SO_2 101

Figure 43: Fireside Corrosion of NiCr at 700^{o}C with the standard corrosion mix powder in a crucible for 160 hours in 20 hour cycles in O_2 + 1000ppm SO_2 101

Figure 44: Fireside Corrosion of FeNiCr at 700^{o}C with the standard corrosion mix powder in a crucible for 160 hours in O_2 + 100ppm SO_2 103

Figure 45: Fireside Corrosion of FeNiCr at 700^{o}C with the standard corrosion mix powder in a crucible for 160 hours in O_2 + 1000ppm SO_2 103

Figure 46: Fireside Corrosion of FeNiCr at 700^{o}C with the standard corrosion mix powder in a crucible for 160 hours in O_2 + 1000ppm SO_2 104

Figure 47: Fireside Corrosion of T92 at 700^{o}C with the standard corrosion mix powder in a crucible for 160 hours in O_2 + 100ppm SO_2 107

Figure 48: Fireside corrosion of T92 at 700^{o}C with the standard corrosion mix powder in a crucible for 160 hours in O_2 + 1000ppm SO_2 107

Figure 49: Fireside Corrosion of T92 at 700^{o}C with the standard corrosion mix powder in a crucible for 160 hours in O_2 + 1000ppm SO_2 108

Figure 50: Fireside Corrosion of Ni-22Cr at 700^{o}C with the standard corrosion mix powder in a crucible for 160 hours in O_2 + 100ppm SO_2 110

Figure 51: Fireside Corrosion of Ni-Cr at 700^{o}C with the standard corrosion mix powder in a crucible for 160 hours in O_2 + 1000ppm SO_2 (a) before the platinum catalyst was moved next to the hot zone and (b) after the platinum catalyst was moved next to the hot zone 110

Figure 52: Fireside Corrosion of Ni-22Cr at 700^{o}C with the standard corrosion mix powder in a crucible for 160 hours in O_2 + 1000ppm SO_2 111

Figure 53: Fireside Corrosion of Ni-22Cr at 700^{o}C with the standard corrosion mix powder in a crucible for 160 hours in O_2 + 1000ppm SO_2 112

Figure 54: Fireside Corrosion of IN-617 at 700^{o}C with the standard corrosion mix powder in a crucible for 160 hours in O_2 + 100ppm SO_2 115

Figure 55: Fireside corrosion of IN-617 at 700^{o}C with the standard corrosion mix powder in a crucible for 160 hours in O_2 + 1000ppm SO_2 115

Figure 56: Fireside corrosion of IN-617 at 700^{o}C with the standard corrosion mix powder in a crucible for 160 hours in O_2 + 1000ppm SO_2 116

Figure 57: Fireside Corrosion of NiCrAl at 700^{o}C with the standard corrosion mix powder in a crucible for 160 hours in O_2 + 100ppm SO_2 117

Figure 58: Fireside corrosion of NiCrAl at 700^{o}C with the standard corrosion mix powder in a crucible for 160 hours in O_2 + 1000ppm SO_2 117

Figure 59: Fireside corrosion of NiCrAl at 700^{o}C with the standard corrosion mix powder in a crucible for 160 hours in O_2 + 1000ppm SO_2 119

Figure 60: Fireside corrosion of NiCrAlMo at 700^{o}C with the standard corrosion mix powder in a crucible for 160 hours in O_2 + 100ppm SO_2 119

Figure 61: Fireside Corrosion of NiCrAlMo at 700^{o}C with the standard corrosion mix powder in a crucible for 160 hours in O_2 + 1000ppm SO_2 120

Figure 62: Fireside corrosion of NiCrAlMo at 700^{o}C with the standard corrosion mix powder in a crucible for 160 hours in O_2 + 1000ppm SO_2 121

Figure 63: Type II hot corrosion microstructures: (a.-b.) NiCrAlY (c.-d.) CoCrAlY [74] 122

Figure 64: Type II hot corrosion microstructure of NiCrAlY demonstrating interphase attack[74] 123

Figure 65: $NiSO_4$-Na_2SO_4 Phase Diagram 125

Figure 66: Cross-sections of selected disk alloys after oxidation in air 126

Figure 67: Oxidation of selected disk alloys in air with Na_2SO_4 deposit at 700°C 127

Figure 68: Oxidation of Mo-containing disk alloys in air with Na_2SO_4 deposit at 650°C 129

Figure 69: Type II Hot Corrosion of Disk Alloys at 700°C in O_2 + 1000ppm SO_2 130

Figure 70: Comparison of Type II hot corrosion of NiCrAlY to Fireside Corrosion of NiCrAlMo 135

Figure 71: Comparison of corrosion of NiCrAlMo with a Na_2SO_4 deposit at 700°C in air to Type I hot corrosion [66] 138

ACKNOWLEDGEMENTS

I would like to thank my research advisors Professors Gerald H. Meier and Frederick S. Pettit for the guidance and wisdom given to me not only on the work for this thesis but in my all of my academic and research efforts. They create a work atmosphere that is both pleasant and exciting to work in. I also owe a lot of gratitude to my colleagues Michael Task, Michael Helminiak, Meltem Yanar, Ed Magee, Keeyoung Jung, and Nan Mu for their experience and knowledge given to me in working in the laboratory. Without them this would not have been possible. I would also like to thank my committee members, Professors Brian Gleeson and J.K. Lee for sharing their knowledge and expertise in the classroom and here on this committee.

This project was funded by the Office of Naval Research under contract number N00014-10-1-0661 and by the National Energy Technology Laboratory under URS Corps. Task Release 100.

1.0 INTRODUCTION

The growing population requires increasing amounts of electricity from sources that will have a reduced environmental impact. The worldwide energy demand will increase by approximately 40% by 2030, and coal combustion is believed to account for 30% of the future worldwide energy production.[1] Coal is plentiful and available at low cost, but traditional methods of coal combustion lead to high pollutant and CO_2 emissions. Global warming is becoming a bigger problem every day with the emission of greenhouse gasses, and therefore power plants in the United States are under increasing pressure to improve thermal efficiency in order to provide abundant and affordable electricity while reducing gas emissions. Advanced coal combustion designs will provide this. Older power plants from the 70's and 80's need to be either replaced with the new advanced combustion technology power plants, or with their retrofit. Some of the advanced combustion technologies include using renewable fuels, such as biomass, and carbon capture storage (CCS), such as oxy-fuel combustion. Part of the research performed for this thesis was for materials development for superheater and reheater tubes for oxy-fuel combustion systems.

Oxy-fuel firing is one of three ways in which CCS can be accomplished. The other two ways are post-combustion capture, where the CO_2 is removed from the flue gas after combustion, and pre-combustion capture, where the CO_2 is removed from the fuel before combustion. Oxy-fuel firing is carrying out the combustion in an environment consisting of recirculated flue gases

containing primarily CO_2, steam and pure oxygen instead of air in order to create a flue gas with minimal amounts of N_2, but still excess oxygen. A schematic of the oxy-fuel process is shown below in Figure 1.

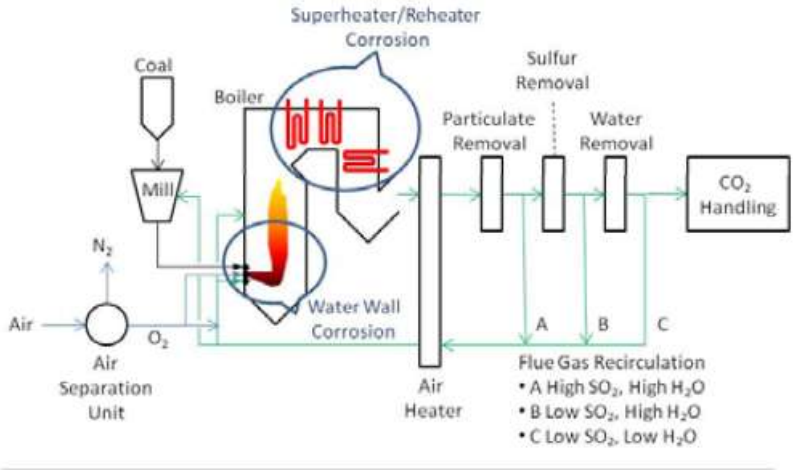

Figure 1: Schematic of oxy-fuel combustion

Oxy-fuel combustion produces flue gases containing 60%CO_2-30%H_2O-4%O_2-5%N_2, whereas traditional air-fired combustion produces flue gases containing 74%N_2-12%CO_2-9%H_2O-4%O_2.[2] The flue gases in oxy-fuel systems are able to be recycled through the fuel burners leading to decreased CO_2 emissions. However, with the reduced amounts of nitrogen, the products of the oxy-fuel combustion process have increased amounts of CO_2, steam and corrosive gases, such as SO_2 and HCl that will cause significant corrosion in superheater and reheater tubes when compared to air-fired combustion. Burning biomass as fuel or oxy-fuel combustion will increase corrosion due to increased corrosive gas products and ash deposits from the coal/biomass. SO_2 in the flue gas and ash deposits from the fuel cause severe corrosion in the superheater and reheater tubes of coal fired boilers where the temperature is the highest. This form of corrosion is called fireside corrosion, and is caused by the formation of liquid deposits on the surface of superheater and reheater tubes. Because the oxy-fuel combustion

system operates in two parts, the plant efficiency decreases. One way to overcome the efficiency loss of using oxy-fuel combustion is to increase the steam temperatures and pressures to ultra-supercritical conditions.

The efficiency of a coal-fired power plant is related to the steam temperature and pressure. This is the Carnot efficiency. A higher efficiency requires higher temperatures and materials that can withstand the higher temperatures than current coal-fired power plants. Ultra-supercritical steam conditions are the result of increasing temperature and pressure. The critical point for the water/steam system is 22.1MPa at 374^{o}C. Operating at higher temperatures and pressures produces supercritical and even higher produces ultra-supercritical steam conditions. At these high temperatures and pressures, water does not form a two-phase steam/water mixture during boiling. The system forms a single phase going from water directly into steam.[3] The goal is to move from supercritical conditions of 16.5-24MPa and 540^{o}C to ultra-supercritical conditions of 35MPa and 760^{o}C. The higher steam temperatures and pressures will significantly increase efficiency while decreasing fuel usage and CO_2 emissions. Compared to normal pulverized coal (PC) power plants which operate at 35% efficiency, ultra-supercritical steam conditions can potentially increase efficiency to more than 47%, while reducing carbon dioxide emissions by 30%.[4] The current materials used in supercritical conditions do not have the high temperature strength and corrosion resistance to be operated in ultra-supercritical conditions. The technology needed to reach the ultra-supercritical goals is developing stronger and corrosion resistant high temperature materials.

Advanced gas turbine engines are also being developed in order to decrease gas emissions and reduce fuel consumption. In other words, the efficiency of the engine must increase. This can be done by increasing the temperature and pressure of the combustion process

or developing improvements in component cooling technologies. Gas turbine engines, especially those used for marine propulsion or in coastal areas also undergo severe corrosion caused by Na_2SO_4 salt deposits on the surface of turbine hardware. When the conditions are such that the deposited salts become molten, as in fireside corrosion, severe degradation of the turbine hardware can occur. Increasing the temperature and pressure can cause the corrosion to be more severe.

The research presented here is focused on providing high temperature fireside corrosion information as well as indicating a corrosion mechanism to aid in materials development for oxy-fuel combustion systems. The identified corrosion mechanism for fireside corrosion will be compared to the mechanism of type II hot corrosion for turbine engines and the corrosion of rotor disk alloys, so that a better understanding of the corrosion processes for these varying types of attack can be obtained.

2.0 BACKGROUND

2.1 FORMATION OF DEPOSITS ON BOILER TUBES

Corrosion of the wall tubes of coal-fired boilers is caused by ash deposits that form a slag layer with high alkali and SO_3 contents and high solubility in water. The ash deposits on wall tubes prevent heat transfer, and lead to corrosion of the tube. Reid and Cohen[5] examined the influence of slag thickness on wall tubes. They showed that there is a stationary layer of slag next to the tube and a moving layer of slag at higher temperature. These layers are based on the temperature and composition of the slag. The more fluid a slag layer is, the more heat it will conduct to the tubes. The heat transfer through the slag increases linearly with slag surface temperature. The heat flux will vary around the tube, and it will be the smallest where the deposit is the thickest. Ely and Schueler[6] examined the influence of slag thickness on the heat transfer through the wall tubes. The heat flux was found to decrease as the slag becomes thicker with increasing time, this can be seen below in Figure 2.

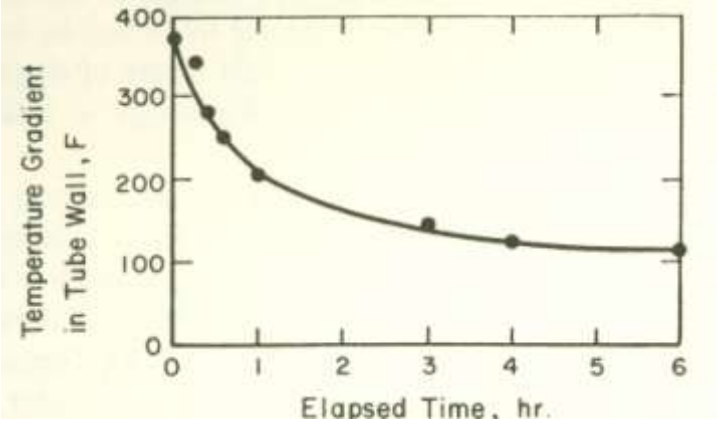

Figure 2: Rate of change of heat flux with accumulation of slag

The corrosion of superheater tubes from ash deposits is dependent on the operating steam temperatures. The steam temperature in boilers is increasing for increased efficiency in power production, but corrosion becomes a great problem at higher temperatures. The corrosion kinetics follow a bell-shaped curve with the largest amount of corrosion occurring in a temperature range of 650-750^{o}C. In this temperature range, the deposits become molten and corrode the metal. At lower temperatures, the deposits are solid and for the most part are not reactive. At higher temperatures, the deposits will become molten, however there is not enough SO_3 produced to cause the formation of highly corrosive alkali iron trisulfates. This will be explained in later sections. Trisulfates decompose in the absence of sufficient SO_3. At these high temperatures, a slag of alkali sulfates will form, which can still cause corrosion of the boiler hardware.

The build-up of ash deposit on boiler tubes was examined by Bishop[7]. He proposed the following possible causes of deposit build-up[3]:

- Alkali metal salts in the vapor phase condense on the tubes to form a sticky layer, which collects impacting particles of fly ash.

- The initial deposit consists of fly ash; the insulating effect of this ash results in the outer layers of the deposit becoming hotter than the inside, and this temperature gradient allows partial decomposition of sulfates in the hotter parts, with the SO_3 so formed diffusing toward the cooler surface. An inner dense alkali sulfate-rich layer forms.
- Alkali metal or alkaline-earth oxides are deposited on the surface, and are then converted to low-melting point sulfates and pyrosulfates by reaction with SO_3 in the bulk gas phase.
- Alkali chloride vapors from high-chlorine coals condense on the tubes and are converted to sulfates.
- Silicon compounds are evolved as vapors from silicate materials during combustion, and are then deposited as fine aerosol particles on the surface and are rapidly oxidized to silica.
- Molten ash particles in the hot gas stream impact on the cold metal surface and freeze in place.

Generally, a white deposit will form first on the surface of the tube. This is mostly sodium sulfate. An ash deposit then forms. The deposit on a corroding tube is shown below in Figure 3.[3] The amount of corrosion will be determined by the SO_3 partial pressure near the alkali sulfates and the temperature.

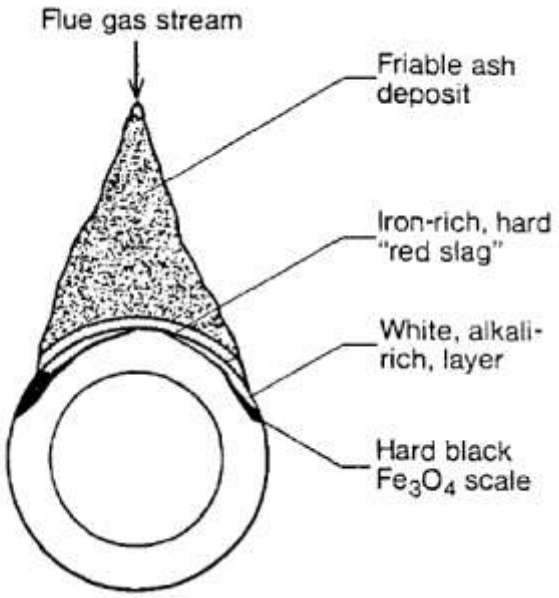

Figure 3: Deposits and corrosion area for typical reheater tube

2.2 FUEL

There are many different kinds of fuels that can be used in power generation systems. These fuels can be compared based on fuel storage, preparation and handling, combustions behavior, and fuel compositions that can cause corrosion issues. The types of fuels can range from solid fuels such as coal, biomass, and waste to gaseous fuels. Co-firing of different types of fuel is also possible.[8] The current research was focused on the deposits and corrosion caused from coal-fired boilers and power systems as well as gas turbine engines. Other types of fuels can lead to corrosion from different deposits and mechanisms.

2.2.1 Coal

When coal is burned, coal ash is put into the gas stream, and it becomes a major part of the deposits on superheater tubes. The typical composition of the flue gas in burning coal at temperatures between 400-1200^{o}C is shown below in Figure 4[9]. The big difference in flue gas composition between coal and other types of fuels is the SO_2/SO_3 content, which is increased due to higher amounts of sulfur in coal. SO_2 is dominant at temperatures greater than 700^{o}C, while SO_3 becomes dominant at lower temperatures.

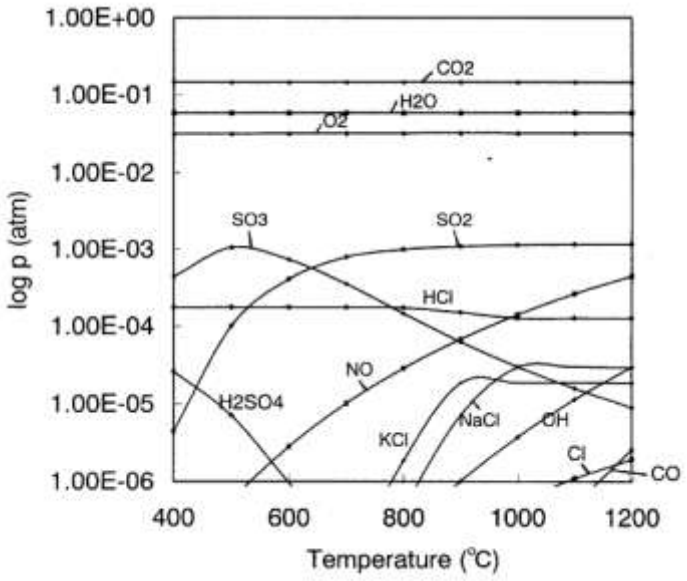

Figure 4: Calculated flue gas composition upon coal combustion

Differences in fuel composition can affect the formation of deposits on the superheater tubes. Table 1[9] below shows a typical elemental composition of coal compared with other kinds of fuels used in power generation systems.

Table 1: Elemental analysis of major fuel (wt%)

Element	MSW	Coal	Black liquor[a]	Oil[b]	Orimulsion[b]	LNG[b]
Ultimate						
C	22	76.2	28.4	85	60.1	76.5
H	8.7	5.13	5.2	12	10.1	23.5
O	60.4	6.15	44.3	0.4	26.4	–
N	0.3	1.63	–	0.2	0.35	–
S	0.02	1.73	2.7	2.35	2.85	–
Cl	0.4	0.275	3.0	–	–	–
ash	8.18	8.89	–	0.05	0.2	–
Metals						
Fe	0.2	1.1	–	–	–	–
Ca	0.9	0.1	–	–	–	–
Mg	0.1	0.04	–	–	370[c]	–
V	–	–	–	100[c]	310[c]	–
Na	600[c]	311[c]	13.0	50[c]	30[c]	–
K	400[c]	325[c]	3.4	50[c]	–	–
Zn	70[c]	–	–	–	–	–
Pb	10[c]	–	–	–	–	–
Heat value (kcal/kg)	2440	7509	3700	10 400	7242	13 000

The major difference between coal and other types of fuel is the sulfur content. The greater the amount of sulfur there is in the coal, the more corrosion that will occur. Coal can be generally described as high sulfur and high chlorine fuel. The iron content in the coal can also play a large part in the behavior of ashes. When in an oxidized form, iron oxide can raise the fusion temperature of the ash, but when it is in a less oxidized form, the fusion temperature will decrease. The ash viscosity will also increase with increasing ferrite content.[10]

It is the inorganic matter in fuels that is the cause of corrosion of boiler tubes. The products of combustion are relatively harmless. The amount of mineral matter in coal varies, but there is almost always enough to cause significant problems. The mineral matter occurs in coal as either cations and discrete mineral grains or as minerals that range in size between several microns to 100 microns.[11] Removal of the ash from fuels would solve the deposit-induced corrosion problem, but this is not economically feasible. The inorganic mineral matter in coal

can be categorized as inherent mineral matter or extraneous mineral matter. Inherent mineral matter is inorganic materials that were part of the original plant substances that turned into coal. Some examples of this type of mineral matter are iron, magnesium, calcium, phosphorous, potassium, and sulfur. Inherent mineral matter constitutes very little of the inorganic matter in the ash in coals. Extraneous mineral matter is inorganic materials that were added to the original substances during the process of becoming coal. This is the predominant contributor to the inorganic matter in the ash in coals. Extraneous mineral matter is roughly 4-7 microns in size.[12] Table 2[13] lists the common minerals found in coal in order of their abundance.[14] The main metallic elements are aluminum, iron, calcium, magnesium, titanium, sodium, and potassium. There are four main groups that all the minerals can be grouped into. These are clay minerals, sulfates and sulfides, carbonates, and quartz.[15]

Table 2: Occurance of minerals in coal

Mineral	Formula
Shale group	$(K, Na, H_3O_+, Ca)_{1-2}(Al, Mg, Fe, Ti)_4(Al, Si)_8O_{20}(OH, F)_4$
Clay group	$Al_2O_3 \cdot 2SiO_2 \cdot xH_2O$
(Kaolinite)	$Al_2O_3 \cdot 2SiO_2 \cdot 2H_2O$
Sulfur group	FeS_2, $FeSO_4$, Na_2SO_4
Carbonate group	$CaCO_3$, $CaCO_3 \cdot MgCO_3$
Associated minerals	
Quartz	SiO_2
Feldspar	$(K, Na)_2O \cdot Al_2O_3 \cdot 6SiO_2$
Garnet	$3CaO \cdot Al_2O_3 \cdot 3SiO_2$
Hornblende	$CaO \cdot 3FeO \cdot 4SiO_2$
Gypsum	$CaSO_4 \cdot 2H_2O$
Apatite	$9CaO \cdot 3P_2O_5 \cdot CaF_2$
Zircon	$ZrSiO_4$
Epidote	$4CaO \cdot 3Al_2O_3 \cdot 6SiO_2 \cdot H_2O$
Biotite	$K_2O \cdot MgO \cdot Al_2O_3 \cdot 3SiO_2 \cdot H_2O$
Augite	$CaO \cdot MgO \cdot 2SiO_2$
Prochlorite	$2FeO \cdot 2MgO \cdot Al_2O_3 \cdot 2SiO_2 \cdot 2H_2O$
Diaspore	$Al_2O_3 \cdot H_2O$
Lepidocrocite	$Fe_2O_3 \cdot H_2O$
Magnetite	Fe_3O_4
Kyanite	$Al_2O_3 \cdot SiO_2$
Staurolite	$2FeO \cdot 5Al_2O_3 \cdot 4SiO_2 \cdot H_2O$
Topaz	$(Al, F)_2SiO_4$
Tourmaline	$MgAl_3(BOH)_2Si_4O_{18}$
Hematite	Fe_2O_3
Penninite	$5MgO \cdot Al_2O_3 \cdot 3SiO_2 \cdot 2H_2O$

The deposits on superheater parts can be classified into three types: sintered and fused, alkali matrix, and phosphatic. Sintered and fused deposits are coal ash particles consisting of silicates, alumina, iron oxide, lime, magnesia, and alkalis that are carried by the flue gas and deposited on the surface of boiler tubes. Alkali matrix deposits contain large amounts of alkali sulfates. Phosphatic deposits rarely occur in coal-fired boilers. The average ash from coal contains 55-60%SiO_2, 20-30%Al_2O_3, 10-15%Fe_2O_3, about 1% TiO_2, P_2O_5, CaO, and MgO each, and SO_3 and the alkalis about 1%.[10] The most troublesome deposit is sintered deposits of fly ash. Fly ash can form thick layers on superheater and reheater materials and can reduce heat transfer to the tube, plug gas passages, and provide the environment in which complex sulfates form causing corrosion. The sintered deposits will form a layered structure, which is enhanced by the porosity of the sintered deposit and the temperature gradient.[10] The sintering characteristics of coal ash are very unpredictable, and are not well understood. The effect of the fly ash deposit particle size is very important. Smith[16] showed that the sintering temperature decreased as the particle size decreased.

The inorganic mineral matter in coals turns to ash or slag when heated. The mechanism of the process of transformation of mineral matter into ash in coal combustion chambers is shown below in Figure 5[12]. It is a very complicated process, because it is determined by the composition of the original mineral matter, its size and distribution within the coal, the heating rate, the mixing of the inorganic matter during combustion, the maximum temperature reached, time, and turbulence in the gas stream.

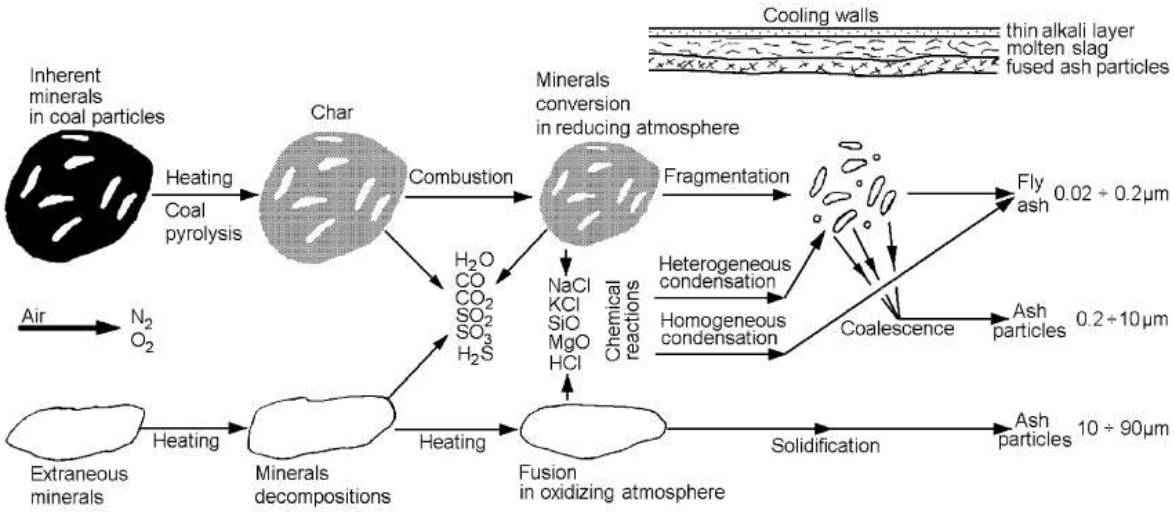

Figure 5: Mineral matter transformation mechanism

An example of some of the many reactions that occur is when sulfides, kyanites, and marcasite begin to decompose at 300°C. Under oxidizing conditions, the evolved sulfur is burnt to SO_2, while some may be emitted as H_2S in the flue gas. In an oxidizing atmosphere, magnesium and calcium oxides will react with SO_2 to form sulfates, which do not decompose until 1000°C.[10] The sulfur in coal is stabilized by the formation of these calcium and magnesium sulfates, while the remaining sulfur will be oxidized to SO_2/SO_3. Even though coal may have large amounts of chlorine, NaCl and KCl salts are not able to deposit on the surface. This is because there are high amounts of SO_2/SO_3 in the flue gas, so the chlorides react with SO_2, O_2, and H_2O to form sodium and potassium sulfates according to the following reactions[9],

$$2NaCl_{(s)} + SO_{2(g)} + ½\ O_{2(g)} + H_2O_{(g)} = Na_2SO_{4(s)} + 2HCl_{(g)} \qquad (1)$$

$$2KCl_{(s)} + SO_{2(g)} + ½\ O_{2(g)} + H_2O_{(g)} = K_2SO_{4(s)} + 2HCl_{(g)} \qquad (2)$$

Figure 6[9] below shows the condensed compounds in equilibrium with the flue gas that form when coal is heated. Na_2SO_4 and K_2SO_4 become thermodynamically stable at temperatures

below 900°C and 800°C respectively. Na_2SO_4 and K_2SO_4 are vapor condensed from the surrounding flue gas. The corrosion of boiler tubes is from liquid phase alkali iron trisulfates. These can only form from Na_2SO_4, K_2SO_4 and Fe_2O_3.[9]

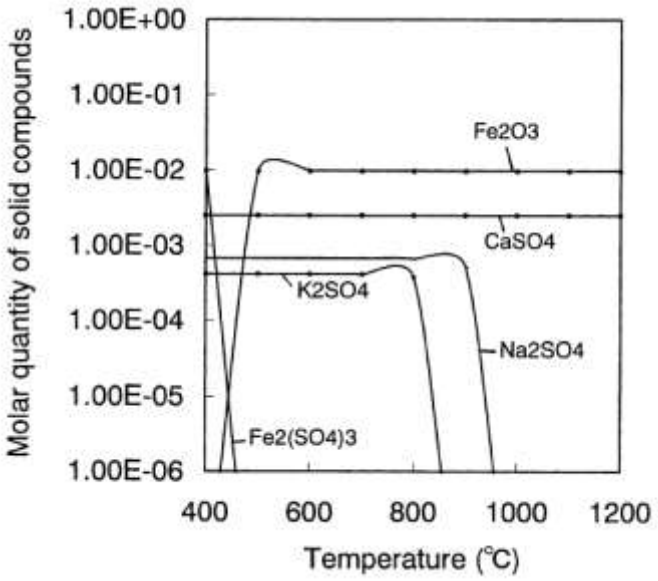

Figure 6: Calculated molar quantity of pure compounds of condensed phases in equilibrium with the flue gas upon combustion of 100g of the coal shown in table 1

2.2.2 Other Types of Fuels

Biomass consists of forestry and agricultural residues. The use of biomass in the power generation industry usually means wood, energy crops, or straw. Biomass is a renewable energy form, and it currently provides about 70% of the renewable energy sources worldwide.[2] Different types of biomass will have different compositions, properties, and costs when used as fuels. The timing of harvesting biomass can have an effect on its composition, but faster growing biomass will tend to have higher contents of chlorine and potassium as compared to

slower growing biomass. In general, biomass will have lower levels of sulfur when compared with coal. The corrosion causing deposit when burning biomass is alkali chloride salts, which can be even more damaging to the metal tubes. Burning biomass alone as a fuel has shown to have issues with fouling, deposition, and corrosion, but co-firing a small amount of biomass with coal will reduce SO_2 levels formed from combustion.[8]

Waste fuels are very inhomogeneous, and there are many different kinds of waste including sewage sludge, municipal solid waste, and refuse derived fuels. Waste generally has lower amounts of sulfur than coal but larger amounts of chlorine, therefore waste fuels can be considered high chlorine low sulfur fuels.[9] The corrosion causing deposits of waste fuels are also alkali chlorides. Co-firing of biomass or waste along with coal produces reduced amount of SO_2 in the combustion gas, along with higher steam temperatures which lead to higher efficiency and more electrical energy produced. Using 5% biomass in a 500 MWe coal power plant produces 25 MWe, while the same amount of biomass in a biomass only power plant produces 21MWe. Co-firing of biomass and coal also helps in reducing CO_2 emissions. It is also relatively easy to convert a coal-fired power plant into a co-fired plant with minor modifications. This is relatively inexpensive, and is much less expensive than building a new biomass only power plant. The allowable amount of biomass mixed with coal has not been determined, but some reports have shown that 20% biomass can be mixed with coal without having severe corrosion issues.[2] Oxy-fuel firing technologies use fossil fuels to produce a flue gas stream composed of CO_2 and H_2O. The flue gasses in this system need to be recycled. The flue gas stream does produce CO_2, steam, SO_x, and HCl levels that are significantly higher than coal systems, which can lead to increased corrosion. Deposits can also form on the heat exchanger systems.[8]

2.3 FIRESIDE CORROSION

Corrosion from combustion gases can occur in many ways in boilers and gas turbines. Fireside corrosion occurs by gas phase oxidation along with melted deposits that produce liquid-phase corrosion. Fireside corrosion can result in general mass loss or by the formation of cracks that then allow failure by mechanical mechanisms such as fatigue.[2] The temperature range of interest for boilers and gas turbines is between 650-750^{o}C. Corrosion can be decreased by using materials with good oxidation resistance at the temperature range of interest. Gas phase oxidation is not typically a problem as long as alloys are chosen that have adequate oxidation and spallation resistance. Liquid-phase corrosion results in rapid attack even on stainless steels. Alloys with high chromium contents above 22wt% show corrosion resistance. Chromium is the most beneficial alloying element for corrosion resistance. Fireside corrosion is an accelerated form of corrosion induced from the melting of impurities in coal such as potassium, sodium, sulfur, and chlorine. The temperature range of interest and the deposits will determine what type of corrosion will occur. The temperature regimes and corrosion materials are shown below in Figure 7.[17] At the temperature range of interest, alkali iron trisulfates are the main contributor to fireside corrosion. The formation of liquid alkali iron trisulfates on the surface of boiler tubes beneath an ash deposit will cause significant corrosion. Alkali sulfate and alkali chloride deposits will lead to rapid metal wastage especially when high sulfur coals are burned. The amount of corrosion will increase with increasing concentrations of SO_2 and alkali sulfates. The temperature that corresponds to the maximum metal loss follows a bell curve with a maximum between 650-750^{o}C. The curve can be shifted based on alloy composition, SO_2 level and alkali

content. Alloys with lower corrosion resistance will usually have larger metal loss at lower temperatures than those with high corrosion resistance. Pitting is the main result of fireside corrosion.[4,17-18]

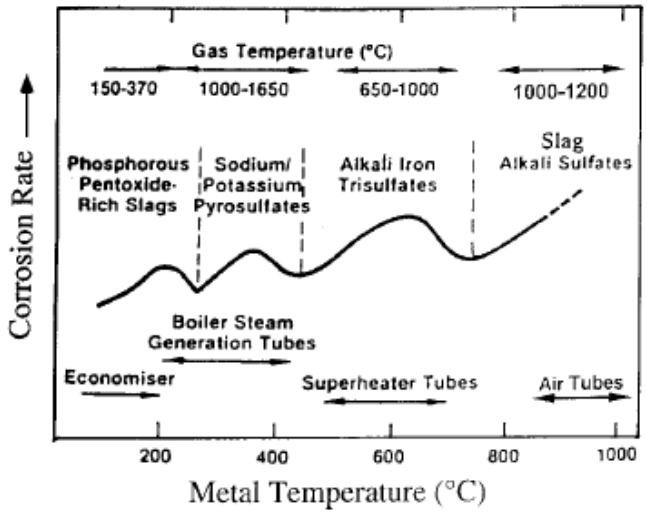

Figure 7. Fireside corrosion regimes in coal-fired boilers

2.3.1 Sulfur and Sulfates

There are four main elements in fuels that are the major causes of corrosion. These are sulfur, vanadium, and the alkalis sodium and potassium. Sulfur is the most serious of these four. Vanadium occurs only in fuel oils. Sodium and potassium are present in coal, while sulfur is present in coal and fuel oils. The compounds of sulfur with iron, oxygen, and the alkalis cause the most corrosion and accumulation of deposits. Sulfur can cause high temperature corrosion from complex sulfates, or it can cause low temperature corrosion by SO_3 reacting with deposits on the surface of metals (acidic fluxing).[19-20]

The amount of sulfur in coals can vary. The normal variation is 1-4%. Sulfur occurs in coal in three forms: pyrites (FeS_2), organic sulfur in the coal itself, and sulfates. Pyritic sulfur is found in all coals, most likely as bands in the coal bed. Pyrites make up about half of the sulfur found in coals, and an effective way of removing it from the coal has not been found without suffering significant coal losses or significant costs. Organic sulfur is part of the complex mixture of molecules that make up coal, along with carbon, hydrogen, oxygen and nitrogen. Organic sulfur is uniformly distributed within the coal. After pyrites, half of the remaining sulfur in coal is organic sulfur. Organic sulfur can only be removed by combustion. Sulfate occurs as iron sulfate, but the amount of sulfate sulfur is so low that it plays little role in the many problems that sulfur can cause. The sulfur content in fuel oils depends on where the original crude oil came from, and this varies from place to place all around the world. Most fuel oils in the United States contain less than 2% sulfur.[14]

Sulfur is highly reactive, especially with oxygen. SO_2 and SO_3 are in the products of combustion where they react to form sulfites, sulfates, and more complex trisulfates that cause corrosion. The total reaction for the formation of SO_2 is given by[10],

$$H_2S + 3/2O_2 = H_2O + SO_2 \qquad (3)$$

The reaction of sulfur and oxygen occurs in many steps, and many of the intermediate steps in the oxidation of sulfur are unstable and do not last very long, but they all may influence the amount of reactants formed and the rate of reaction. A list of the reactions involved with the oxidation of sulfur is given below in Table 3[21].

Table 3: Reactions in the oxidation of sulfur

$H_2S \rightarrow SH + H - 91$ kcal	(1)
$H + H_2S \rightleftarrows SH + H_2 + 19$ kcal	(2)
$SH + O_2 \rightleftarrows SO + OH + 16$ kcal	(3)
$OH + H_2S \rightleftarrows H_2O + SH + 22$ kcal	(4)
$SO + O_2 \rightleftarrows SO_2 + O + 18$ kcal	(5)
$O + H_2S \rightleftarrows OH + SH + 19$ kcal	(6)
$SO + O \rightarrow SO_2^* \rightarrow SO_2 + h\nu$	(7)
$SO + SO \rightleftarrows S_2O_2 + 49$ kcal	(8)
$SH + SH \rightleftarrows H_2 + S_2 + 26$ kcal	(9)
$4S_2 \rightleftarrows S_8$	(10)
$SH + OH \rightleftarrows H_2O + S + 27$ kcal	(11)
$S + O \rightleftarrows SO$	(12)
$S + S \rightleftarrows S_2$	(13)
$H + O_2 \rightleftarrows OH + O - 16$ kcal	(14)
$O + H_2 \rightleftarrows OH + H - 2$ kcal	(15)
$OH + H_2 \rightleftarrows H_2O + H + 15$ kcal	(16)
$SO_2 + O + M \rightleftarrows SO_3 + M + 82$ kcal	(17)
$SO + O_2 + M \rightleftarrows SO_3 + M + 93$ kcal	(18)
$SO_3 + H_2 \rightleftarrows SO_2 + H_2O + 38$ kcal	(19)

It does not matter what form of sulfur is present in the fuel, combustion will convert it into SO_2. The primary formation of SO_2 is by the oxidation of SO. The oxidation of pyrites can also form SO_2. Levy and Merryman [21] studied the formation of sulfur dioxide in combustion reactions in H_2S flames, and determined that the oxidation of SO is the major cause of SO_2 formation.

Sulfur trioxide in boiler furnaces and gas turbines can come from reactions within the flames, oxidation of SO_2, and dissociation of complex sulfates. As was mentioned earlier, the sulfate content in fuels is so small, that it cannot contribute significant amount of SO_3 to the flue gas. The main source of SO_3 in the flue gas is by the oxidation of SO_2. The amount of SO_2 will determine the amount of SO_3 that can form. In boiler furnaces, roughly 1% of the SO_2 is converted to SO_3. There are two reactions that can produce SO_3.[14]

$$SO_2 + ½\ O_2 = SO_3 \qquad (4)$$

$$SO_2 + O = SO_3 \qquad (5)$$

The oxidation of SO_2 with molecular oxygen only occurs in the presence of a catalyst. Dooley and Whittingham[22] found that the production of SO_3 occurs by the reaction of SO_2 with oxygen atoms, because there is a large concentration of atomic oxygen present in the combustion flames. Levy and Merryman [21] confirmed this by studying the microstructure of H_2S flames. The maximum amount of SO_3 created was found about one flame thickness downstream of the flame, and remained constant even at further distances from the flame. This can be seen in Figure 8[23] below. This proves that reaction 4 above is not responsible for the formation of SO_3, because large amounts of O_2 and SO_2 are present downstream of the flame, but the SO_3 level reaches a maximum and then remains constant. If reaction 4 were responsible, the SO_3 content would continue to rise.

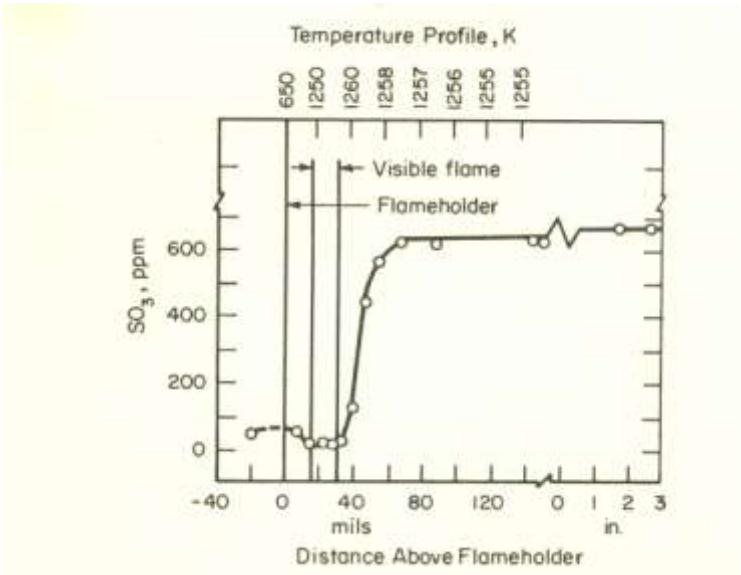

Figure 8: Formation of SO_3 in thin stabilized flame of H_2S-O_2-N_2

Levy and Merryman[21] also calculated the rate constants for the formation of SO_3 from two flames, and found that the same amount of SO_3 was created as in boiler furnaces. This shows

that the conditions in a boiler furnace or gas turbine will not affect flame-produced SO_3. The amount of SO_3 that can be formed from SO_2 depends on the temperature and the amount of the material exposed to the temperature. Lower temperatures will produce higher levels of SO_3. At temperatures 426^{o}C and below, SO_3 will dominate the gas, but at temperatures 1093^{o}C and above, SO_2 will be the major component in the gas.[10] The partial pressure of oxygen will affect the equilibrium values of SO_3. The more oxygen there is in the system, the higher amount of SO_3 that can be created, but even very small amounts of oxygen are capable of oxidizing SO_2 to SO_3 in equilibrium. It is unusual for equilibrium to actually be reached in actual boiler furnaces however. The reason is because the reactions do not have enough time to occur. The flue gas is cooled too quickly for equilibrium to be obtained.[14] When equilibrium levels of SO_3 are approached, there is usually a catalyst involved. There can be homogeneous and heterogeneous catalysts. In boiler furnaces and gas turbines, homogeneous catalysis is not a significant factor in the formation of SO_3. Platinum is a heterogeneous catalyst that can accelerate the oxidation of SO_2 by O_2. Vanadium and iron oxides, specifically Fe_2O_3, are also good catalysts and are less expensive. Harlow[24] was the first to find that Fe_2O_3 could be used as a catalyst for the oxidation of SO_2 by O_2. He found that the maximum amount of SO_3 formed was in a specific temperature range (bell shaped curve), and the amount formed was not only dependent on the temperature, but also the amount of surface exposed.

Deposits of K_2SO_4, Na_2SO_4, and Fe_2O_3 in a 1.5:1.5:1.0 molar ratio exposed at 1100F (593^{o}C) produced alkali iron trisulfates. This deposit mixture is known from Cain and Nelson[25] as the “standard corrosion mix”. Since 250ppm SO_3 is necessary to produce trisulfates at this temperature[26], catalysis must be responsible, because there was no SO_3 in the flue gas. Fe_2O_3 has been shown to be an excellent surface catalyst. Tests from Levy and

Merryman[27] have shown that any ferritic alloy with Fe_2O_3 on the surface will aide in the oxidation of SO_2, while Fe_3O_4 is an ineffective catalyst. A catalyst can be deactivated with additives from Group VA and Group VIA on the periodic table, specifically antimony or arsenic. Arsenic will deactivate platinum, so that it can no longer oxidize SO_2 to SO_3. Small amounts of Sb_2O_3 were shown to drastically decrease the formation of SO_3 in the standard corrosion mix.[14] The deactivating materials are highly toxic substances however, and having these materials in the flue gas would not be tolerated.

2.3.1.1 Pyrosulfates

Low-melting substances forming liquid films on the surfaces of boiler and gas turbine materials cause corrosion, and sulfates are the main cause of this. Alkali pyrosulfates such as K_2SO_7 and Na_2SO_7 were thought to be one of the main sulfates that cause corrosion. These substances have low melting points of 754^oF (401^oC) for Na_2SO_7 and 570^oF (299^o) for K_2SO_7 and high chemical activity. Studies by Reid showed that the level of SO_3 necessary to form the alkali pyrosulfates is not reached at the temperatures used in boilers and gas turbines.[14] Coats, Dear, and Penfold [28] examined the partial pressure of SO_3 with the temperature of alkali pyrosulfates. They found that the amount of SO_3 needed to produce pyrosulfates at the operating temperatures of boilers was higher than what is possible to be formed. At lower temperatures, the SO_3 content is high enough to produce pyrosulfates. This can be seen in Figure 9 below[28]. If the temperature is low and the SO_3 content is high enough, corrosion from pyrosulfates can occur.

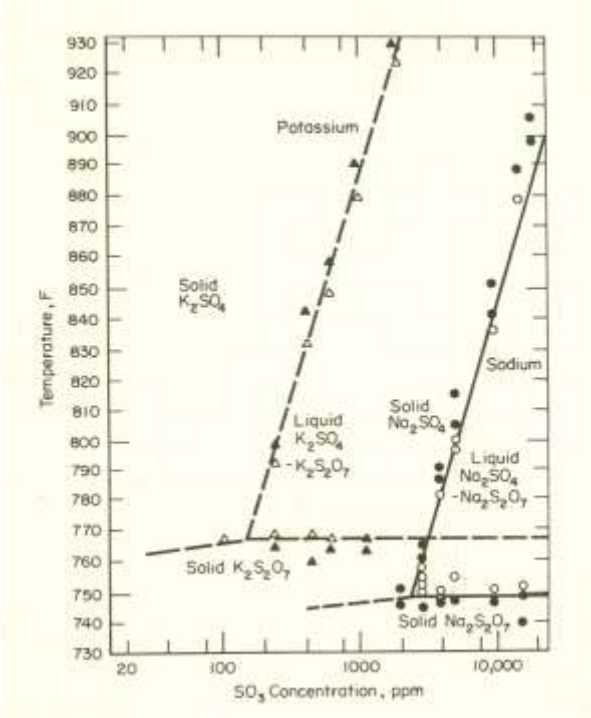

Figure 9: Melting points in the system Na_2SO_4-SO_3 and K_2SO_4-SO_3

The high concentrations of SO_3 needed come from the catalytic oxidation of SO_2 on the surfaces, which can create much higher SO_3 content than the bulk gas. The mechanism involves the formation of alkalis on the surface followed by a conversion to K_2SO_7 and Na_2SO_7 by the reaction of sulfates with SO_3 and their reaction of oxides grown on the surface. This is shown by the following reactions[10],

$$3Na_2SO_7 + Fe_2O_3 = 3Na_2SO_4 + Fe_2(SO_4)_3 \quad (6)$$

$$4Na_2SO_7 + Fe_3O_4 = 4Na_2SO_4 + Fe_2(SO_4)_3 \quad (7)$$

Further oxidation then occurs to replace the oxide scale leading to metal loss according to the reaction[10],

$$3Fe + 3O_2 = Fe_3O_4 \quad (10)$$

2.3.1.2 Alkali Iron Trisulfates

Most of the alloys used as boiler tubes are iron-based alloys, and the mobility of iron from the metal substrate to the oxide/gas interface is fairly rapid, therefore considerable research has been done on the formation of alkali iron trisulfates and their role in the corrosion of boiler tubes.[17] Alkali iron trisulfates are the most probable cause of liquid phase corrosion, because their melting points are in the range of superheater metal temperatures, they have been found in the areas where corrosion has occurred, and they are highly reactive materials. The melting points of some alkali iron trisulfates are shown below in Table 4[25].

Table 4: Melting point of complex sulfates

Compound	Melting Point, F
$K_3Fe(SO_4)_3$	1145 (618°C)
$K_3Al(SO_4)_3$	1210 (654°C)
$KFe(SO_4)_2$	1281[a] (694°C)
$Na_3Fe(SO_4)_3$	1155 (624°C)
$Na_3Al(SO_4)_3$	1195 (646°C)
$NaFe(SO_4)_2$	1274[a] (690°C)

[a] In high SO_3 atmosphere

Alkali iron trisulfates can form from reactions with iron oxides and SO_3 in the gas, leading to further iron oxidation and metal loss[10],

$$3K_2SO_4 + Fe_2O_3 + 3SO_3 = 2K_3Fe(SO_4)_3 \quad (9)$$

$$4Fe + 3O_2 = 2Fe_2O_3 \quad (10)$$

The iron oxides in these reactions can come from the oxide scale grown on the metal surface or from the ash deposits formed on the surface. $Na_3Fe(SO_4)_3$ forms from a similar reaction, and these reactions become the basis for determining the standard corrosion mix.[14] At 1100^oF

(593^{o}C), alkali iron trisulfates formed when the SO_3 level was above 250ppm. The amount of SO_3 present in the flue gas is a major factor on the formation of alkali iron trisulfates.[26] The trisulfates will decompose when heated in non-SO_3 atmospheres. The maximum amount of corrosion was found when deposits contain as much potassium as sodium in a molar ratio at high temperatures. The ratio changes with temperature, and this shows that the rate of corrosion is dependent on the melting point. Large amounts of clay minerals such as kaolinite ($Al_2O_3 \cdot 2SiO_2 \cdot 2H_2O$) will dilute the sodium and potassium in the deposit and result in less corrosion.[2] The reaction of SO_3 directly with the superheater metal surfaces is not a significant source for corrosion.[14]

2.3.2 Mechanism of Corrosion

Metal loss in boilers and gas turbines can occur by gas-phase oxidation, by removal of the protective scale on metals through chemical reaction with a deposit, or by direct attack of the metal surface. It is not certain which of these processes is the cause of fireside corrosion, but it is known that a liquid-phase deposit is needed for corrosion to occur at a significant rate. It may also be a case of many of these processes acting simultaneously. The formation of molten alkali iron trisulfates on superheater and reheater tube surfaces is the main cause of fireside corrosion. The corrosion of boiler metals is hard to replicate in a laboratory, because there are variations in the fuel and the environment is constantly changing. Some of the non-replicable environmental problems are that the actual composition of deposits formed on tubes is more complex than simulated deposits, the SO_3 content is variable, large temperature gradients occur, the ash and flue gas move at varying velocities, the composition of deposits will change with time, and fly-ash erosion can remove oxide scales exposing base metal.[29]

2.3.2.1 Gas-Phase Oxidation

Exposure of metal surfaces to the hot flue gas atmosphere creates an oxide film on the surface. The alloys used for boiler tubes are typically stainless steels that form a protective and adherent oxide scale on the surface. The oxidation of metals produces scales that can grow at linear, parabolic, logarithmic, or cubic rates. The rate is determined by the diffusion of components through the oxide layer and the reactions at the metal/oxide and oxide/gas interfaces. The parabolic rate law is the most common, and the one that describes the growth rate of oxide scales for alloys used in boilers and gas turbines. The parabolic rate law is given by the equation shown below[30],

$$x = 2(kt)^{1/2} \qquad (11)$$

where x is the oxide thickness, k is the rate constant, and t is time. Following this equation, the rate at which the oxide scale grows will decrease with time until it reaches a rate that is so small that it can be ignored. If the scale becomes too thick and breaks off, the metal will oxidize further at a high rate producing more metal loss. Most boiler metals are steels, and are therefore made out of iron. Unalloyed iron forms a multi-layered, fast-growing, non-protective scale that is dependent on the oxidation temperature. This can be seen from the iron-oxygen phase diagram shown below in Figure 10[30].

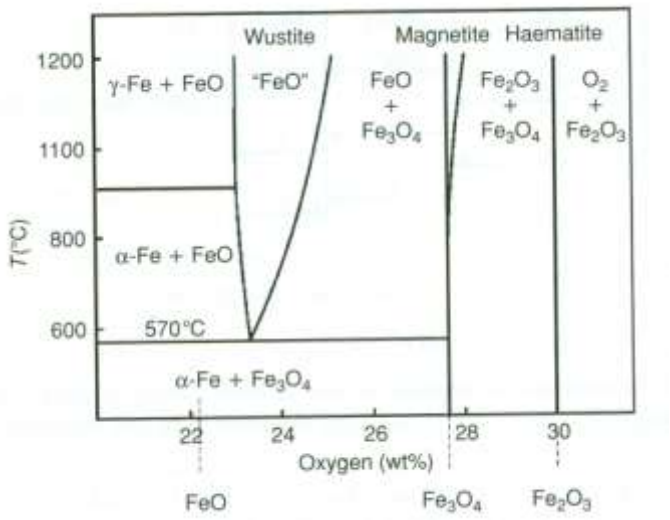

Figure 10: The iron-oxygen phase diagram

At temperatures above 570°C, iron will form an oxide scale consisting of FeO, Fe_3O_4, and Fe_2O_3 in order from the metal surface and in order of scale thickness. The relative thicknesses of the layers are given by the ratio, FeO:Fe_3O_4:Fe_2O_3 roughly 95:4:1.[30] FeO does not form below this temperature. Most metals used for boiler or gas turbine hardware are stainless steels or nickel based alloys. These alloys usually have significant amounts of chromium in them in order to slowly grow a protective layer of chromium oxide (Cr_2O_3) on the surface. This is known as selective oxidation. There is a critical amount of chromium needed in an alloy in order to form this external protective scale. If the critical amount of chromium is not met, then a non-protective internal oxide scale will form. The critical amount for the transition from internal to external oxidation can be determined from equation 12 given below[30], where N^{o}_{Cr} is the critical amount of chromium needed to form protective oxide layer, ν is the stoichiometric constant, g^{*} is a material constant, $N_O^{(s)}$ is the oxygen solubility in the metal, D_O is

the oxygen diffusion coefficient through the metal, V_m is the volume of the metal, D_{Cr} is the chromium diffusion coefficient through the metal, and V_{ox} is the volume of oxide.

$$N_{Cr}^{\ o} > \left[\left(\frac{\pi g^*}{2v}\right)\frac{N_O^{\ (s)} D_O V_m}{D_{Cr} V_{Ox}}\right]^{1/2} \quad (12)$$

The amount of chromium needed can be influenced by all of the parameters in the equation given above. Conditions that decrease the inward flux of oxygen, such as lowering the partial pressure of oxygen, or conditions that increase the outward flux of chromium, such as cold working the alloy, will decrease the amount of chromium needed in order to produce an external protective scale. There is also a critical amount of chromium needed in order to maintain the external protective oxide scale. This is given by the equation shown below[30], where k_p is the reaction rate constant.

$$N_{Cr}^{\ o} = \left(\frac{V_m}{32v}\right)\left(\frac{\pi k_p}{D_{Cr}}\right)^{1/2} \quad (13)$$

Most stainless steels used in high temperature applications are designed with chromium contents in excess of 20% in order to meet these requirements. Even with high chromium levels, iron ions will eventually diffuse through the chromia scale and a non-protective iron oxide layer will form. Austenitic stainless steels also contain large amounts of Ni, because Ni is an austenitic stabilizer, which are highly corrosion resistant materials. Nickel also enhances ductility and hardness. Pure nickel forms only one oxide scale, and that is NiO. This grows by the outward migration of cations and electrons, and it follows the parabolic rate law. The NiO scale is a slightly more protective scale and grows at a slower rate than pure iron, but it still requires selective oxidation at high temperatures for protection. Like the stainless steel alloys, the nickel based alloys used at high temperatures contain significant amounts of chromium in order to form the slowly growing external protective Cr_2O_3 scale. In any metal alloy that forms a

protective oxide layer on the surface, transient oxides of the base element can form before the protective oxide layer. This can increase the amount of alloying element such as chromium needed to form the protective external scale. The extent of the transient oxides is decreased by the factors that promote selective oxidation, such as higher chromium contents, reduced oxygen pressures, and cold working. Any rupture of the protective chromia scale will expose a lower chromium content alloy and return it to its transient state, causing more metal loss.[30] Typically gas-phase oxidation in boiler atmospheres does not lead to significant metal loss in boiler tubes and gas turbine hardware unless chlorides or low-melting oxides remove the usually protective oxide scales.

2.3.2.2 Liquid-Phase Corrosion

The presence of liquid is usually necessary in order for significant corrosion to occur. This is because chemical reactions are faster whenever liquids are present, liquids more effectively insulate the alloy from the gas, and because liquids provide an electrolyte for electrochemical attack. Different areas of the metal will act as cathodes and anodes. With a highly ionized melt, electrons will transfer from anode to cathode, so that anodic iron will oxidize.[14] The oxidation rate depends on the concentration of dissolved metal, the amount of oxygen and sulfur oxides in the melt, and the presence of other substances. A voltametric analysis of molten alkali sulfates showed that the degree of corrosion of iron will depend on the amount of SO_3 in the molten sulfate on the surface of the metal.[31] The rate of dissociation of the sulfate ions will determine the rate of corrosion. The SO_3 concentration in the molten sulfate is the equilibrium concentration at that temperature, and deposits of varying thickness will cause different SO_3 concentrations at the metal surface, setting up a corrosion potential gradient.

Figure 11[3] below, shows the temperature distribution through a superheater tube under typical operating conditions.

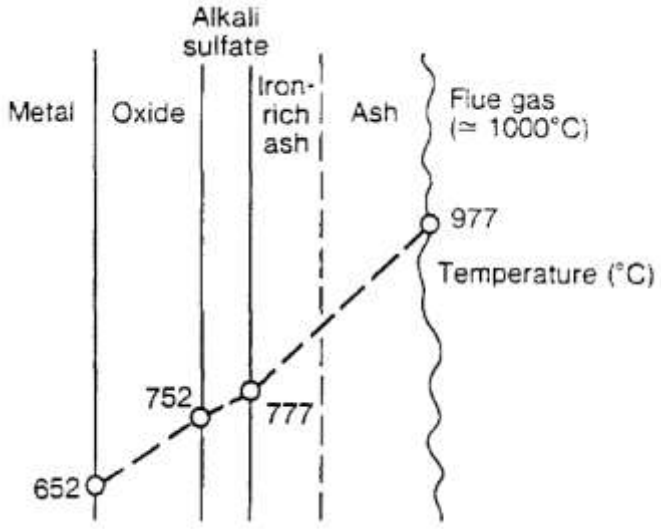

Figure 11: The general temperature distribution through a superheater tube, the oxide, and the deposit

The heat flux will be the least in the areas where the ash is the thickest, and there will be the least amount of metal loss where the deposit is the thickest, directly in front of the flue gas stream. Metal wastage is the largest at the edges of the deposit at the "five o'clock and seven o'clock positions", where the temperature gradient is the largest. As mentioned before, if the temperature is low and there are high amounts of SO_3, then pyrosulfates can cause corrosion. The temperature regimes in the present study were not in this range. The corrosion being analyzed was in the temperature range where alkali iron trisulfate is the main cause.

Alkali iron trisulfates such as $Na_3Fe(SO_4)_3$ and $K_3Fe(SO_4)_3$ are the main causes of corrosion in superheater and reheater tubes in boilers, and they have always been found in the areas where corrosion is occurring. It has been determined that metal wastage can occur due to the chemical reaction of iron oxide scales with alkali sulfates in the flame in the presence of

sufficient amounts of SO_3. The continuous reoxidation of the base iron alloy establishes the metal loss. The chemical reaction products between the iron oxide scale and the alkali sulfates are the alkali iron trisulfates $Na_3Fe(SO_4)_3$ and $K_3Fe(SO_4)_3$. The chemical reaction can be expressed by the following equations[14],

$$2Fe_3O_4 + 9K_2SO_4 + 9SO_3 + 1/2O_2 = 6K_3Fe(SO_4)_3 \quad (14)$$

$$Fe_2O_3 + 3K_2SO_4 + 3SO_3 = 2K_3Fe(SO_4)_3 \quad (15)$$

$$3Fe + 2O_2 = Fe_3O_4 \quad (16)$$

$$4Fe + 3O_2 = 2Fe_2O_3 \quad (17)$$

There are a series of steps in which the corrosion of the metal occurs according to this mechanism assuming a high enough SO_3 content. The steps can be seen in Figure 12 below and are as follows[14]:

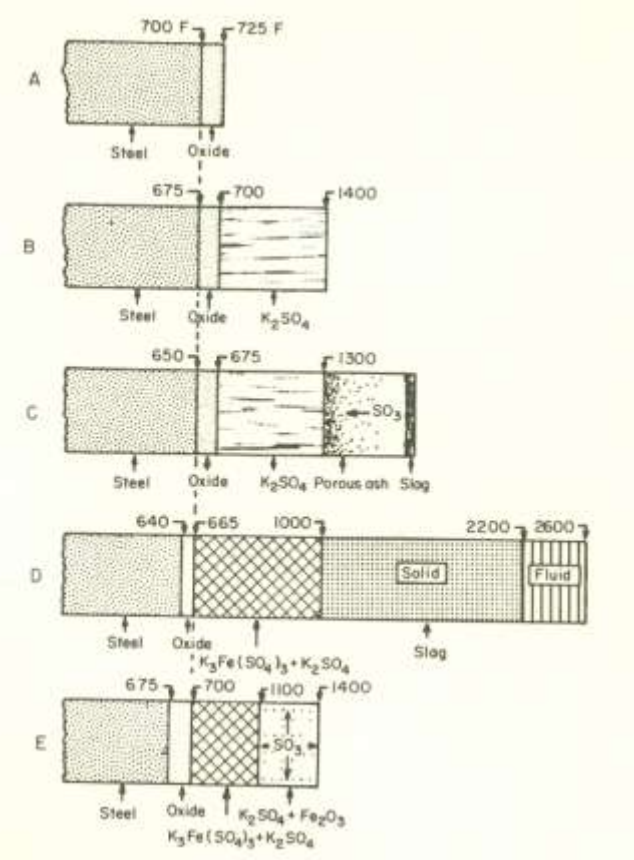

Figure 12: Mechanism of fireside corrosion of steel surfaces by removal of oxide film to form $K_3Fe(SO_4)_3$

A. An iron oxide scale grows on the surface of the metal tube.

B. Alkali sulfates such as K_2SO_4 that form from alkalis in the coal and the fuel ash and sulfur oxides in the atmosphere are deposited on the oxide scale.

C. The outer surface of the alkali sulfate layer becomes sticky due to an increasing temperature gradient, and this causes particles of fly ash to become captured on the surface. The temperature in the captured fly ash increases to the point that SO_3 is released by thermal dissociation of the sulfur compounds in the ash. The released SO_3 migrates towards the cooler base metal surface, and a layer of slag forms on the outer surface.

D. More ash is collected reaching a steady-state thickness. The temperature decreases in the alkali sulfate layer, which causes a reaction with the oxide scale and SO_3 occurs to form alkali iron trisulfates. This removes the oxide scale, which causes the base metal to reoxidize further causing metal wastage.

E. Deslagging then occurs exposing the alkali iron trisulfate layer to temperatures high enough to dissociate it releasing SO_3. Part of this released SO_3 moves toward the cooler part of the deposit, where it reacts with K_2SO_4 present and the oxide scale to form more alkali iron trisulfates. This leads to further oxidation of the scale and more metal loss.

This cycle can repeat indefinitely because there is no loss of alkalis except for the small amount lost due to deslagging. More alkalis can also be deposited from the flue gas after each deslagging event. The high SO_3 content needed for this reaction can come from the gas atmosphere and the catalytic oxidation of SO_2 with Fe_2O_3 as discussed earlier. The adherence of the ash deposits on the oxide scale is dependent on the characteristics of the oxide and the deposit. Because there is not a large difference in thermal expansion coefficients, the deposits on steel boiler tubes are very adherent and can become very difficult to remove. The deposits have been shown to peel off easily from austenitic stainless steels when cooled.[10] $K_3Cr(SO_4)_3$ has not been found in deposits, and so that shows that chromium oxide will resist corrosion from this mechanism, which explains why high chromium content alloys are more resistant to fireside corrosion. Calcium and magnesium in coal ash will inhibit the formation of alkali iron trisulfates, because they will preferentially form relatively harmless $K_2SO_4 \cdot 2CaSO_4$.

Cain and Nelson[32] came up with a corrosion mechanism in which the alkali iron trisulfates are formed within the ash deposit. They showed that the “standard corrosion mix”

mentioned previously subjected to the flue gas of 3.6%O_2 and 0.25%SO_2 produced molten alkali iron trisulfates. The trisulfates formed in fireside ash deposits by the reaction of Fe_2O_3 in the ash with alkali sulfates and SO_3, and they traveled through the ash deposit to the metal tube surface by means of a thermal gradient in the deposit. The molten trisulfates react with the base tube metal according to the reaction,

$$9Fe + 2K_3Fe(SO_4)_3 = 4Fe_2O_3 + 3FeS + 3K_2SO_4 \qquad (18)$$

A sulfide scale is formed in this reaction. Sulfides are not frequently found in the corrosion regions where trisulfides are present, so this corrosion mechanism must remove the results of sulfide penetration. This mechanism is shown below in Figure 13[32].

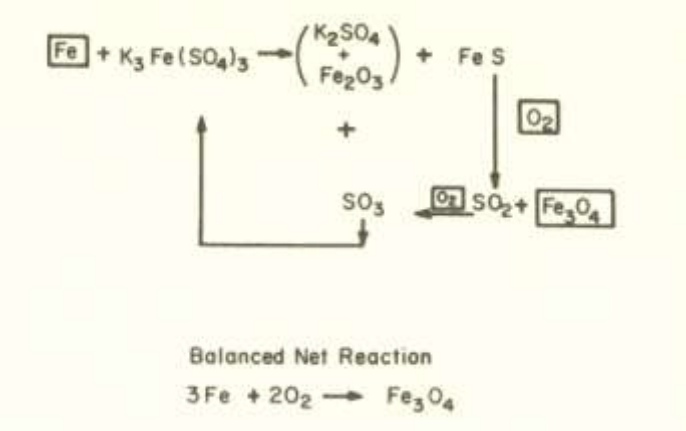

Figure 13: Coal-ash corrosion cycle

This mechanism proposes that only iron and oxygen are consumed and that Fe_3O_4 is the only product. Alkali sulfates and FeS are recycled by the FeS reoxidizing to SO_2 which then oxidizes further to SO_3, which then again reacts with Fe_3O_4 and alkali sulfates to produce more alkali iron trisulfates, which repeats the cycle. The only problem with this corrosion mechanism is that the metal loss occurs only by direct attack of the base tube metal by the alkali iron trisulfates. The

base tube metal will most likely form an iron oxide layer on the surface at the temperatures of interest, so that the exposed surface of the tube is iron oxides. Cracks in the oxide layer on the tube would expose base metal, and the proposed mechanism by Cain and Nelson could then occur, but the amount of metal loss this way would be small. Diffusion of the liquid through the oxide scale would also be limited. Erosion from ash particles flying at a high velocity can remove the protective oxide scale and accelerate corrosion from the mechanism by Cain and Nelson. The formation of alkali iron trisulfates as proposed by Corey and Reid is the most likely corrosion mechanism, although both may occur, the one proposed by Corey and Reid is the dominant one.[14]

Corey et.al.[33] showed that sulfides could also be present from unburned pyrites in the coal. The mechanism for large amounts of FeS in the regions of heavy corrosion is as follows[14],

A. Alkalis from the fuel are deposited on the oxide scale surface as alkali sulfates.
B. Unburned coal particles and pyrites become adherent to the tube surface and form a thick deposit layer.
C. The pyrites oxidize to FeS and Fe_3O_4, with evolved sulfur forming SO_2 and SO_3 in the deposit.
D. The sulfur oxides form small quantities of alkali iron trisulfates leading to a loss of some metal.

In places where combustion is complete and there is no unburned fuel or pyrites able to reach the surface of the metal tube, this mechanism is unlikely when compared to the trisulfates.

Shi et al.[34] studied the effects of different deposits on the rate of fireside corrosion of Fe-Al alloys. They found that for a Fe-10%Al alloy, the corrosion rate for a K_2SO_4 + Na_2SO_4

deposit was twice as high as for deposits of just K_2SO_4 or Na_2SO_4 alone. The corrosion rate was at a maximum at 650°C, and it increased with increasing SO_2 and SO_3 in the atmosphere and decreased with increasing aluminum content. This is similar to deposits of Na_2SO_4 alone. The corrosion kinetics curves for the deposits of K_2SO_4 + Na_2SO_4 and for Na_2SO_4 both show a linear segment, but the curve for K_2SO_4 + Na_2SO_4 became linear much earlier and was linear for a longer time. This can be seen in Figure 14[34] below.

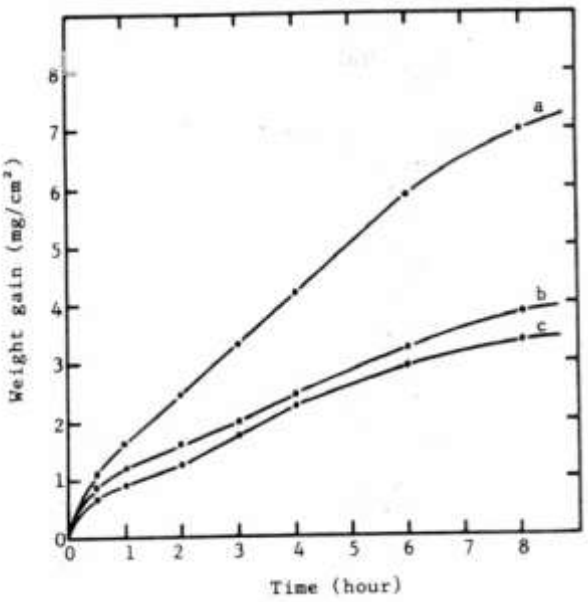

Figure 14: Oxidation kinetics of Fe-10Al Alloy exposed to O_2-0.5% (SO_2+SO_3) at 650°C: (a) Na_2SO_4-K_2SO_4, (b) Na_2SO_4 alone, and (c) K_2SO_4 alone

The addition of K_2SO_4 to the deposit does not change the corrosion mechanism, but it does significantly increase the corrosion rate. Sulfation tests also showed that the critical amount of SO_3 needed to cause the eutectic to melt is dependent on the temperature and decreases by more than an order of magnitude when K_2SO_4 is added to the deposit. This can be seen in Figure 15[34] below.

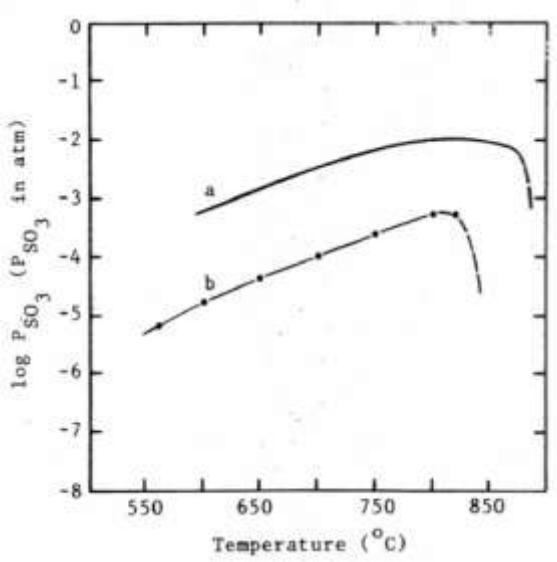

Figure 15: SO_3 levels required to stabilize eutectic melts: (a) Na_2SO_4-iron trisulfates and (b) K_2SO_4-iron trisulfates

The time at which the eutectic melts correlates to the start of the linear portion of the corrosion kinetics curve. The eutectic is melting earlier when K_2SO_4 is added to the deposit. The accelerated corrosion was found to occur not because of the formation of complex sulfates or the sulfation of Fe_2O_3, but because of the earlier formation of the eutectic melt.

Other fuels containing high amounts of vanadium or chlorine may also cause significant corrosion. Vanadium forms many low-melting compounds with sodium that become molten at the temperatures used in boiler superheaters and gas turbine blades. The corrosion caused by vanadium can come from a number of different mechanisms, but it is generally agreed that vanadium in the presence of oxygen and sulfur can cause significant metal wastage. Chlorine contributes to corrosion at high temperatures through either the formation of volatile chlorides or complex sulfates. Corrosion will occur when high amounts of chlorine are available, but it also occurs when there is no chlorine. It can be said that chlorine is a contributor to fireside corrosion, but it is not a major factor.[14]

2.3.3 Alloys for Use in Boilers and Gas Turbine Hardware

The main components in advanced combustion technologies that require high performance are high pressure steam piping and headers, superheater tubing, and waterwall tubing. With the advancement of new combustion technologies, higher thermal efficiency is needed, and so materials must be able to have high strength at increasing temperatures. Part of the research that was conducted for this thesis was for superheater tubing components for oxy-fuel combustion. These components must have high creep strength, thermal fatigue strength, weldability, resistance to fireside corrosion, and resistance to steam side oxidation and spallation. Martensitic or ferritic stainless steels would be beneficial from thermal fatigue strength and cost perspectives. However, the strongest of these materials can really only be used at temperatures as high as 620^{o}C, and even lower temperatures when fireside corrosion is being considered. Poor resistance to steam side oxidation and spallation can cause severe problems such as a loss of cross-section and an increase in temperature due to a decrease in heat transfer that can lead to premature creep failure.[35] Fireside corrosion of superheater tubes by liquid alkali iron trisulfates causes severe problems. High strength ferritic stainless steels such as T91 are frequently used in these applications. The standard metal alloys are T-22 for lower temperatures and SS304 or SS347 austenitic stainless steels for higher temperatures. At increased temperatures, stronger and more advanced austenitic stainless steels or nickel based alloys will be needed.[35] Alloys that have inferior corrosion resistance will have significant metal wastage at lower temperatures than those with greater corrosion resistance. For advanced ultra-super-critical combustors, only advanced austenitic stainless steels or nickel based superalloys will be able to be used, but the high price of nickel based alloys places most emphasis on advanced austenitic stainless steel development.

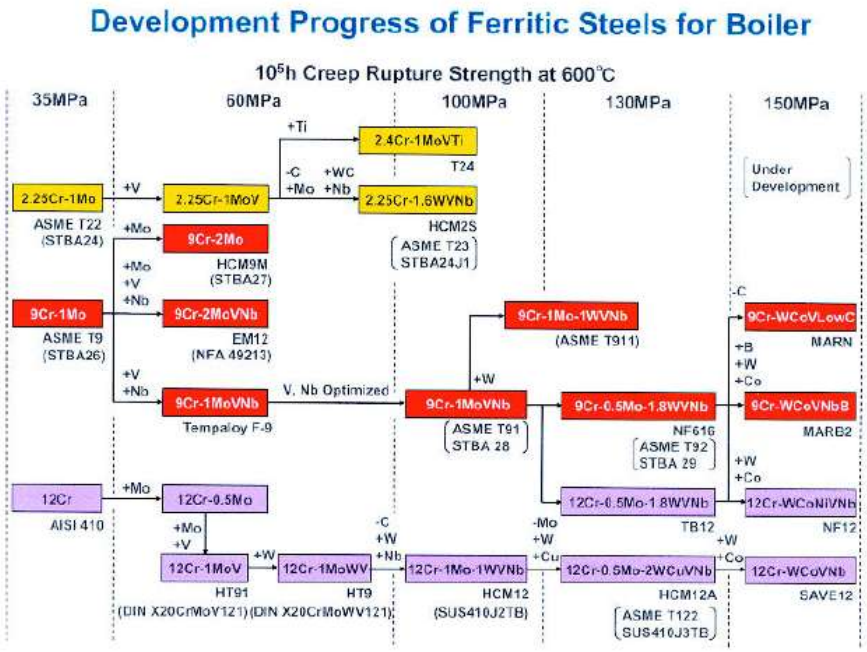

Figure 16: Evolution of ferritic steels for boilers

The evolution of ferritic stainless steel development is shown above in Figure 16[35]. The evolution includes additions of Mo, V, and Nb to simple 9-12%Cr alloys in the 1960's and 1970's, with optimization of these alloying additions coming in the 1970's and 1980's, followed by additions of Mo and W in the 1990's. Tungsten, molybdenum, and cobalt are solid solution strengtheners. Niobium and vanadium are precipitation strengtheners forming very fine coherent precipitates in the ferrite matrix. Chromium adds solid solution strength as well as oxidation and corrosion resistance. Nickel improves toughness, but decreases the creep strength of the alloy. Carbon is added to form fine precipitation strengthening carbides, but it must be kept relatively low for weldability considerations. Cobalt is also an austenitic stabilizer, promotes the nucleation of secondary carbides on tempering, and slows the coarsening of carbides. Ferritic stainless steels are mainly developed for use in thick section pipes and headers.[35]

Austenitic stainless steels are used for higher temperature applications because of their increased corrosion resistance due to increased chromium and nickel additions. Development of alloy additions to typical 18Cr-8Ni austenitic stainless steels and on very oxidation resistant 20-25Cr stainless steels is focused on improving the creep strength. Austenitic stainless steels are used in superheater tubing where fireside corrosion resistance and creep strength are important. They can be placed into four categories based on their chromium contents. These are 15%Cr, 18%Cr, 20-25%Cr, and >25%Cr. The standard alloy has 18Cr-8Ni, but increasing alloy development has led to the formation of 25Cr-20Ni stainless steels, which are much more corrosion resistant. The development of these alloys involves the additions of Ti, Nb, and Mo to stabilize the stainless steels. Ti, Nb, and Mo preferentially form carbides at the grain boundaries instead of chromium carbides that deplete the grain boundaries of chromium causing decreased corrosion resistance. Reducing the amount of Ti, Nb, and Mo, while adding C promotes creep strength while decreasing corrosion resistance. A balance between the two must be met. Cu additions will add precipitation strengthening, and small additions of N and W add solid solution strengthening.[35] Three advanced austenitic stainless steels that have been developed for ultra-super-critical conditions are TP347H, Super304H, and HR3C. These alloys have alloying additions Nb, Ti, Mo, Cu, N, and C for the reasons listed above. Chi et al. studied the microstructures and high temperature creep properties of these alloys.[36]

Figure 17[35] below shows a plot of the allowable stress versus temperature, comparing the high temperature capabilities of certain classes of alloys.

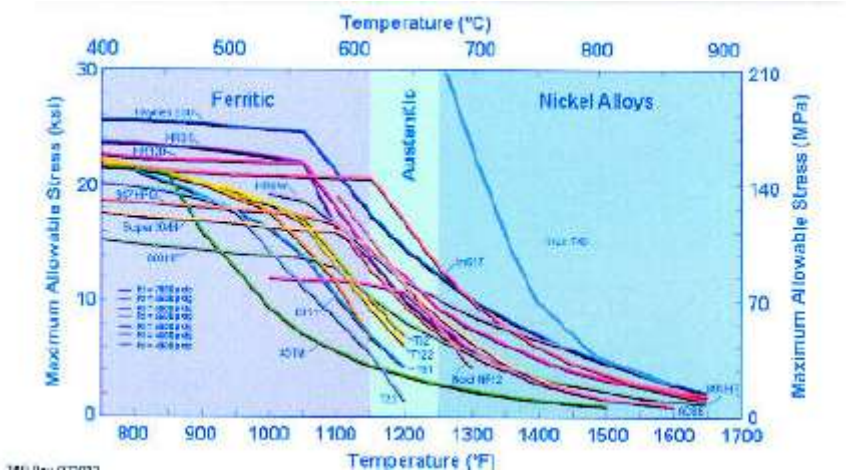

Figure 17: Allowable stress for various classes of alloys

The nickel based alloys are superior to the austenitic stainless steels, which are superior to the ferritic stainless steels. From a creep perspective, ferritic stainless steels are useful up to about 620^{o}C. Austenitic stainless steels are useful up to about 675^{o}C, and higher temperatures require nickel based alloys. Viswanathan et al.[35] studied various ferritic stainless steels, austenitic stainless steels, and nickel based alloys in steam oxidation and fireside corrosion tests. The steam side oxidation tests were conducted at 650^{o}C and 800^{o}C. The austenitic stainless steels and nickel based alloys fared better than the ferritic stainless steels and showed no spallation at 650^{o}C. An adherent protective chromium oxide scale formed over the alloys. The tests conducted at 800^{o}C showed that regardless of the type of alloy, if it had over 10%Cr, then the oxidation resistance was roughly the same. Some of the ferritic alloys fared as well as the austenitic and nickel based alloys. All of the metals showed worse corrosion resistance at 800^{o}C than at 650^{o}C. The fireside corrosion tests were performed with three different types of coals,

Eastern, Midwestern, and Western. Eastern and Midwestern coals typically have more sulfur, and are therefore more corrosive. The alloys tested with Eastern and Midwestern coals had more metal wastage than those tested with Western coals. The corrosion resistance increased with increasing chromium content. At 650^{o}C, the attack was more surface oriented, while at 800^{o}C the attack was more subsurface oriented. Molybdenum containing alloys suffered more corrosion than non-molybdenum containing alloys. Latham, Flatley, and Morris[37] studied the corrosion rates of some typical stainless steel alloys that could be used in coal-fired boilers. The variation in the corrosion resistance between the different alloys tested was not great, but they found that if a standard austenitic stainless steel is to be used, then additions of at least 25%Cr gives increased corrosion resistance, 1%Nb decreases intergranular penetration, and 1%Si is also beneficial. Stein-Brzozowska et al.[1] performed fireside corrosion tests on three austenitic alloys with varying chromium contents (18-25%) at 650^{o}C in typical air fired and oxy-fuel combustion atmospheres. The oxy-fired combustion tests produced more corrosion of the metal alloys than the air fired tests, probably due to the increased SO_2 partial pressures that result from oxy-firing. A uniform and protective chromium oxide scale is able to be formed with increasing chromium content in the alloy.

Natesan et al.[17] also performed fireside corrosion tests on some model and commercial stainless steels and nickel based alloys. The iron-based alloys had chromium contents in the range of 18-25%Cr, along with additions of Nb, Mo, V, N, Ti, and Ta to improve creep strength. The nickel based alloys had chromium contents in the range of 21-28%Cr, increased Mo contents, and additions of Al and Si. The tests were conducted with synthetic ash with varying amounts of Al_2O_3, SiO_2, Fe_2O_3, Na_2SO_4, NaCl, and K_2SO_4 at temperatures ranging from 650^{o}C-800^{o}C in an atmosphere containing 1%SO_2. The corrosion rates for the iron-based alloys tested

showed a bell-shaped curve with a maximum at 725^{o}C. The addition of NaCl to the deposit increased the corrosion rate for iron-based alloys. The NaCl will attack the precipitated carbides there to strengthen the alloy, and it will also form volatile chlorides that cause a non-protective porous scale. The corrosion of the nickel based alloys was more local and in the form of deep pits. The nickel based alloys did have lower corrosion rates than the iron-based alloys, especially with the deposit that included NaCl. This is because the vapor pressure of $NiCl_2$ is much lower than for the chlorides formed with the iron-based alloys. Cross-sectional images show that the attack looks to be from a low temperature hot corrosion mechanism caused by liquid eutectic alkali iron trisulfates.

Simms et al.[2] performed fireside corrosion tests comparing air and oxy-firing for a co-fired biomass boiler on typical ferritic and austenitic stainless steels as well as some nickel-based alloys. The synthetic deposits used on the alloys had varying amounts of Al_2O_3, SiO_2, Fe_2O_3, Na_2SO_4, and K_2SO_4, with the most corrosive being a stoichiometric mix of Na_2SO_4, K_2SO_4, and Fe_2O_3. The other oxides dilute the effects of the sulfates. In the absence of any deposit, the oxy-fired specimens had more corrosion than the air-fired. This is most likely due to the increase in CO_2, H_2O, and SO_2 in the oxy-fired atmosphere. The lower chromium content ferritic stainless steels such as T92 suffered the most corrosion. The alloys tested with higher chromium contents performed the best and had the smallest oxide scales grown on the surface. This includes nickel and iron-based alloys. The alloys had more corrosion in the oxy-fired tests than in the air-fired tests, most likely due to the increased amounts of steam, CO_2, and SO_2. Cross-sections of the stainless steels showed that there was internal molten deposit penetration of the scales, as sulfur and potassium were found to have penetrated deep into the scale.

Foster Wheeler Corporation[4,18,29] has also conducted fireside corrosion tests on high strength ferritic and advanced austenitic stainless steels as well as some nickel-based alloys. The evaluation of the alloys in fireside corrosion tests was done in three steps. Laboratory tests with different alloys, temperatures, deposits, and gas atmospheres were conducted to screen for the highest performing alloys. These alloys were then made into corrosion probes that were tested in the superheater and reheater sections of actual coal fired boilers. The third process was testing the best alloys under pressure in actual boiler operating conditions. They found that alloys with higher chromium contents, specifically those with greater that 25%Cr had adequate corrosion resistance. Alloys with high molybdenum contents had more corrosion than those without molybdenum. Tantalum, aluminum and silicon were beneficial. The tests performed in eastern coals, which contain higher amounts of sulfur, exhibited the typical attack from liquid alkali iron trisulfates, while the tests conducted in the western coals, exhibited atypical corrosion due to sulfidation from the presence of calcium sulfides in the coal. There was significantly more corrosion from the alloys tested in the Eastern and Midwestern coals, than from the western coals.

2.4 SODIUM SULFATE-INDUCED HOT CORROSION

Alloys used in the combustion process of gas turbine engines, especially those used in marine applications, can undergo an aggressive form of corrosion associated with the formation of a salt deposit, which is usually sodium sulfate, on the surface of the metal or thermally grown oxide. This type of corrosion is called hot corrosion. The Na_2SO_4 deposits on the gas turbine hardware can be directly deposited from ingested sea salt, or they can be condensed from a vapor

phase.[38] Vapor phase condensation occurs when the common fuel impurity, sulfur, is oxidized to form SO_2 and/or SO_3 in the combustion section of the engine. These gases then react with oxygen and NaCl vapor. If the surface of the turbine hardware is below the dew point of Na_2SO_4, then a condensed salt deposit will form. Bornstein and Allen[39] investigated the mechanism of salt deposition on the surface of turbine hardware, and determined that the direct impact of ingested sea salt particles on the turbine hardware is likely to be the main deposition mechanism. The amount of hot corrosion caused is determined by the composition and amount of Na_2SO_4 deposit, gas atmosphere, temperature, cycling, erosion, and alloy composition.[30] Once a deposit has been formed on the surface of combustion hardware, the amount of corrosion will depend significantly on whether or not the deposit melts. If the temperature of the combustion environment is above the melting point of Na_2SO_4 ($T_m = 884^oC$)[40], the corrosion is called type I hot corrosion or high temperature hot corrosion. Below the melting point of Na_2SO_4, the salt deposit can become molten because of a reaction between the combustion gas and the oxide scale grown on the alloy. This type of corrosion is called type II hot corrosion or low temperature corrosion. In the research presented, these two types of hot corrosion will be compared to the corrosion mechanisms of fireside corrosion as well as corrosion of disk alloys. They will be discussed in the sections to follow.

2.4.1 Stages of Corrosion

Hot corrosion occurs in two stages. There is an initiation stage, in which the rate of corrosion is slow and resembles that of oxidation without a deposit, and there is a propagation stage in which rapid and possibly catastrophic corrosion occurs.[30] The stages are demonstrated in Figure

18[30] below, which is a plot of weight change per area versus time for IN-738 exposed to Type I hot corrosion conditions with 1 mg/cm^2 sodium sulfate deposit.

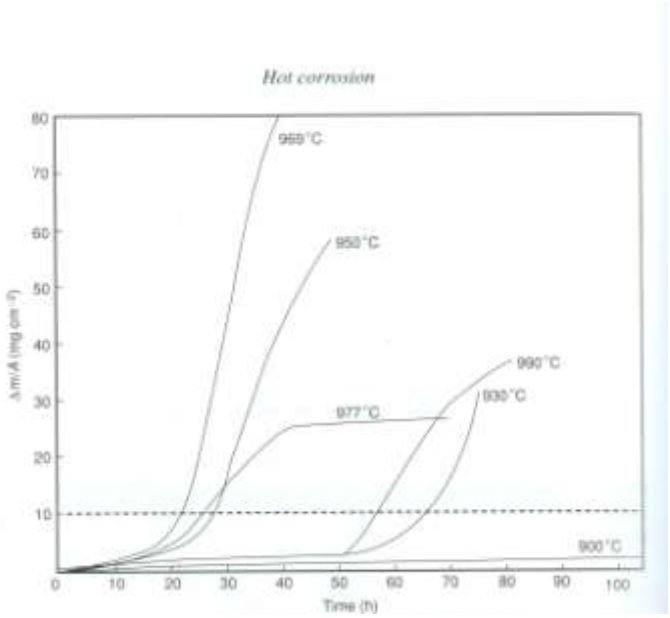

Figure 18: Isothermal mass change versus time for IN-738. The data consists of an initiation stage and a propagation stage with large weight changes (dashed line gives arbitrary end of initiation stage).

Examining the plot in Figure 18, the two distinct stages of corrosion can be seen. During the initiation stage, the weight change is very small, showing that there is little or no severe corrosion occurring. The propagation stage occurs when the weight gains start to become large due to rapid oxidation, and this signifies the occurrence of significant corrosion. The initiation stage of an alloy is very important. Corrosion resistant alloys are able to increase the initiation stage of corrosion, so that the alloy may be used for longer periods of time before failing. The length of the initiation stage can vary from seconds to hundreds of hours, and it is determined by the alloy and the combustion environment.

2.4.1.1 Initiation Stage

During the initiation stage of hot corrosion, the alloy undergoes a process similar to simple oxidation. The metal will oxidize and the gaseous species, typically oxygen will be reduced to form an external oxide scale. The difference between the initiation stage and simple oxidation is that during the initiation stage of hot corrosion, the reducing species comes from the salt deposit, and the alloy or oxide scale is being altered so that it is more susceptible to rapid degradation. The oxide scale/salt interaction can lead to extremely corrosive conditions as the salt becomes basic or acidic. At the end of the initiation stage, the salt deposit becomes sufficiently basic or acidic in order to cause rapid degradation, and the propagation stage begins. In many cases, the end of the initiation stage occurs when the deposit becomes liquid and penetrates the oxide scale and spreads along the alloy/scale interface. The presence of the liquid deposit in this region where the oxygen activity is low and the element producing the protective alloy is depleted produces severe corrosion and starts the propagation stage.[30]

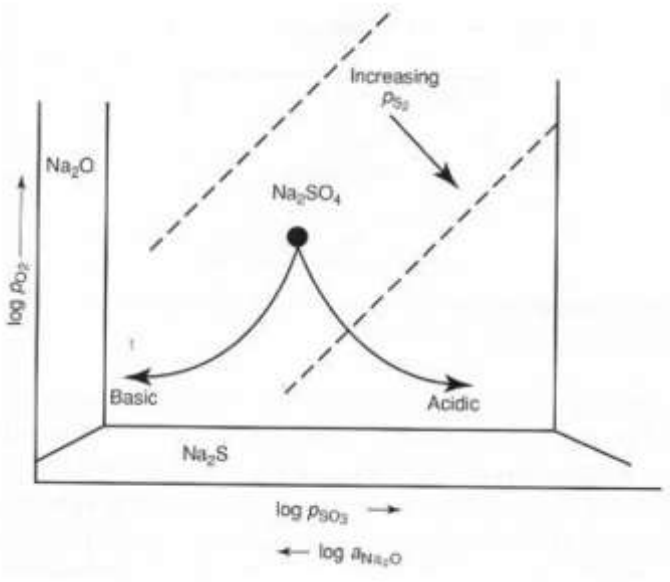

Figure 19: Thermodynamic stability diagram for the Na-O-S system at constant temperature

A phase stability diagram for the Na-S-O system is shown in Figure 19[30] above. The initially deposited salt is in the Na_2SO_4 phase field and is defined by the two axis logpo_2 and – loga_{Na2O}. The diagram shows the compositional changes that can happen to the initial salt deposit during the initiation stage of hot corrosion. The salt may become more basic (higher Na_2O) or more acidic (lower Na_2O) when interacting with the base alloy and its oxides. Giggins and Pettit[41] outlined some of the factors that affect the reactions that occur during the initiation stage as well as its duration. These are summarized below.

Alloy Composition: The initiation stage is longer for Co-based alloys than Ni-based alloys under Type I hot corrosion conditions. The reverse is true under Type II hot corrosion. Increased aluminum contents in Ni-Cr and Co-Cr alloys increases the initiation stage of hot corrosion. The addition of more aluminum produces a protective Al_2O_3 scale that is able to be retained for

longer times. Increasing the chromium content in alloys is also beneficial, and is the main element added for corrosion resistance. Larger chromium contents enable a protective Cr_2O_3 scale to be formed and be maintained for longer periods of time.

Alloy Fabrication: The hot corrosion of alloys can be influenced by the fabrication condition. As-cast alloys can be more susceptible to corrosion than a vapor deposited alloy, because of compositional inhomogeneity. The corrosion will initiate in areas that may be depleted in chromium or aluminum due to the inhomogeneous as-cast nature.

Gas Composition: The gas composition can have a significant influence on the initiation of hot corrosion. This is especially true for low temperature Type II hot corrosion, where corrosion occurs at temperatures below the melting point of Na_2SO_4. At these temperatures, the amount of SO_3 in the gas influences the duration of the initiation stage, and the amount of corrosion that will occur. In an atmosphere of just oxygen at 700^oC, the initiation stage can go on indefinitely, because the presence of SO_3 is required for Type II hot corrosion. This will be discussed in more detail in the later section entitled Type II hot corrosion.

Salt Characteristics: The composition of the salt deposit can have an effect on the hot corrosion of the alloy. For hot corrosion, salt deposits with NaCl mixed with Na_2SO_4 can have a different effect than pure Na_2SO_4 deposits. The composition of the deposits in fireside corrosion also has a significant effect on the amount of corrosion that occurs. This will be explained in later sections.

The amount of salt that is deposited will also affect the corrosion of the alloy. The amount of salt on the alloy is important, because some modes of corrosion are not self-sustaining, and the more salt that there is to consume and cause corrosion, the more corrosion will occur. Some alloys need the right composition of salt in order to induce attack. The amount

of salt may influence that amount of time for the deposit to react with the alloy to create the right composition needed to initiate attack. There may also be a limiting deposit thickness. For some propagation modes a thin deposit is more corrosive, while for others a thick deposit may be more corrosive. The amount of corrosion of Ni-based alloys under Type I and Type II hot corrosion conditions was found to be significantly less when the metal was submerged in salt compared to when there was a deposit of 1-8mg/cm^2.[42] This can be compared to fireside corrosion, in which there is the least amount of metal wastage where the deposit is thickest, as was explained earlier.

Temperature: It is generally accepted that a molten salt deposit is needed for hot corrosion. At higher temperatures above the melting point of Na_2SO_4, where Type I hot corrosion occurs, the deposit melts and significant corrosion occurs, however the initiation stage may be shorter at 900^{o}C than at 1000^{o}C. The attack can be less severe as the temperature increases because less salt can be deposited on the alloy as the temperature increases. For Type II hot corrosion, the salt deposit becomes liquid at lower temperatures, around 700^{o}C, in the presence of SO_3 gas. At higher temperatures, there are insufficient amounts of SO_3 in the gas to cause a liquid deposit. The deposit will remain solid, and less corrosion will occur. This will be explained in later sections.

2.4.1.2 Propagation Stage

Once the initiation stage has occurred and the alloy or oxide scale has been altered, the propagation stage occurs and the alloy becomes seriously degraded. There are three main types of propagation stages that can occur. These include alloy-induced acidic fluxing, basic fluxing, and gas phase-induced acidic fluxing. The first two listed here occur at high temperatures (above 900^{o}C) and are therefore categorized as Type I hot corrosion. The third kind of propagation

mechanism, gas phase-induced acidic fluxing, occurs at lower temperatures (650-750^{o}C) and is categorized as Type II hot corrosion. The type of propagation stage that occurs is dependent on what happens to the alloy and the oxide during the initiation stage, and it is therefore dependent on all of the variables listed in the previous initiation stage section. There are similarities and differences between the different propagation mechanisms, and therefore it might not be appropriate to label the corrosion of an alloy as one specific type of corrosion. There are some gray areas regarding which type of corrosion is occurring. The corrosion mechanisms for Type II hot corrosion, fireside corrosion and corrosion of some disk alloys will be compared in this thesis. It will be discussed later, but even though the tests were done at 700^{o}C, some of the corrosion mechanisms of the alloys tested were similar to Type I alloy-induced acidic fluxing.

The salt that is the cause of hot corrosion attack is typically Na_2SO_4. It is an oxyanion salt that exhibits an acid-base relationship with SO_3(g) being the acidic component and Na_2O(s) being the basic component. The composition of the Na_2SO_4 melt at a fixed temperature can therefore be described by the oxygen partial pressure and the activity of Na_2O in the melt, a_{Na2O}, or the SO_3 partial pressure, because it is related to the activity of Na_2O by equation 19 shown below.[43]

$$Na_2SO_4 = SO_3 + \underline{Na_2O} \qquad (19)$$

The product of $a_{Na2O} \cdot p_{SO3}$ is equal to an equilibrium constant K at a fixed temperature. This relationship is used to determine the acidity or basicity of Na_2SO_4, which was demonstrated in Figure 19. Thermodynamic stability diagrams are able to show the phases that can be stable during hot corrosion. These diagrams have axes of $\log p_{O_2}$ and $-\log a_{Na2O}$, and the

thermodynamically stable phase under the given conditions is shown. An example of this is shown in the diagram given below in Figure 20[44], which is the Cr-S-O system at T = 1200K superimposed on the Na-S-O stability diagram.

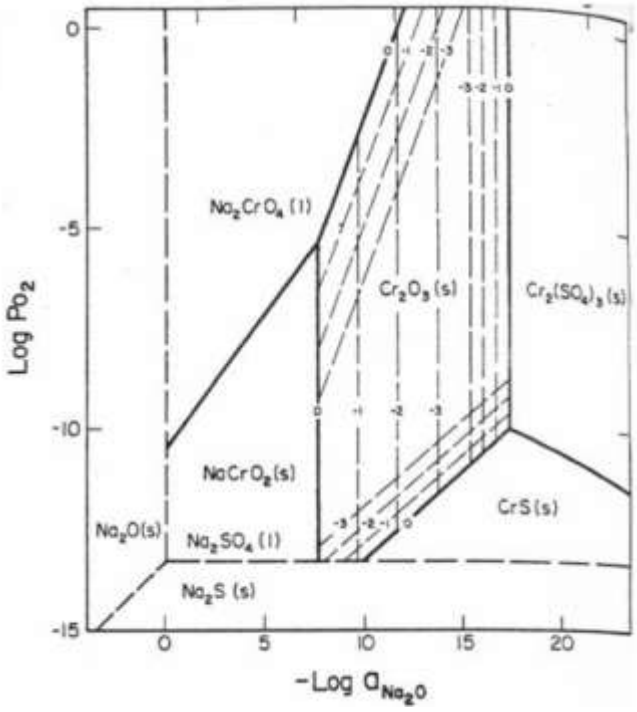

Figure 20: Isothermal stability diagram of the Cr-O-S System superimposed onto the Na_2SO_4 portion of the Na-S-O stability diagram for T=1200K

From the diagram in Figure 20, we are able to determine if a protective Cr_2O_3 scale will be able to grow or will dissolve in the presence of the salt deposit, and if it does dissolve, what solutes will be able to form. In this diagram, we are able to see that the Cr_2O_3 scale will dissolve into basic solutes of Na_2CrO_4 or $NaCrO_2$ or in acidic conditions, the acidic solutes of CrS and $Cr_2(SO_4)_3$. Thermodynamic stability diagrams for other oxide scales were completed by Rapp and coworkers as well as Deanhardt and Stern and can be seen in references [44-48]. They also produced solubility curves for a number of oxides in Na_2SO_4 as a function of the activity of

Na_2O in the melt. This was done by using high temperature reference electrodes at p_{O2} = 1atm and T = 1200K. Some of the typical solubility curves of a number of the oxides are shown below in Figure 21[44].

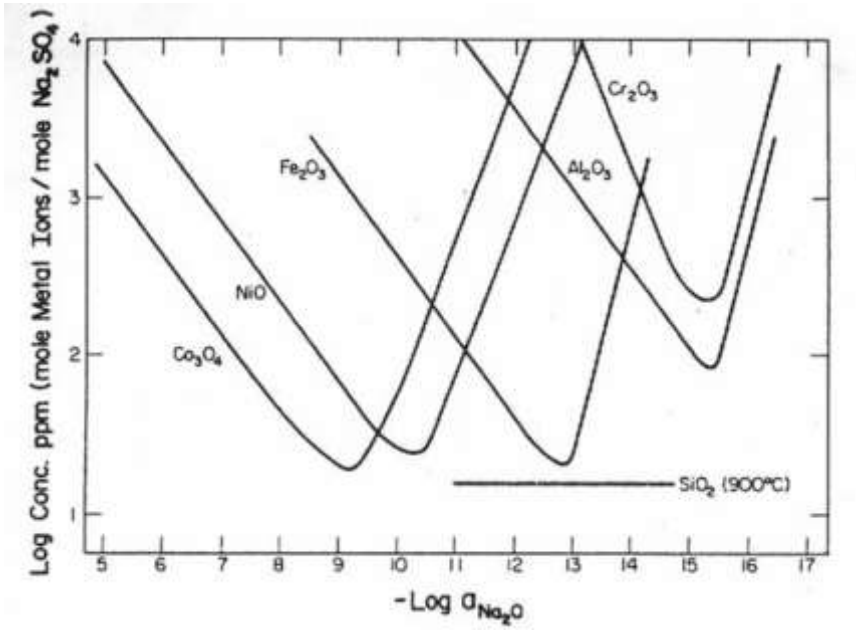

Figure 21: Measured oxide solubilities in Na_2SO_4 at 927°C and 1 atm O_2

The solubility minima of these oxides occurs over six orders of magnitude, which show that the salt chemistry is extremely important on the amount of hot corrosion.

As was mentioned earlier, the solubility plots shown in Figure 21 are for a constant p_{O2} = 1 atm, but some of the oxides will be dependent on the oxygen partial pressure. This can be seen from the basic dissolution reaction of Cr_2O_3 in Na_2SO_4 shown in equation 20 below.

$$Cr_2O_3 + 2Na_2O + 3/2\ O_2 = 2Na_2CrO_4 \qquad (20)$$

The Cr ion is oxidized from a Cr^{3+} ion to a Cr^{6+} ion during the dissolution, and so the solubility of Cr_2O_3 will increase as a function of p_{O2}. Alumina does not have this effect. This can be seen from the dissolution reaction shown in equation 21 below.

$$Al_2O_3 + Na_2O = 2NaAlO_2 \quad (21)$$

There is no change in valence of the Al^{3+} ion during the dissolution, and the solubility of Al_2O_3 in Na_2SO_4 is therefore independent of oxygen partial pressure. Rapp and Otsuka[49] explained this as the reason that higher chromium contents in alloys produces better hot corrosion resistance. The dependencies of oxide solubility on the oxygen partial pressure for chromia and iron oxides have been measured by Rapp and Zhang[50-51] and they were in good agreement with thermodynamic predictions.

The thermodynamic calculations based on the basic and acidic dissolution reactions are able to determine the shapes of the solubility curves. The oxide will dissolve by either accepting oxide ions (basic) or donating oxide ions (acidic). The slope of the curve is able to be determined by using the basic and acidic dissolution reaction equations, which are shown for NiO in equations 22 and 23 respectively below.

$$NiO + Na_2O + ½\ O_2 = 2NaNiO_2 \quad (22)$$

$$NiO + Na_2SO_4 = NiSO_4 + Na_2O \quad (23)$$

Assuming that NiO has unit activity, the equilibrium constant for the basic dissolution reaction can be given by equation 24 below.

$$K = \frac{a_{NaNiO_2}{}^2}{a_{Na_2O} p_{O_2}{}^{1/2}} \quad (24)$$

Taking the logarithm of both sides of the equation, solving for a_{Na2O}, and then differentiating with respect to $-\log(a_{Na2O})$ yields the slope of the left side of the solubility curve, which corresponds to basic dissolution. This is shown in equation 25 below.

$$\left[\frac{\delta log a_{NaNiO_2}}{\delta(-log a_{Na_2O})}\right] = -1/2 \quad (25)$$

The same can be done with the acidic dissolution reaction equation. This is shown in equations 26 and 27 below. This reveals a slope of 1 for the right side of the solubility curve, or the side pertaining to acidic dissolution.

$$K = a_{NiSO_4} \cdot a_{Na_2O} \quad (26)$$

$$\left[\frac{\delta log a_{NiSO_4}}{\delta(-log a_{Na_2O})}\right] = 1 \quad (27)$$

The minimum in the solubility curve is the point in which the acid and basic dissolution curves intersect. Rapp and Goto[52] have proposed a criterion for which the continued self-sustaining hot corrosion attack can occur. This is known as the Rapp-Goto Criterion, and it is given by equation 28 shown below, where C_{oxide} is the solubility of the protective oxide and x is the distance into the molten salt deposit from the oxide/salt interface.

$$\left[\frac{\delta C_{oxide}}{dx}\right]_{x=o} < 0 \quad (28)$$

When the solubility gradient is positive, the salt can become too saturated with oxide and a protective scale is able to form over the metal surface. A negative solubility gradient in the oxide solubility at the oxide/scale interface results in dissolution of the protective oxide scale and a reprecipitation of the oxide as discontinuous non-protective particles in regions of the molten salt deposit where the solubility is much lower.

Figure 22[52] shows a schematic of the conditions in the salt that satisfy the Rapp-Goto Criterion and produce hot corrosion of a material with a surface oxide.

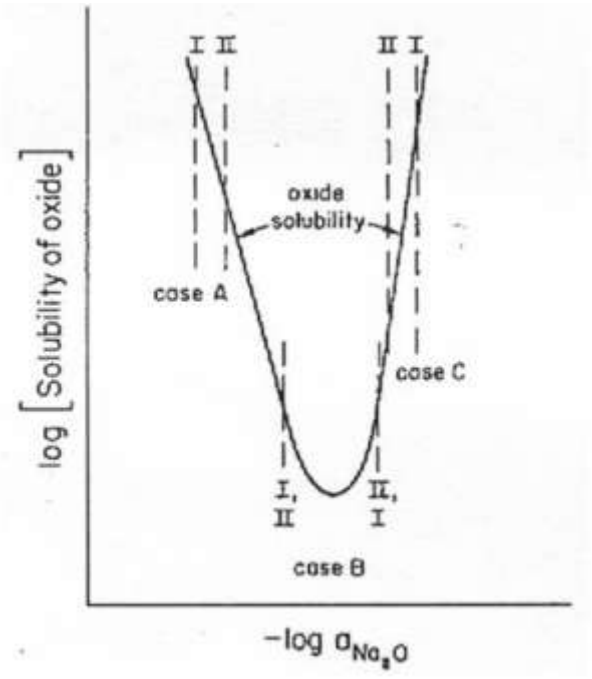

Figure 22: Conditions in the Na_2SO_4 salt the satisfy the Rapp-Goto Criterion

Figure 22 is plotted for a constant oxygen partial pressure. Three situations labeled A, B, and C are given in which solubility gradients are established so that hot corrosion can occur. The dashed lines labeled I are for the locations of the oxide/salt interface, and the dashed lines labeled II are for the locations of the salt/gas interface. Whether the dissolution is basic or acidic, the oxide solubility must be higher at interface I than at interface II, which are cases A and C. Continued oxide dissolution occurs for case B if the locations of the interfaces lie on either side of the solubility minimum. A general description of Na_2SO_4-induced hot corrosion

has been given. In the following sections the propagation or hot corrosion mechanisms for alloy-induced acidic fluxing, basic fluxing, and gas phase-induced acidic fluxing will be described in more detail.

2.4.2 Type I Hot Corrosion

As was mentioned earlier, Type I hot corrosion occurs at high temperatures of approximately 900-1000^{o}C. There are two propagation modes for this type of hot corrosion. These occur when there is dissolution of the protective oxide from a highly basic molten salt deposit where a_{Na2O} is high, and when there is dissolution of the protective oxide from a highly acidic molten salt deposit where p_{SO3} is high. These are called basic fluxing and alloy-induced acidic fluxing respectively. These two forms of Type I hot corrosion occur due to interactions between the salt deposit and the underlying surface. A description of the corrosion mechanisms for these two forms of Type I hot corrosion will now be discussed in more detail. Although the tests conducted were not at Type I hot corrosion temperatures, a description of basic fluxing and alloy-induced acidic fluxing will still be given. Some of the alloys tested did observe characteristics of alloy-induced acidic fluxing even at low Type II hot corrosion temperatures.

2.4.2.1 Basic Fluxing

When hot corrosion first became a problem for alloys used in the hot turbine section of gas turbine engines, it was concluded that the presence of molten Na_2SO_4 deposits was the cause. There were many different mechanisms proposed for this accelerated attack. The currently accepted mechanism for basic fluxing was first proposed by Bornstein and DeCrescente.[53] They investigated the oxidation of three superalloys: B-1900, U-700, and Waspaloy. The first

two are alumina formers, and Waspaloy is a chromia former. Their tests were conducted at 900°C with and without deposits of Na_2SO_4 and $NaNO_3$, so that the effect of the deposit could be determined. They also performed tests in which the alloys were impregnated with sulfur before being oxidized with and without $NaNO_3$ deposits, so that the effect of sulfur could be determined. Both deposits, Na_2SO_4 and $NaNO_3$, showed the same amount of degradation. The alumina forming alloys oxidized much more than the chromia forming Waspaloy. Sulfides were present when the Na_2SO_4 deposit was used, but not when the $NaNO_3$ deposit was used. The microstructures of all of the alloys in which salt deposit induced corrosion occurred had a porous non-protective oxide scale and a depletion zone beneath the scale. There was no accelerated oxidation with the sulfur impregnation tests with or without deposits. From these results, they determined that the oxidation of sulfides is not the cause of accelerated oxidation during Type I hot corrosion. They proposed that it is an interaction between Na_2O in the salt and the alloy substrate which causes the dissolution of the protective oxide scale and causes rapid oxidation. When Na_2SO_4 is used as the salt deposit, chromium rich sulfides form in the substrate, which removes sulfur from the salt and produces Na_2O ions in the melt. The accumulated Na_2O ions react with the substrate somehow, which results in rapid oxidation.

Goebel and Pettit[20] conducted tests on Ni providing further proof for this proposed mechanism. They confirmed that Bornstein and DeCrescenti's observation that a condensed Na_2SO_4 deposit is needed in order for corrosion to occur. A vapor phase salt deposit will not cause corrosion. The condensed Na_2SO_4 is the same as the vapor phase, which means that a compositional gradient is established across the salt layer on the surface of the Ni. This concentration gradient is unable to form when the salt is in a gaseous state because of rapid transport rates. Tests were performed on pure nickel specimens in air at 1000°C with and

without a Na_2SO_4 deposit. The salt deposit accelerates the oxidation of nickel during the early stages of oxidation, but it is not a self-sustaining attack because it returned to parabolic growth kinetics. The amount of attack does increase as the amount of Na_2SO_4 salt deposit increases. The uncoated Ni specimen showed a protective NiO scale, while the specimen with the salt deposit showed a very porous non-protective NiO scale with some nickel sulfides, which are liquid at 1000°C, at the oxide/metal interface. These tests led the authors to produce a mechanism for the corrosion process at 1000°C.

A thermodynamic approach was taken in order to come up with this mechanism. A phase stability diagram for the Na-Ni-S-O system was calculated and is shown below in Figure 22.[20]

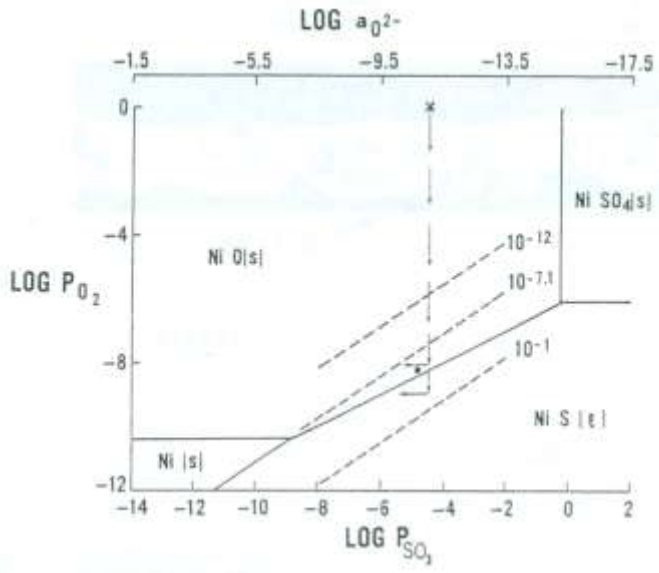

Figure 23: Phase stability diagram for the Na-Ni-S-O system at 1000°C

The diagram shows that when Na_2SO_4 comes in contact with Ni, NiO will form. The oxygen is supplied from the Na_2SO_4 deposit or from the dissociation of SO_4^{2-} ions. Oxygen will not be able to be transported through the salt from the gas atmosphere faster than it is being consumed

to form the NiO layer. This creates a positive oxygen activity gradient at the NiO/Na_2SO_4 interface across the molten salt deposit. Rapp[54] showed that the oxygen solubility in Na_2SO_4 is low, and that the soluble oxidant in hot corrosion is SO_3 in the molten salt. As the oxygen activity decreases along the gradient, the sulfur activity increases according to the equilibrium from the reaction shown in equation 29 below.

$$½\ S_2 + 3/2\ O_2 = SO_3 \qquad (29)$$

In the presence of two oxidants, namely O_2 and S_2, phase stability on the metal surface will be dependent on the ratio of p_{O2}/p_{S2} given by the reaction shown below in equation 30.

$$NiO + S_2 = NiS + ½\ O_2 \qquad (30)$$

At the surface of the NiO scale, NiS will be unstable, because very little oxygen will be removed from the molten salt at this location. If the sulfur activity is high enough and the sulfur can diffuse through the oxide scale to the metal/oxide interface, a region where the oxygen activity is even lower than in the Na_2SO_4 melt, then a NiS layer will form below the NiO oxide scale.[55] This is what was observed.

As more sulfur is removed from the melt to form NiS at the substrate surface, oxide ions are produced in the melt according to the following reaction.

$$SO_4^{2-} = O^{2-} + ½\ S_2 + 3/2\ O_2 \qquad (31)$$

The sulfur removal causes an increase of the oxide ion activity at the scale/salt interface, which is given by the following reaction.

$$Na_2SO_4 + 3Ni = 3NiO + Na_2O\ ½\ S_2 \qquad (32)$$

If the oxide ion activity of the Na_2SO_4 melt reaches high enough values, then a reaction can occur given in equation 33, where NiO reacts with oxide ions in the melt to form nickelate ions, NiO^{2-}, which are soluble in Na_2SO_4.

$$NiO + Na_2O = Na_2NiO_2 \quad (33)$$

There is a high oxide ion activity near the oxide/salt interface, and therefore as the nickelate ions form and diffuse into the salt, they encounter regions of lower oxide activity and they precipitate out as porous non-protective NiO oxide particles in the reverse reaction of equation 33. This is the cause of the porous NiO scale encountered in the researcher's experiments. As was mentioned before, the accelerated oxidation described is not self-sustaining and the reaction will eventually proceed to normal parabolic growth kinetics. This occurs because eventually the oxygen activity will reach a steady-state value, and the production of oxide ions reduces the sulfur activity in the melt, which causes NiS to no longer be able to be formed and the oxide ion concentration will be stabilized at a high value. When this occurs, a continuous protective NiO scale will form below the porous outer scale, and the accelerated oxidation will stop.[20] A schematic of the basic fluxing mechanism just described is shown below in Figure 24[20].

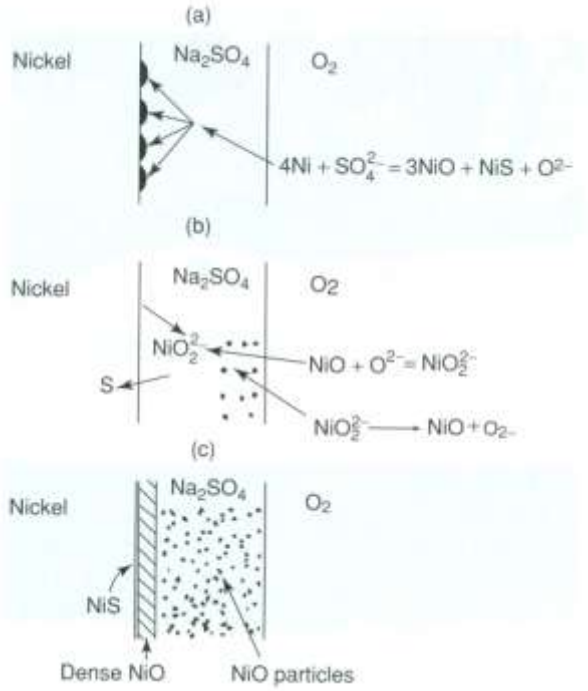

Figure 24: Model for Na_2SO_4-induced accelerated oxidation of nickel

This mechanism can be validated by the Rapp-Goto criterion. When accelerated oxidation is occurring, the oxide ion activity is much higher at the oxide/salt interface than it is further out into the molten salt. According to the Rapp-Goto criterion, this is the same as saying that the NiO solubility is greater at the oxide/salt interface than it is further out into the salt, which is a negative solubility gradient. According to equation 28, accelerated oxidation should occur until the oxide ion activity becomes stabile and NiS is no longer able to form, the NiO solubility gradient flattens out, and the Rapp-Goto criterion is no longer applicable and normal parabolic growth kinetics occur.

Goebel and Pettit performed further tests in Type I conditions with nickel-based alloys.[56] They tested pure Cr, Ni-Cr, Ni-Al, and some chromia and alumina forming alloys. The tests were conducted at 1000^{o}C in pure oxygen after presulfidizing in an H_2/H_2S

environment in order to determine the effect of sulfur on the oxidation behavior of the alloys. The presulfidation treatment did not affect the oxidation behavior of the pure Cr. A Cr_2O_3 scale grew over a layer of CrS. Presulfidation did increase the oxidation rate of the Ni-Cr alloys if NiS formed, because NiS is molten at the temperature tested. NiS is able to go through the protective Cr_2O_3 scale creating rapid diffusion paths for oxygen, leading to increased oxidation. The Ni-Al alloys oxidized significantly if the Al activity was sufficient enough to form Al_2S_3. If the Al activity is not sufficiently high enough to form Al_2S_3, then NiS formed and Al was selectively oxidized to form Al_2O_3. The chromia-forming alloys performed similarly to the Ni-Cr alloys, while the alumina-forming alloys performed like the Ni-Al alloys that do not form Al_2S_3. This shows that the basic fluxing mechanism described earlier is only valid for chromia forming alloys and Ni-Al alloys with high Al activities.

As was explained earlier, Bornstein and DeCrescente performed tests on some nickel-based superalloys and some Ni-Cr alloys.[57] There was a lack of corrosion of the Ni-Cr alloys, which showed that Cr is beneficial for hot corrosion resistance. This is due to the formation and dissolution of Cr_2O_3, which lowers the important oxide ion levels at the oxide/scale interface according to the reaction given in equation 34 below.

$$Cr_2O_3 + 2Na_2O + 3/2\ O_2 = 2Na_2CrO_4 \qquad (34)$$

Goebel and Pettit also studied the oxidation of some commercial and model nickel-based alloys containing various amounts of Cr, Al, Mo, W, and V in order to determine the effects of alloy composition on the basic fluxing corrosion mechanism.[19] It was concluded that a second form of Type I hot corrosion occurs with Mo, W, or V containing alloys that leads to catastrophic oxidation. This type of hot corrosion is alloy-induced acidic fluxing, and will be discussed in more detail in the following section.

The basic fluxing mechanism has been described in detail, and there are a few distinct features. Metal sulfides are usually found in the alloy substrate because sulfur is removed from the Na_2SO_4 melt. The amount of attack depends on the production of oxide ions in the melt. The oxide ion concentration eventually reaches a steady-state value, greater than the initial Na_2SO_4 deposit, and the melt becomes supersaturated with oxides that reprecipitated out during the basic fluxing process. Therefore, the attack is not self-sustaining. This type of attack only occurs at high temperatures (900-1000^oC) and in gas atmospheres that do not contain large amounts of acidic SO_3.[30]

2.4.2.2 Alloy-Induced Acidic Fluxing

The second propagation mechanism for Type I hot corrosion is alloy-induced acidic fluxing. It was shown that the basic fluxing mechanism in Type I hot corrosion is not self-sustaining. The oxide solubility plots given earlier show that a protective oxide scale can also be dissolved due to melts with low a_{Na2O} (acidic melts). The Na_2SO_4 deposit can become acidic due to SO_3 in the gas atmosphere, or by the dissolution of transient Mo, W, or V oxides that are added to superalloys for solid solution strengthening. Alloy-induced acidic fluxing is due to the latter and will be discussed here in more detail.

Bornstein et al.[58] studied the effects of various elemental additions to nickel-based alloys on the Na_2SO_4-induced hot corrosion at temperatures between 800-1000^oC. The oxidation rates of alumina forming alloys were significantly accelerated when there were additions of Mo or V in the alloys or when Na_2SO_4 was deposited with MoO_3 or V_2O_5. The first explanation for this phenomenon was that these acidic oxides react with oxide ions releasing SO_2 such as the reaction given below in equation 32.

$$V_2O_5 + Na_2SO_4 = 2NaVO_3 + SO_2 + ½\ O_2 \qquad (35)$$

The released SO_2 would then dissolve the protective Al_2O_3 scale with the reaction shown below in equation 36.

$$Al_2O_3 + 3SO_2 + 3/2\ O_2 = Al_2(SO_4)_3 \quad (36)$$

In order for this to occur however, significant amounts of SO_2 would have to be released in order for equation 36 to happen. The reaction in equation 35 would have to be extremely rapid, and this was not observed by the authors. They then concluded that the attack was due to the fact that the acidic transient MoO_3 and V_2O_5 oxides are molten at the temperatures tested. The molten oxides go through the Al_2O_3 scale, which causes rapid degradation of the substrate. Tungsten did not produce the same corrosion because its oxide is not molten at the temperatures of interest.

As was mentioned in the previous section, Goebel and Pettit[19] studied the oxidation of some commercial and model nickel-based alloys with different element additions in order to determine their effect on Na_2SO_4-induced hot corrosion. They oxidized Ni-Al Ni-Cr-Al alloys with additions of Mo, W, and V at 1000^{o}C in air with Na_2SO_4 deposits. All of the alloys tested were catastrophically degraded. The refractory element additions were found to be concentrated at the alloy/scale interface, and the attack was initiated with these phases. The authors also performed tests in which oxides of Mo, W, V, and Cr were mixed with Na_2SO_4 in an alumina crucible and heated to 1000^{o}C. The crucibles with WO_3, MoO_3, and V_2O_5 all lost weight and traces of Al were found in the salt after the test. This did not occur with the Cr_2O_3. The refractory oxides lower the oxide ion activity significantly so that the reaction in equation 36 can occur. Cr_2O_3 reacts with the oxide ions to a much lesser extent. Based on these tests the authors came up with a corrosion mechanism for refractory element-containing alumina forming nickel-based alloys.

During the first stages of oxidation, transient MoO_3 and NiO oxides as well as Al_2O_3 form at the alloy surface. MoO_3 reacts with the oxide ions in the Na_2SO_4 salt deposit to decrease the oxide ion activity of the melt, which prevents the basic fluxing mechanism from occurring. This reaction is shown below in equation 37.

$$MoO_3 + O^{2-} = MoO_4^{2-} \quad (37)$$

MoO_3 will decrease the oxide ion activity of Na_2SO_4 to levels where equation 36 and acidic fluxing of the protective Al_2O_3 scale can occur. The attack initiates near Mo-rich particles because the activity of MoO_3 in the Na_2SO_4 is highest in these areas. The fluxing of the Al_2O_3 scale causes Al^{3+} and MoO_4^{2-} ions to diffuse through the salt where Al_2O_3 is reprecipitated out as a porous non-protective scale, and the MoO_3 evaporates. This form of attack is self-sustaining unlike the basic fluxing mechanism, because MoO_3 is able to continue to form at the alloy/salt interface and evaporate at the salt/gas interface. Figure 25[30] below shows the weight change versus time plot for hot corrosion in air of Ni-8%Cr-6%Al and Ni-8%Cr-6%Al-6%Mo.

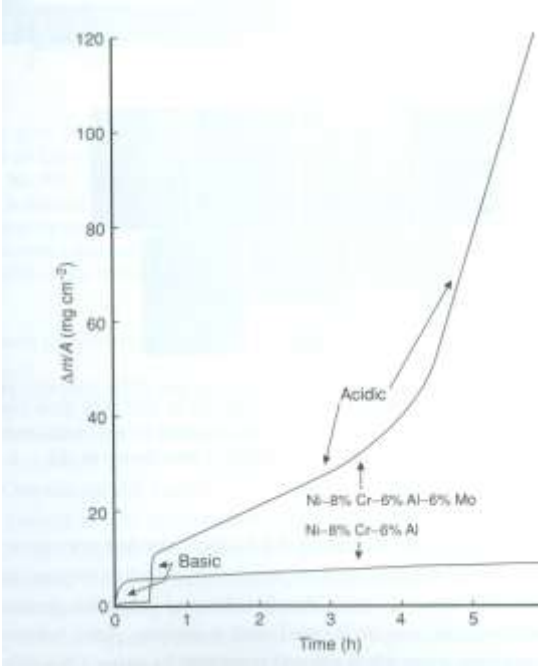

Figure 25: Comparison of isothermal hot corrosion of Na_2SO_4-coated Ni-CrAl and Ni-Cr-Al-Mo

The Ni-Cr-Al alloy undergoes basic fluxing that is not self-sustaining, while the Mo-containing alloy undergoes basic fluxing that turns into self-sustaining acidic fluxing. A negative solubility gradient is maintained in the salt at the salt/alloy interface, which maintains the Rapp-Goto criterion.

The alloy-induced acidic fluxing mechanism described above was for Type I conditions at high temperatures of 900-1000^{o}C. This mechanism will be compared to the mechanisms of the research performed for this thesis at 700^{o}C. The Mo containing disk alloys tested with Na_2SO_4 deposits at these low temperatures show characteristics of alloy-induced acidic fluxing, meaning there may be some gray areas for the characteristics of the different types of hot corrosion. This will be explained in more detail in the results and discussion sections.

2.4.3 Type II Hot Corrosion

Previous sections have described the hot corrosion mechanisms at high temperatures of around (900-1000^{o}C). It is also possible to have hot corrosion at lower temperatures between 650-750^{o}C, and the attack can be greater at these lower temperatures. Na_2SO_4 has a melting point of 884^{o}C, so it does not form a molten salt and remains solid at these temperatures. In order for severe degradation to occur, the salt must become liquid, and so severe corrosion would not be expected at these temperatures, but severe corrosion occurs in turbine blades and the hot sections of boiler hardware at these low temperatures all the time. This type of low temperature corrosion is called Type II hot corrosion. Type II hot corrosion is not well understood, but the accelerated corrosion is generally believed to be caused by the formation of a Na_2SO_4-MSO_4 eutectic melt that has a melting point well below that of Na_2SO_4.[56] It is also known that a partial pressure of SO_3 of about 10^{-5} is required for this melt to form.[60] This amount of SO_3 in the gas atmosphere is not uncommon in industrial gas turbines or superheater tubing for boilers. CoCrAlY coatings are more susceptible than NiCrAlY coatings and Ni-based alloys to this form of corrosion, and so the bulk amount of research has been conducted with Co-based metals.

2.4.3.1 Gas-Phase Induced Acidic Fluxing

The corrosion mechanism for low temperature Type II hot corrosion is also an acidic fluxing mechanism, but this time the Na_2SO_4 salt deposit becomes acidic due to SO_3 in the gas atmosphere. This is why it is called gas-phase induced acidic fluxing. There has been a great deal of research on the mechanism of Type II hot corrosion of Co-based materials.[59-62] This type of attack on CoCrAlY coatings is generally described as very localized pitting attack, with the pits containing porous unprotective Cr_2O_3, Al_2O_3, $CoCr_2O_4$, or $CoAl_2O_4$ with AlS forming a

layer at the base of the pit. Cobalt oxides or cobalt sulfates will form at the corrosion product/gas interface depending on the partial pressure of SO_3 in the gas. Higher SO_3 contents will form cobalt sulfates.[40] Binary Co-Cr alloys have similar morphologies as the CoCrAlY coatings, but there are only Cr- and Co- rich corrosion products. There is no Al in the alloy. Also, CrS form a layer at the base of the pit instead of AlS. Binary Co-Al alloys sustained a more frontal attack, but the distributions of the elements in the corrosion products were similar to the Co-Cr and CoCrAlY alloys. There were of course only Al- and Co- rich corrosion products as well.[40]

A liquid deposit is generally required for severe corrosion to occur. For Type I hot corrosion, this is not a problem, because the operating temperatures are above the melting point of Na_2SO_4 ($T_m = 884^oC$). For low temperature Type II hot corrosion, liquid deposits are able to still form below the melting point of Na_2SO_4. This can be explained from the $CoSO_4$-Na_2SO_4 phase diagram shown in Figure 26 below.[63]

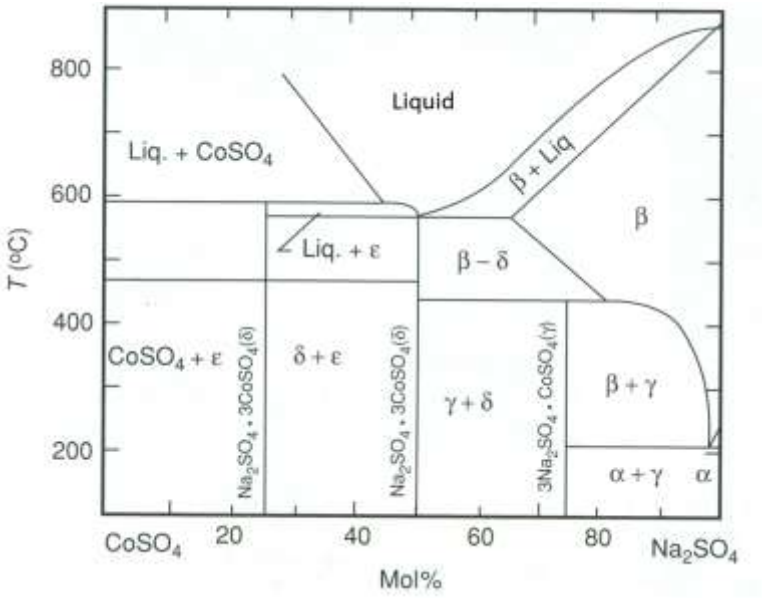

Figure 26: The $CoSO_4$-Na_2SO_4 phase diagram

A eutectic liquid can be seen on the diagram at approximately 50% Na_2SO_4 at 560^oC. Therefore, if sufficient amounts of $CoSO_4$ can form in the Na_2SO_4 deposit, then a liquid will form in the low temperature 650-750^oC range.

MCrAlY materials oxidized at high temperatures usually will form a slow growing protective α-Al_2O_3 scale on its surface. Even though Al_2O_3 is the oxide that will preferentially grow on the substrate of these alloys, a small amount of MO (NiO or Co_3O_4) will grow initially before the protective Al_2O_3 scale can, because these oxides grow much faster than Al_2O_3. This is known as transient oxidation.[30] A CoCrAlY coating covered with a Na_2SO_4 deposit will have transient Co_3O_4 or CoO, depending on temperature, growing first. The transient cobalt oxides can then react with SO_3 in the gas atmosphere to form the liquid Na_2SO_4-$CoSO_4$ eutectic melt. The reactions for this are given in equations 38 and 39 below.[64]

$$1/3\ Co_3O_4 + SO_3 = \underline{CoSO_4} + 1/6\ O_2 \qquad (38)$$

$$CoO + SO_3 = \underline{CoSO_4} \qquad (39)$$

$CoSO_4$ is underlined because it will dissolve in the Na_2SO_4 at an activity of less than one, and if there is enough SO_3 present in the gas atmosphere to cause the formation of sufficient amounts of $CoSO_4$, then the liquid eutectic melt can form. The amount of SO_3 needed in the gas atmosphere to cause the formation of the eutectic melt from Co_3O_4 p_{O2} = 1atm was calculated by Shores and Luthra[64] and is shown in the plot in Figure 27 below as a function of temperature.

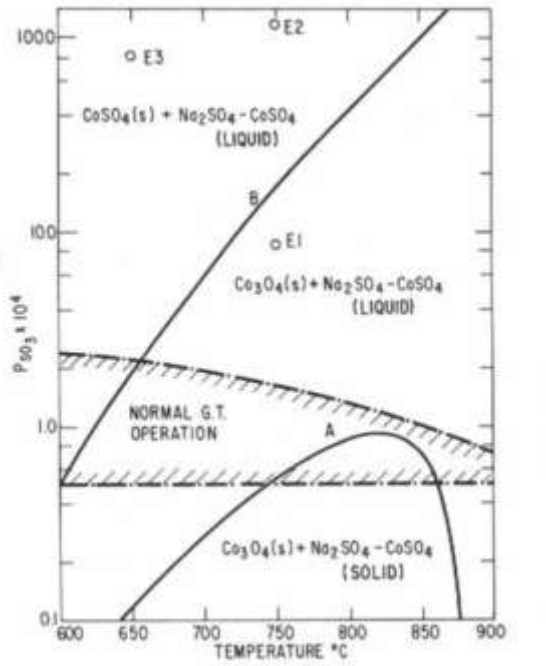

Figure 27: The SO_3 partial pressure required to form various species

The Na_2SO_4-$CoSO_4$ liquid eutectic is stable above the solid line in the plot marked A. The amount of SO_3 present in common gas turbine operating conditions is marked on the plot by the dashed line area. As can be seen, the liquid eutectic is stable at a wide range of SO_3 partial pressures within the normal gas turbine operating conditions. This plot is for p_{O2} = 1 atm, and the curves will change with the oxygen partial pressure as can be seen in the equilibrium reaction given in equation 38. Even with significant increases in the oxygen partial pressure, curve A in the plot will only slightly increase, and therefore this plot is still valid for most situations.

Sulfur dioxide and sulfur trioxide both exist in combustion gas atmospheres. The formation of SO_3 comes from the oxidation of SO_2, which has been explained earlier. The reaction is given by equation 4. As was discussed earlier, this reaction is very temperature dependent with SO_2 being favored at high temperatures and SO_3 at lower temperatures. Jones studied the interaction between Co_3O_4 and SO_2/SO_3 gas mixtures.[63] He determined that SO_3

was the gas species responsible for turning Co_3O_4 into $CoSO_4$ and not SO_2. It was also discovered that Co_3O_4 is a good catalyst for reaction 4. Even in a gas atmosphere containing only SO_2, significant amounts of eutectic liquid will form due to Co_3O_4 catalyzing the SO_3 reaction.

The corrosion mechanism for low temperature Type II hot corrosion of Co-based alloys was proposed by Luthra.[64] The SO_3 levels needed to form the eutectic liquid on the surface of the metal and cause corrosion would dissolve the protective Al_2O_3 and Cr_2O_3 scales as sulfates and therefore basic fluxing is not possible. The SO_3 is consumed at the oxide/salt interface, and therefore the SO_3 partial pressure is lower here than at the salt/gas interface. The solubility gradient at the oxide/salt interface would be positive, so acidic fluxing of the Al_2O_3 or Cr_2O_3 cannot occur. The fluxing of the protective oxide scale as was described in alloy-induced acidic fluxing is not applicable here. The transport rates of oxygen, SO_2, and SO_3 through the liquid salt were calculated, and it was found that only SO_3, which is present as $S_2O_7^{2-}$ ions, is the primary oxidant at the oxide/salt interface, and is the reason for the increased oxidation rates. SO_3 becomes part of the salt deposit by the reaction given in equation 40 below.

$$Na_2SO_4 + SO_3 = Na_2S_2O_7 \qquad (40)$$

Luthra[64] explains that it is then transported to the salt/gas interface by an $SO_2O_7^{2-}/SO_4^{2-}$ exchange reaction given in equation 41 below.

$$S_2O_7^{2-} + SO_4^{2-} + SO_4^{2-} = SO_4^{2-} + S_2O_7^{2-} + SO_4^{2-} \qquad (41)$$

Cobalt oxides are commonly found at the corrosion product/gas interface, therefore they must transport somehow through the molten salt. Luthra also proposed a mechanism to explain this.[64] Cobalt is able to exist in a 2+ or 3+ valence state. The outward migration of Co ions requires the coupled movement of additional ions in order to preserve electrical neutrality. There

are three proposed migration possibilities. The first involves the simultaneous outward diffusion of Co^{2+} and SO_4^{2-}. This requires the activity of $CoSO_4$ be highest at the metal/oxide interface. At high concentrations of SO_3, $CoSO_4$ forms at unit activity at the salt/gas interface, and so the activity gradient needed for this reaction to occur is not possible, and therefore this migration mechanism is not possible. The second migration mechanism proposed is the simultaneous outward diffusion of Co^{2+} and SO_3^{2-}. The partial pressure of oxygen is low, and there should be a negative SO_3^{2-} gradient at the oxide/salt interface. This is shown by the reaction given in equation 42 below.

$$Na_2SO_3 + ½\ O_2 = Na_2SO_4 \qquad (42)$$

The calculated maximum flux for this mechanism is much smaller than the observed flux of cobalt. This confirms that this is not the mechanism for Co migration. The third mechanism for the migration of Co is a $3Co^{2+}/2Co^{3+}$ exchange reaction. The ratio of Co^{3+}/Co^{2+} in the molten salt is given by the reaction in equation 43.

$$2CoSO_4 + SO_3 + ½\ O_2 = Co_2(SO_4)_3 \qquad (43)$$

The partial pressures of oxygen and SO_3 are lower at the oxide/salt interface than at the salt/gas interface; therefore the Co^{3+}/Co^{2+} ratio should be higher at the salt/gas interface. This causes an outward migration of Co^{2+} ions that will form Co_3O_4 or $CoSO_4$ depending on the oxygen and SO_3 partial pressures at the salt/gas interface. Co^{3+} ions will migrate inward, where they will be reduced to Co^{2+} at the oxide/salt interface. This is the correct Co migration mechanism.

Using this Co migration mechanism, a sequence of reactions was developed to describe the mechanism of gas-phase induced acidic fluxing.[64] A binary Co-Cr alloy was used as the example material. During the beginning stages of oxidation, transient Co oxides and Cr_2O_3 will form. Cr_2O_3 is more stable than Co_3O_4, so an alloy containing sufficient amounts of Cr would

eventually form a continuous, slowly growing, protective Cr_2O_3 scale. The dissolution of this protective scale is the reason for increased corrosion. The transient Co_3O_4 that initially forms will react with SO_3 in the gas to form $CoSO_4$ which will dissolve in the Na_2SO_4 salt deposit. If sufficient SO_3 is available, then a liquid Na_2SO_4-$CoSO_4$ eutectic will form leaving behind a porous Cr_2O_3 scale. The reaction can continue with the inward migration of SO_3 and the outward migration of Co^{2+} as was discussed earlier. The inward migrating SO_3 oxidizes the Cr at the oxide/salt interface releasing SO_2, which can penetrate into the alloy and form sulfides. Sulfide rich bands are commonly found at the base of corrosion pits. The sulfide band that formed can be further oxidized generating S_2, which can penetrate further into the alloy to form additional sulfides. The sulfide band and the corrosion pit are able to progressively go further into the alloy substrate. Eventually the maximum $CoSO_4$ activity is reached at the salt/gas interface and the outward migrating cobalt will form Co_3O_4. This mechanism can be applied to Co-Al and CoCrAl alloys. Luthra[64] explained that the mechanism described above is not likely for Ni-based alloys because nickel does not have any known Ni^{3+} compounds, even though Ni^{3+} is possible.

The mechanism for Ni-based alloys is similar and was described by Chiang et al.[62]. A binary Ni-Cr alloys is used as an example. Transient NiO grows over a protective Cr_2O_3 scale on the surface of the metal and react with SO_3 in the gas to form Ni_2SO_4. This will dissolve in the Na_2SO_4 deposit, and if there is sufficient SO_3 in the gas atmosphere, a liquid Na_2SO_4-Ni_2SO_4 eutectic will form and penetrate the Cr_2O_3 scale. High p_{SO2}/p_{S2} values are established at the alloy/salt interface due to low p_{O2} in this area. This leads to acidic fluxing of the protective

Cr_2O_3 scale and reprecipitation of a non-protective scale at places of higher p_{O2}. The base metal dissolves in the salt and diffuses to the salt/gas interface where it precipitates as NiO. The high p_{S2} at the alloy/salt interface results in the precipitation of CrS in the alloy.

Low temperature hot corrosion tests were conducted on Ni-Cr, Co-Cr, NiCrAl, and CoCrAl alloys at temperatures between 700-750^{o}C by Chiang et al.[62] They found that all of the alloys exhibited the degradation morphology similar to that for Co-Cr and CoCrAl described earlier. Even the Ni-based alloys observed severe degradation, but higher SO_3 pressures were required for this to occur when compared to Co-based alloys. Chromium sulfides were found at the base of the pits of the Ni-based alloys, along with NiS in the corrosion product. Aluminum present in the alloy also seems to result in increased degradation, because the ternary Co-18Cr-6Al alloy sustained more degradation than the binary Co-20Cr at a given SO_3 partial pressure. With these results, the authors proposed a Type II hot corrosion mechanism. As was discussed before, a liquid eutectic salt is formed from the reaction of transient NiO or Co_3O_4 with SO_3. High values of p_{SO2} and p_{S2} are established at the oxide/salt interface because of low p_{O2} in this region. The acidic fluxing of the protective Al_2O_3 scale for CoCrAl alloys is given by the reaction in equation 44 below.

$$Al_2O_3 + 3SO_2 = Al_2(SO_3)_3 \qquad (44)$$

Aluminum sulfite is dissolved into the molten salt and is then reprecipitated out at porous Al_2O_3 in the outer region of the molten salt where the SO_2 partial pressure is low. Chromium may undergo a similar reaction, or it may be oxidized in-situ. As was discussed earlier in the mechanism by Luthra, Co diffuses through the liquid salt and forms Co-oxide at the salt/gas interface. This mechanism is consistent with the observed preferential attack of the Al-rich β-phase in the alloy. The mechanism is a bit different for NiCrAl alloys. The important reaction is

at the oxide/salt interface in the substrate between Cr, Al, and S forming sulfides. These sulfides then oxidize and S_2 is released which form NiS and dissolve into the molten salt. This allows Ni to diffuse to the salt/gas interface forming the non-protective NiO.

The morphology and mechanisms of Type II hot corrosion described here and encountered in the performed research will be compared to the severe pitting attack observed in fireside corrosion tests. Both of these types of tests were conducted at low temperatures (650-700^{o}C), with the only difference being the type of deposit and the varying amounts of SO_3 in the gas atmosphere. The results of the fireside corrosion tests and the Type II hot corrosion tests will also be compared to the Na_2SO_4 induced corrosion of the so-called disk alloys. Some of these contain Mo, which might exhibit Type I characteristics even at a low temperature. This will all be discussed further in the results and discussion sections.

2.4.4 Disk Corrosion

Advanced gas turbine engines are currently being developed for reduced gas emissions and reduced fuel consumption (higher efficiency). This can be done by increasing the combustion temperature and pressure or improvements in cooling technologies. Not only will the temperatures and pressures of the turbine blades be increased, but the temperatures and pressures surrounding the disk rotors will also increase. Currently high strength nickel alloys are used for disk rotor hardware because of their high temperature oxidation resistance and strength. Exposing disk alloys to engine environments for long periods of time will cause severe oxidation and hot corrosion due to salt deposits as discussed earlier. Increasing the temperature and pressure will have even greater effects on disk integrity.[65]

Encinas-Oropesa et al.[65] studied the oxidation behavior of a new disk alloy, RR1000, which is a nickel-based superalloy with composition Ni-18.5%Co-15%Cr-5%Mo-3.6%Ti-3%Al-2%Ta-0.5%Hf and trace other elements. It is important to note the addition of 5%Mo. As has been discussed previously and will be shown later, the addition of Mo to these alloys can caused increased degradation even at these low temperatures. Encinas-Oropesa et al. oxidized RR1000 isothermally and cyclically in air at temperatures between 700-800^{o}C. The results showed that a very thin Cr_2O_3 oxide scale grew with parabolic kinetics. The thickness of the oxide scales increased with increasing temperature. There was also some sub-surface damage beneath the growing oxide scales which contained grain boundary pores and a second phase depletion zone.

The research presented in this thesis compares the low temperature oxidation (700^{o}C) as well as Na_2SO_4 induced Type II hot corrosion morphologies and mechanisms of RR1000 as well as some other model and commercial Ni-based disk alloys. This mechanism will then be compared to the Type II hot corrosion of selected Ni-based alloys as well as the fireside corrosion mechanisms. All of these tests were conducted at 700^{o}C, so a clear understanding of the different corrosion mechanism as a result of salt deposits will be achieved.

3.0 RESEARCH OBJECTIVES

The current materials used in the superheater and reheater sections of coal-fired boilers do not have the high temperature strength and corrosion resistance needed for advanced ultra-supercritical power plants. In order to increase plant efficiency and reduce CO_2 emissions advanced coal-fired power plants will operate under higher temperatures and pressures and using oxy-fuel combustion processes. This will cause the plants to be operating in the ultra-supercritical range of 35MPa and 760^{o}C, and with oxy-firing, a gas atmosphere with increased SO_3 and CO_2. Deposits from the coal react with SO_3 from the gas atmosphere in this temperature range to cause severe liquid-phase corrosion. This type of corrosion called fireside corrosion is not well understood. The first goal of this research was to provide high temperature fireside corrosion information as well as indicate a corrosion mechanism to aid in materials development for oxy-fuel combustion systems.

Advanced gas turbine engines are also being developed for higher temperatures in order to increase efficiency. The mechanisms for the different types of hot corrosion caused by Na_2SO_4 deposits have been established. There are some gray areas, however, regarding the conditions that cause the different types of hot corrosion. The second goal of the performed research was to compare the conditions and mechanisms for different types of hot corrosion as

well as fireside corrosion and corrosion of disk alloys. This will provide more information on the conditions needed for the different types of corrosion, and may allow different types of corrosion to be combined into the same category under certain conditions.

4.0 EXPERIMENTAL PROCEDURE

4.1 MATERIALS PREPARATION

The compositions of all of the alloys tested are shown below in Table 5.

Table 5: Nominal Alloy Compositions (wt%)

	Ni	Fe	Co	Cr	Al	Mo	Ti	W	Other(Nb, Ta, Hf, Y)
NiCrAlY	Balance	-	-	21	14	-	-	-	0.7Y
CoCrAlY	-	-	Balance	21	14	-	-	-	0.7Y
NiCrAl	Balance	-	-	8	6	-	-	-	-
NiCrAlMo	Balance	-	-	8	6	6	-	-	-
IN-738	Balance	-	8.5	16	3.5	1.75	3.5	2.5	1.75Ta, 0.8Nb
IN-617	Balance	-	12	22	1.2	9	0.3	-	-
T92	0.32	Balance	-	8.84	-	0.32	-	1.83	-
FeNiCr	12	Balance	-	18	-	-	-	-	-
NiCr	Balance	-	-	22	-	-	-	-	-
RR1000	Balance	-	18.5	15	3	5	3.6	-	2Ta, 0.5Hf

The NiCrAlY, CoCrAlY, NiCrAl, and NiCrAlMo alloys were received as bars that could be cut into circular specimens. The NiCrAlY and CoCrAlY specimens were cut into coupons approximately 3mm thick and 18mm in diameter. The NiCrAl specimens were cut into coupons approximately 1.5mm thick and 18mm in diameter, while the NiCrAlMo specimens were slightly larger at approximately 1.5mm thick and 19.4mm in diameter. The remaining alloys

were cut into rectangular coupon specimens approximately 15mm x 10mm x 2mm. All of the specimens were polished to a 1200 grit SiC finish and ultrasonically cleaned in isopropanol. The specimens were then dried and weighed before any deposits were applied or testing was conducted.

There were two deposits used for the fireside corrosion tests. The deposits were prepared by thoroughly mixing the individual ingredients. The first deposit had a composition (wt%) of 30%SiO_2-30%Al_2O_3-30%Fe_2O_3-5%Na_2SO_4-5%K_2SO_4. This deposit was called Deposit D and will be referenced as such for the rest of this thesis. This deposit simulates the ash that can form in actual boiler systems. The second deposit had a composition of Na_2SO_4:K_2SO_4:Fe_2O_3 in a 1.5:1.5:1.0 molar ratio. This deposit composition was based on the work of Cain and Nelson[25], and was called the "standard corrosion mix", and will be called this for the rest of the thesis as well. The amounts of each component in the standard corrosion mix come from the stoichiometric values of the alkali iron trisulfates that form and cause corrosion. The standard corrosion mix is designed to form alkali iron trisulfates in the tested environment. It represents the most severe deposit that could occur. Several deposition procedures were used in covering the specimens. Deposit D was first used as a coating. A powder deposit was made into a 2M slurry in isopropanol (2 moles of powder in one liter of isopropanol). The slurry was magnetically stirred while resting on a hot plate. While stirring the slurry, the specimens were dipped into the solution, removed, and dried with a heat gun. This was repeated until 2.75±0.25 mg/cm^2 of slurry was coated onto the specimens. The second deposition procedure was simply keeping Deposit D and the standard corrosion mix in powder form and placing them into

alumina crucibles. The specimens were placed into the crucibles so that half of the specimen was covered in powder and half was not. This was done so that the effect of deposit thickness on the corrosion of the alloy could be determined.

The Type II hot corrosion tests used a different salt deposit and deposition procedure. These tests were conducted by Michael Task, and reported in his Masters and Ph.D. theses.[66-67] His procedure is referenced here, and the results of his work will be referenced in this thesis. Na_2SO_4, Na_2SO_4-$NiSO_4$, or Na_2SO_4-$CoSO_4$ eutectics were the salt deposit used depending on whether the NiCrAlY or CoCrAlY alloys were used. The eutectic salt deposits were made by mixing 80g of Na_2SO_4 powder per 16oz. of distilled water with $NiSO_4$ powder and $CoSO_4$ powder so that there was 38wt%$NiSO_4$ and 52wt%$CoSO_4$. A 2.75±0.25mg/cm^2 deposit was applied to the surface of the specimens by heating the specimens with a heat gun and spraying with the prepared eutectic salt solution. The specimens were weighed so that the desired amount was deposited on the surface. Tests were also conducted under Type II hot corrosion conditions on some model and commercial disk alloys. These tests used Na_2SO_4. The salt deposit mixture was made by mixing 80g of Na_2SO_4 powder per 16oz. of distilled water. A deposit of 2.75±0.25mg/cm^2 was applied to the surface of the specimens in the same manner as the eutectic salt deposits. The testing conditions were different for the fireside corrosion tests and the Type II hot corrosion tests, and they will be described in the following respective sections.

4.2 FIRESIDE CORROSION TESTS

The FeNiCr, T92, NiCr, NiCrAl, NiCrAlMo, and IN-617 alloys were selected for fireside corrosion tests. There were many tests conducted varying different parameters of the conditions

in order to find the environment that caused the most severe corrosion. Once the specimens had been deposited with the salt mixture, they were placed into a horizontal resistance-heated quartz tube furnace shown schematically in Figure 28.

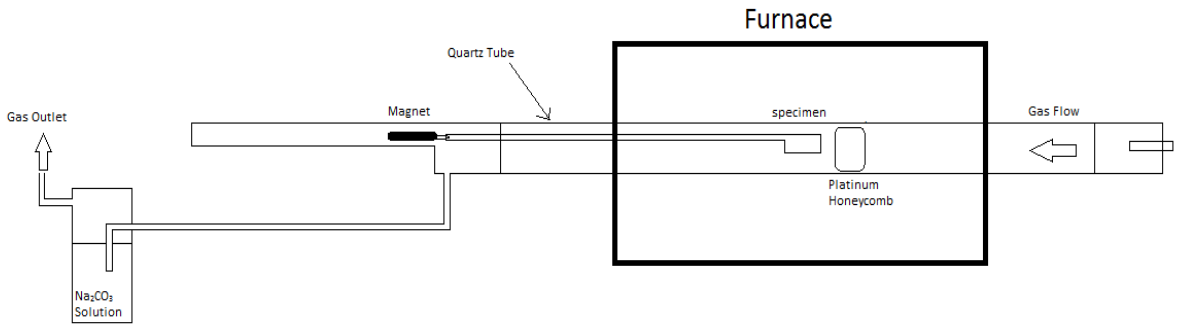

Figure 28: Schematic of horizontal tube furnace apparatus for fireside corrosion tests

The specimens could be cycled in and out of the hot zone of the furnace manually by using a magnet to push a quartz rod that held the specimens. The hot zone was maintained within 3 degrees of the test temperature. The gas atmospheres tested contained oxygen with varying amounts of SO_2. The gas flowed into the tube at a constant flow rate of 15mL/min (0.0125 cm/s) and passed over a platinum honeycomb catalyst placed in the hot zone of the furnace to establish the equilibrium p_{SO3} described earlier and given by the reaction in equation 4. Assuming that equilibrium is attained, the equilibrium p_{SO3} values for the temperatures and gas atmospheres tested are given in Table 6.

Table 6: Equilibrium SO_3 partial pressures at experimental temperatures and gas atmospheres

SO_3 Partial Pressure	O_2 + 100ppm SO_2	O_2 + 1000ppm $SO_{2=}$
650°C	4.856×10^{-4} atm	4.856×10^{-3} atm
700°C	2.524×10^{-4} atm	2.524×10^{-3} atm

When exiting the furnace, the gas is bubbled through a Na_2CO_3 plus water mixture before entering the fume hood. This removes the SO_3 from the gas, which is shown by the reaction in equation 45.

$$SO_3 + Na_2CO_3 = Na_2SO_4 + CO_2 \quad (45)$$

The produced sodium sulfate precipitates out in the bubbler, and the exiting gas is predominantly carbon dioxide.

As was mentioned before, the test conditions were varied to find the environment that caused the most corrosion. First, tests were conducted using the slurry deposition method. Following this, the powder-crucible method explained earlier was predominantly used. For this method, the quartz rod that was pushed by the magnet to place the samples in the hot zone was modified so that alumina crucibles could hang below it. This can be seen in the schematic shown in Figure 29.

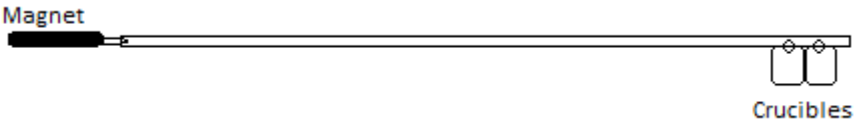

Figure 29: Modified quartz rod for crucible fireside corrosion tests

Using this method, tests were conducted at 650°C and 700°C in gas atmospheres containing O_2 + 100ppm SO_2 and O_2 + 1000ppm SO_2 with Deposit D and the Standard Corrosion Mix for 100-160 hours in order to find the most severe environment. In some tests the specimens were cycled in and out of the hot zone in 20 hour cycles, and others were conducted isothermally. The platinum catalyst was found to be too far from the hot zone in the initial experiments, and was moved closer to the samples. After every test was completed, the specimens were metallographically prepared for examination with lapping oil instead of water in order to preserve the corrosion products.

4.3 TYPE II HOT CORROSION TESTS

The Type II hot corrosion tests on the NiCrAlY and CoCrAlY alloys were conducted and the results were written by Michael Task.[66-67] The procedure for the tests was as follows. Following deposition of the eutectic salt mixture onto the surface of the specimens, Type II hot corrosion exposures were carried out at 700°C in a horizontal resistance-heated quartz tube furnace. The set-up is identical to the apparatus shown in Figure 28. As in the fireside corrosion tests, the specimens were cycled in and out of the furnace manually using the magnet to push the quartz tube holding the samples into the hot zone. The hot zone was maintained at 700°C ± 3°C.

The gas atmosphere tested contained O_2 + 1000ppm SO_2. The gas flowed into the quartz tube at a constant flow rate of 15mL/min (0.0125 cm/s) and over the platinum catalyst as described previously. Assuming thermodynamic equilibrium caused by the catalyst, the equilibrium p_{SO3} at 700^{o}C can be seen back in Table 6. Again, after each test, the specimens were metallographically prepared with water-free solutions.

Tests were also conducted on some model and commercial disk alloys. The alloys that were selected were NiCrAl, NiCrAlMo, IN-617, IN-738, and RR1000. These alloys were tested under the Type II hot corrosion conditions described above. The deposit on these samples was just Na_2SO_4. A test was also conducted under the same conditions, but with air instead of the SO_2 environment. A baseline test was conducted at 700^{o}C without any salt deposit in air so that the effect of the deposit on the oxidation of the alloys could be determined. Finally, a test was conducted on the Mo-containing alloys (NiCrAlMo, IN-617, and RR1000) at 650^{o}C with the salt deposit in air. This is below the melting point of sodium molybdate. This was done in order to test whether or not Mo additions to the alloys are causing increased corrosion in the absence of SO_3.

4.4 ANALYTICAL PROCEDURE

Weight change versus time measurements were calculated, but it is difficult to get an accurate measure of the degradation due to the nature of the deposits, so microstructural characterization was the main tool used. The surfaces of each of the specimens were viewed under the scanning electron microscope. The specimens were then metallographically prepared in water-free lubricants and viewed under the scanning electron microscope again so that cross-sectional

images could be taken. Two different SEMs were used. One is a Phillips XL-30 Field Emission Gun microscope. This microscope is equipped with secondary electron (SE), backscatter electron (BSE), and X-ray detectors and is thus capable of performing image acquisition and energy dispersive spectroscopic analysis (EDS). The other is a JEOL JSM-6610LV equipped with SE, BSE, and EDS. With the images and information gathered, a comparison the different morphologies and mechanisms of corrosion was then made.

5.0 RESULTS AND DISCUSSION

5.1 FIRESIDE CORROSION

5.1.1 Initial Tests: Finding the right corrosion environment

There were many tests conducted at the start of this project in order to identify the right set of conditions that would cause the most corrosion of the selected alloys in a relatively short amount of time. There are many variables which can affect the corrosion of the alloys. These include: temperature, deposit composition, gas atmosphere, duration of test, and cyclic heating. These different variables were all tested and the combined conditions that caused the most corrosion were determined. The goal of the tests was to simulate the atmosphere that actually occurs in coal-fired boilers. The deposits and the gas atmospheres used are much simpler than the actual conditions, but it is believed that the experimental conditions used for these tests are relevant in describing the corrosion occurring in coal-fired boilers.

5.1.1.1 Slurry Coating Deposition Tests

The first set of tests was conducted with the Deposit D mixture using the slurry coating method that was described in the experimental procedure section. It is known that the maximum amount of corrosion occurs in the 650-750^{o}C temperature range. This is based on previous studies in which a bell-shaped curve was observed for the corrosion rates, with the most severe

corrosion occurring in this temperature range.[4,14,17-18] Fireside corrosion tests were conducted on duplicate specimens of each of the alloys selected at 650°C and 700°C for 100 hours isothermally in a gas atmosphere containing O_2 + 100ppm SO_2 with Deposit D slurry coated onto the specimen. These tests did not cause any severe corrosion. This can be seen in the BSE micrographs shown in Figures 30 and 31. EDS analysis showed that a very thin oxide scale of transient Ni or Fe oxides and protective Cr or Al oxides grew depending on the alloy, with some remaining deposit covering the scale. The steel alloys had transient Fe-oxides and chromia scales. IN-617 and Ni-Cr had transient Ni-oxides and chromia scales, while the NiCrAl alloy had transient NiO as well as Cr and Al oxides.

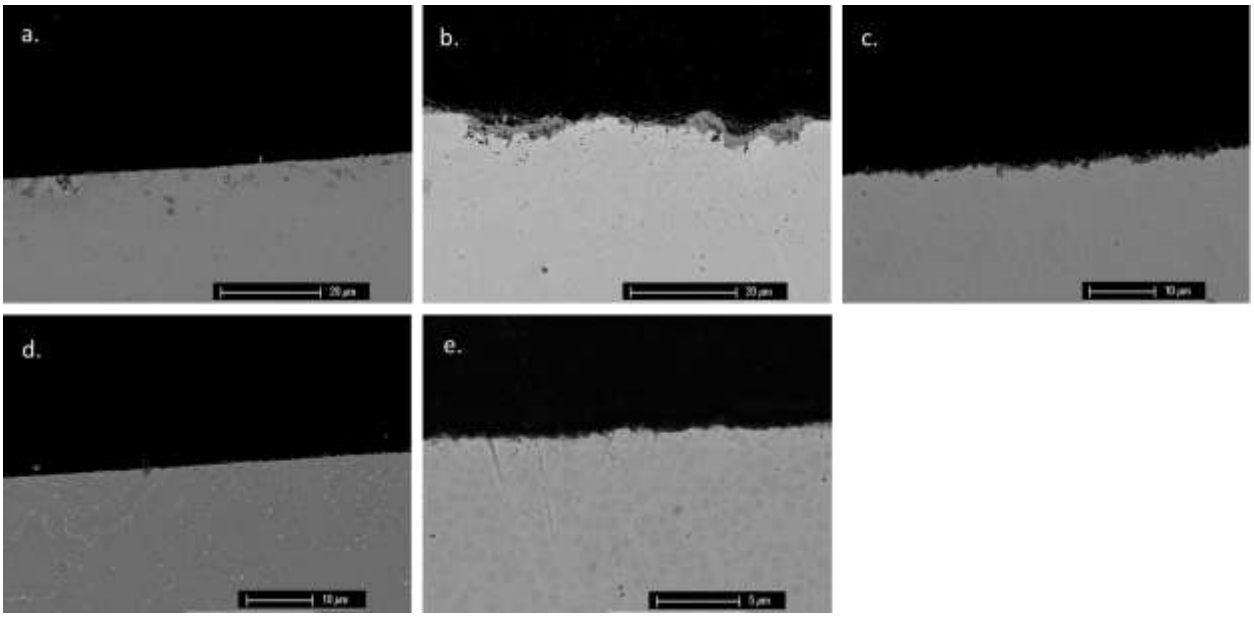

Figure 30: Fireside corrosion at 650°C with deposit D slurry coated in O_2 + 100ppm SO_2 for 100hrs for (a.) FeNiCr, (b.) IN-617, (c.) Ni-Cr, (d.) T92, and (e.) NiCrAl

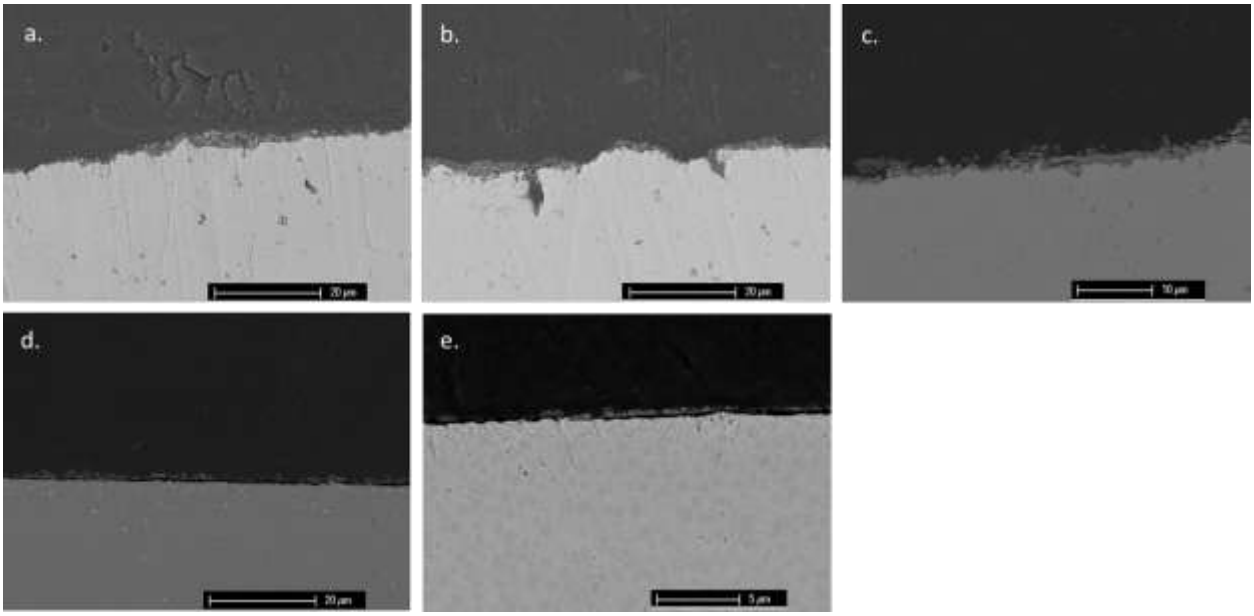

Figure 31: Fireside corrosion at 700°C with deposit D slurry coated in O_2 + 100ppm SO_2 for 100hrs of (a.) FeNiCr, (b.) IN-617, (c.) Ni-22Cr, (d.) T92, and (e.) NiCrAl

5.1.1.2 Powder-Crucible Deposition Tests

The test environment was then altered, because there was no significant corrosion occurring under the previous conditions. The slurry coating method was replaced by the powder-crucible method explained in the experimental procedure section. This was done so that the effect of deposit thickness could be analyzed. Tests were conducted for all of the alloys as before at 650°C in O_2 + 100ppm SO_2 with Deposit D for 100 hours. This did not produce any significant corrosion either; however there was differences in the oxides grown based on deposit thickness. The results can be seen macroscopically in Figure 32 below.

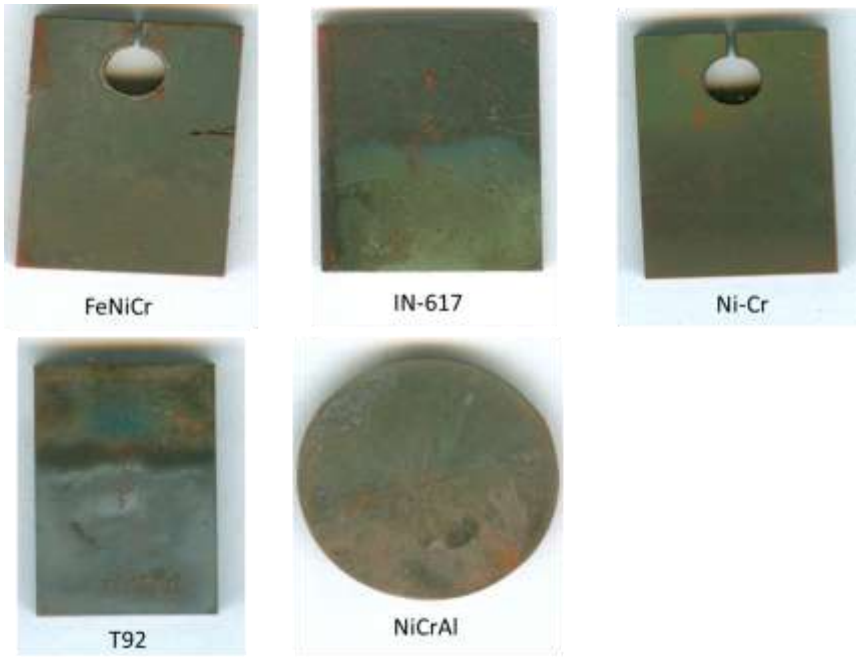

Figure 32: Fireside corrosion of selected alloys at 650^{o}C with deposit D powder in a crucible in O_2 + 100ppm SO_2 for 160hrs

With the powder-crucible deposition method, the effect of deposit thickness on the corrosion of the alloys can be seen. There are three main areas of each specimen that could be analyzed. There is a zone where there is no deposit, where the alloy was only exposed to the gas atmosphere. There is a zone where the powder starts to cover the specimen. This is equivalent to a thin deposit. Finally, there is a zone where the specimen is completely covered in deposit powder, which is equivalent to a thick deposit. With the different salt deposition method, the alloys grew transient Ni- and Fe- oxides and some protective Cr- and Al oxides depending on the alloy and on the location on the specimen. EDS analysis showed that in the region where there was no deposit on the specimen, some transient oxides grew, but there was predominantly a protective Cr- or Al- oxide scale. Where the deposit was the thickest on the specimen,

predominantly transient Fe- or Ni-oxides grew. In the region where there was a thin deposit, a transition from the protective Cr- or Al-oxides to transient Fe- or Ni-oxides could be seen. An example of this is shown for the Ni-Cr alloy in the BSE micrographs in Figure 33.

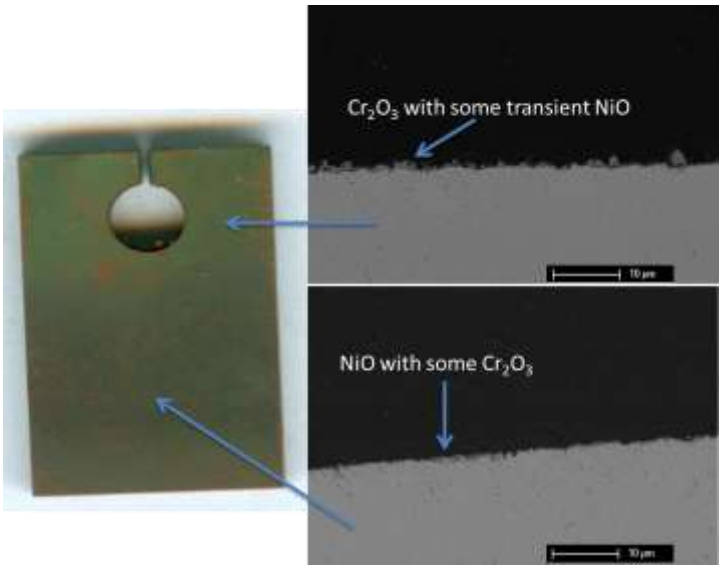

Figure 33: Fireside corrosion of Ni-22Cr at 650°C with deposit D powder in a crucible in O_2 +100ppm SO_2 for 160 hours

The early tests so far were only conducted for 100 hours. It is thought that under these conditions and given a sufficient amount of time, the specimens would become more severely corroded. The goal was to produce severe corrosion in a short time however; and therefore the test conditions were changed again. Deposit D was replaced by the more aggressive standard corrosion mix. It is believed that the large amounts of Al_2O_3 and SiO_2 were diluting the corrosive alkali sulfates in Deposit D. This is based on the work of Niles and Siegmund [68]. They tested kaolin ($Al_2O_3 \cdot 2SiO_2$) as an additive to deposits because it is effective in reacting with sodium. The alumina and silica inhibits the corrosion by absorbing the corrosive molten sulfates. The standard corrosion mix does not have any silica or alumina in it, and it should be a

very corrosive deposit. It has the corrosive alkali sulfates K_2SO_4 and Na_2SO_4 and catalytic Fe_2O_3 in a stoichiometric ratio 1.5:1.5:1.0 based on the reaction given in equation 9. A test was conducted on the T92 and NiCr alloys at 650°C with the standard corrosion mix powder in a crucible in O_2 + 100ppm SO_2 for 100 hours. This produced similar results to the specimens oxidized using Deposit D. BSE cross-sectional images of the deposit zone for the two alloys are shown in Figure 34.

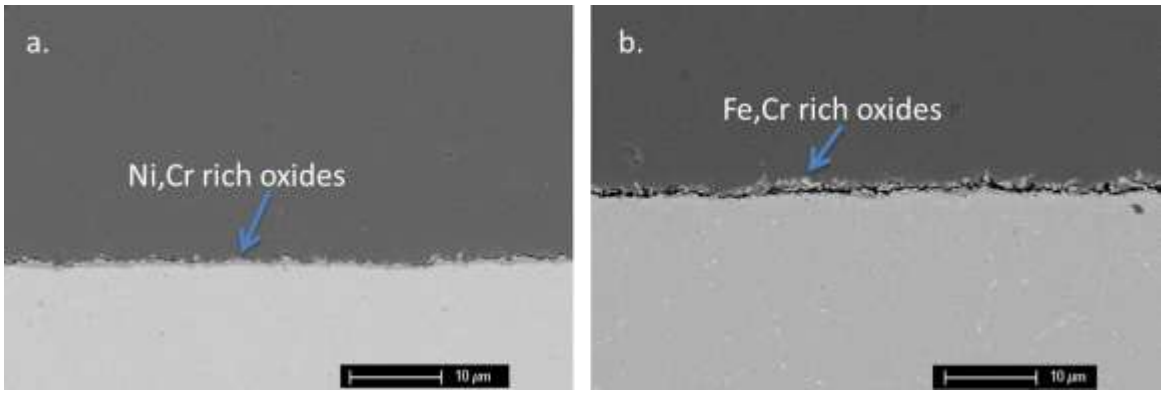

Figure 34: Fireside corrosion of (a.) Ni-22Cr and (b.) T92 at 650°C with the standard corrosion mix powder in a crucible in O_2 + 100ppm SO_2 for 100hrs

Short-term tests were the focus of this work, but it was thought that the length of the test should be increased slightly in order to cause more significant corrosion, so the duration of the remaining tests was increased to 160 hours. It was also determined that a single alloy should be chosen and used for each test until the proper conditions could be found. FeNiCr was the alloy chosen. A test was conducted on duplicate specimens at 650°C with the standard corrosion mix in O_2 + 100ppm SO_2 for 160 hours. This still produced negligible corrosion as can be seen from the BSE micrograph in Figure 35. EDS analysis showed that a very thin Cr_2O_3 scale formed over the alloy in the deposit zone.

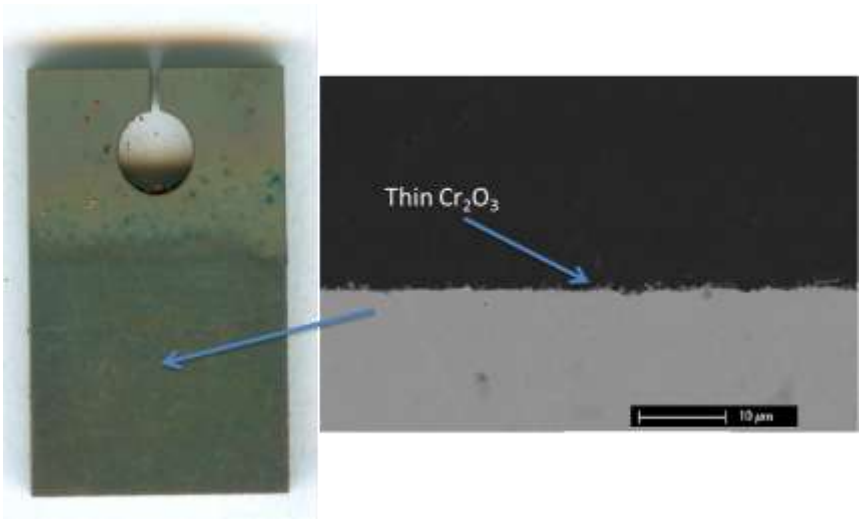

Figure 35: Fireside corrosion of FeNiCr at 650°C with the standard corrosion mix powder in a crucible in O_2 + 100ppm SO_2 for 160 hours

Following this, a test was conducted at 700°C under the same conditions, but the specimens were cycled in and out of the hot zone of the furnace in 20 hour cycles. It was believed that the higher temperatures and cycling of the specimens would cause increased corrosion and spallation. This was however not the case, as the results were very similar to the previous test at 650°C. This can be seen from the images in Figure 36. A small area in the thick deposit zone near the edge of the sample did produce a thicker Fe_2O_3 oxide scale; however there was still negligible corrosion.

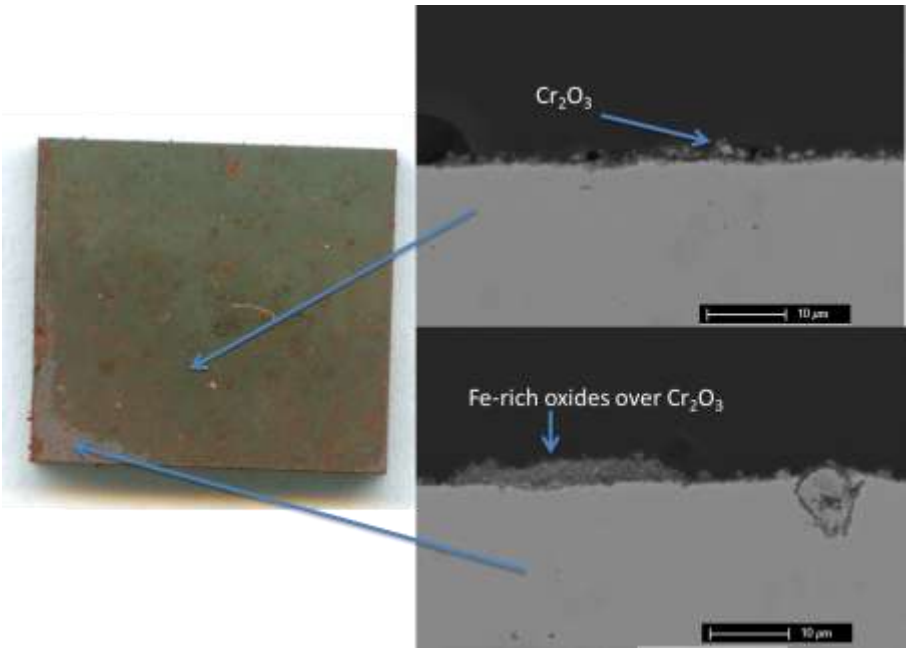

Figure 36: Fireside corrosion of FeNiCr at 700°C with the standard corrosion mix deposit in a crucible in O_2 + 100ppm SO_2 for 160 hours in 20 hour cycles

The most significant change in results came when the SO_2 content in the gas atmosphere was increased. Based on the work of Corey and Reid[26], at least 250ppm of SO_3 was needed to cause corrosion with a deposit of alkali sulfates and iron oxide at 1100°F (593°C). They found that at higher SO_3 concentrations, the reactivity of the deposits increases rapidly, and that adequate amounts of SO_3 are a major prerequisite for the formation of alkali iron trisulfates and severe corrosion. The temperatures used in the current work for this thesis were at higher temperatures. At these higher temperatures, the maximum amount of SO_3 that can be formed decreases and the SO_3 pressure required to form sulfates increases. As was mentioned earlier, SO_3 forms from the oxidation of SO_2, and catalysts can be used to speed up the reaction. From the previous tests, at 650-700°C the atmosphere of O_2 + 100ppm SO_2 ($p_{SO3} = 4.856 \times 10^{-4}$atm) does not have enough SO_2 to oxidize and form enough SO_3 to cause corrosion. The gas atmosphere was changed to O_2 + 1000ppm SO_2, which has a $p_{SO3} = 4.856 \times 10^{-3}$atm. The

increased amount of SO_2 along with the catalyst allow for the formation of sufficient amounts of SO_3 to cause corrosion. A test was conducted on duplicate specimens at 700°C with the standard corrosion mix deposit in a crucible in O_2 + 1000ppm SO_2 for 160 hours isothermally. These conditions showed some corrosion of the alloy. This can be seen from the macroscopic images shown in Figure 37.

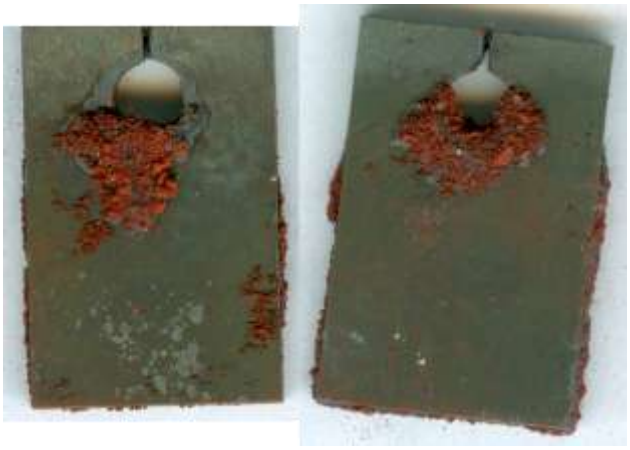

Figure 37: Fireside corrosion of FeNiCr at 700°C in O_2 + 1000ppm SO_2 with the standard corrosion mix powder in a crucible for 160 hours isothermally

The surfaces of the specimens were viewed under the SEM and analyzed using EDS. In the region where there was no deposit, spallation of protective chromium oxide occurred revealing base metal. Severe corrosion of the alloy occurred in the region where the deposit was the thinnest and near the edges of the specimen and hole in the specimen. In this region, a thick, porous, non-protective Fe_2O_3 scale grew with some deposit material covering it and alkali sulfates in the surrounding area. In the deposit zone where there was no corrosion, transient iron oxides grew over a protective chromium oxide with some thicker iron oxides starting to form. This can all be seen below in Figure 38.

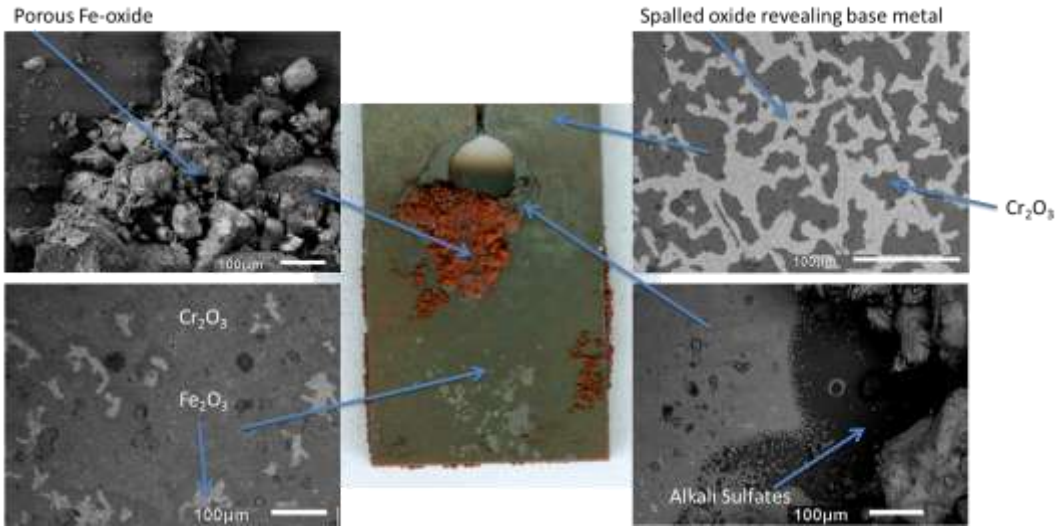

Figure 38: BSE surface SEM images of fireside corrosion of FeNiCr at 700°C in O_2 + 1000ppm SO_2 with the standard corrosion mix powder in a crucible for 160 hours isothermally

The specimens were metallographically prepared and a cross-section was viewed under the SEM and microscopic images are presented in Figure 39. The corrosion was in the form of deep pits. The pitting nature of the corrosion is similar to that which occurs for Type II hot corrosion. This will be discussed in a later section. The corrosion area has a very thick and porous external Fe_2O_3 scale. This turns into an internal oxide scale forming a sulfur-rich pit consisting of mixed chromium and iron oxides. The chromium and sulfur content increases with depth into the pit until at the scale/alloy interface the oxygen content drops off and chromium sulfides are present. This is typical fireside corrosion morphology. The mechanism describing fireside corrosion for each alloy will be discussed in subsequent sections.

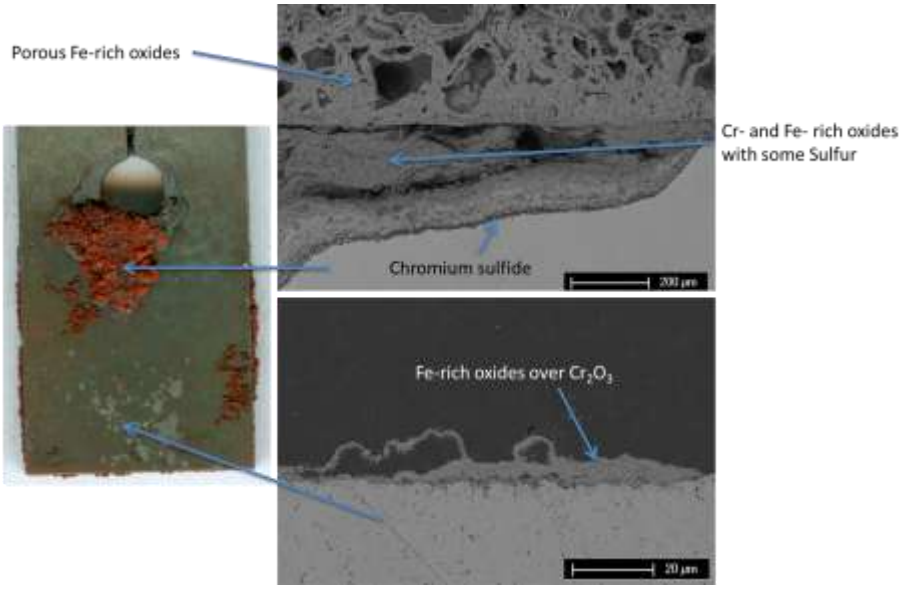

Figure 39: BSE cross-sectional SEM images of fireside corrosion of FeNiCr at 700°C in O_2 + 1000ppm SO_2 with the standard corrosion mix powder in a crucible for 160 hours isothermally

With the onset of corrosion occurring after the gas atmosphere was switched from O_2 + 100ppm SO_2 to O_2 + 1000ppm SO_2, it appears that there is a threshold level of SO_2 needed to form sufficient amounts of SO_3 to cause corrosion of the alloys at 700°C. This confirms previous research by Corey and Reid[69] explaining that sufficient SO_3 content in the gas atmosphere is a prerequisite for forming alkali iron trisulfates and therefore causing corrosion. From the research conducted to this point, the threshold level is believed to be between 100-1000ppm SO_2. Based on the success of this test, another one was conducted under the same conditions, but the specimen was cycled in the hot zone of the furnace in 20 hour cycles. The results were very similar, but the corrosion area penetrated further into the deposit covered zone. From these results, it was determined that cycling the specimens causes more severe corrosion.

Following this test, it was concluded that specimens in a gas atmosphere of O_2 + 1000ppm SO_2 for 160 hours in 20 hour cycles caused the most severe corrosion. The next test was conducted with this gas atmosphere for 160 hours with the standard corrosion mix but at

650°C. The kinetics of fireside corrosion has been found to follow a bell-shaped curve. The maximum in this curve occurs where sufficient amounts of SO_3 are able to form and where the largest amount of corrosion occurs. Depending on the results of this test, the temperature for the maximum in the bell-shaped curve can be narrowed down. The results of the test can be seen in Figure 40 below.

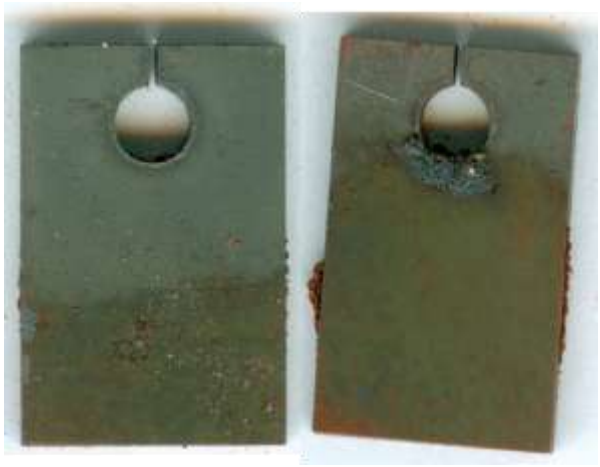

Figure 40: Fireside corrosion of FeNiCrAl at 650°C with the standard corrosion mix powder in a crucible for 160 hours in O_2 + 1000ppm SO_2

There is significantly less corrosion than there was at 700°C. This shows that the maximum in the fireside corrosion bell-shaped curve is greater than 650°C and is most likely near 700°C. A test was then conducted under the same conditions, but with no deposit in order to see the effect of the deposit on the alloy. The results are shown below in Figure 41.

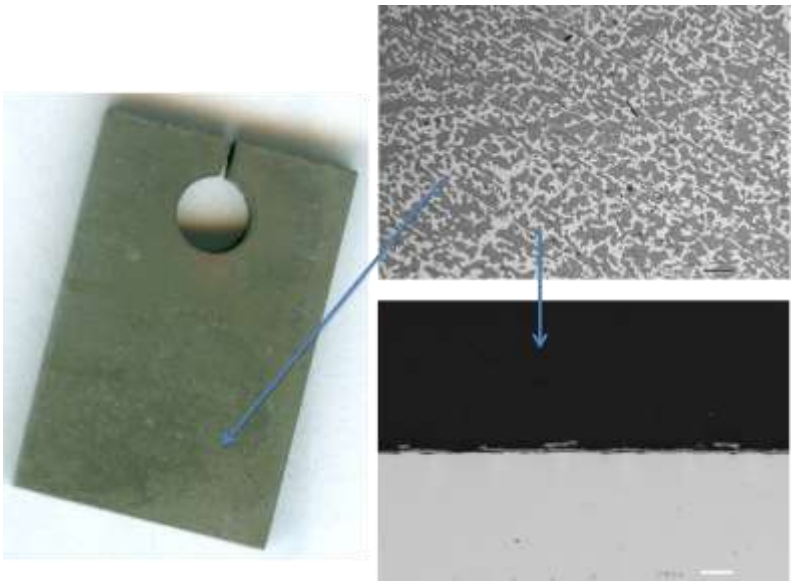

Figure 41: Oxidation of FeNiCr at 650^{o}C in O_2 + 1000ppm SO_2 with no deposit for 160 hours

The entire specimen has severe spallation of the protective chromium oxide scale. This is identical to the previous tests in the no deposit zone. This shows that this gas atmosphere causes increased spallation in the absence of a deposit, and that the standard corrosion mix causes severe corrosion of the alloy.

The test environment that caused the most severe corrosion of the specimens was determined to be 700^{o}C with the standard corrosion mix powder deposit in a crucible for 160 hours in 20 hours cycles in O_2 + 1000ppm SO_2. More alloys were then tested under these conditions so that the corrosion resistance of different alloys could be compared. The results for T92 and NiCr can be seen in Figures 42 and 43 respectively. Severe corrosion of the alloys occurred as with the FeNiCr alloy, with T92 suffering the most damage.

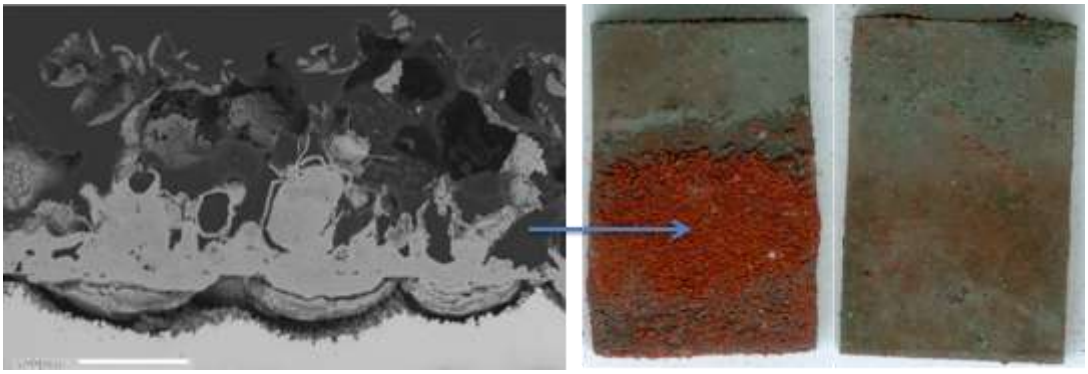

Figure 42: Fireside corrosion of T92 at 700°C with the standard corrosion mix powder in a crucible for 160 hours in 20 hour cycles in O_2 + 1000ppm SO_2

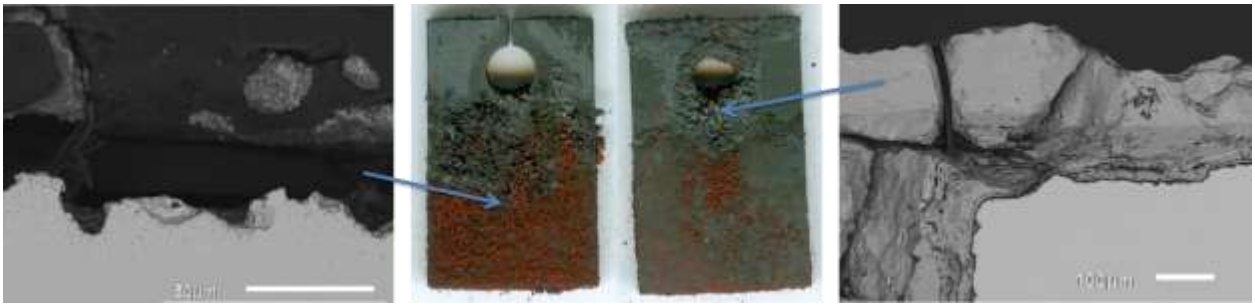

Figure 43: Fireside corrosion of NiCr at 700°C with the standard corrosion mix powder in a crucible for 160 hours in 20 hour cycles in O_2 + 1000ppm SO_2

While severe corrosion was occurring, it was discovered that one of the duplicate specimens tested for each of these tests had been corroding more than the other. The specimen placed in the second crucible downstream in the gas flow was corroding more than the first. It is believed that the platinum catalyst was placed too far out of the hot zone to catalyze significant amounts of SO_3. The first crucible was heating up the flowing gas and the Fe_2O_3 in the deposit was catalyzing this hot gas enough to cause corrosion of the specimen in the second crucible. The platinum catalyst was moved further into the furnace right next to the hot zone so that it was hot enough to catalyze the gas and cause corrosion of the specimens in both crucibles. After the catalyst was moved, the FeNiCr alloy was retested under the determined most severe corrosion

conditions and both specimens corroded significantly. Deposit D was retested under these conditions as well, and there was still no significant corrosion. This proved that the standard corrosion mix is the deposit that will cause the most corrosion. All of the alloys were retested at 700^{o}C with the standard corrosion mix powder in a crucible for 160 hours in O_2 + 100ppm SO_2 and O_2 + 1000ppm SO_2. The results and an examination of the morphologies and corrosion mechanisms will be performed for each alloy in the following sections.

Analysis of the initial test results show that the gas composition and equilibration of sufficient amounts of SO_3 is extremely important in causing corrosion. The Pt catalyst has to be in a hot enough zone to heat up the in-coming O_2 + SO_2 gas flow so that both specimens have enough SO_3 equilibrated to corrode. There must also be sufficient amounts of SO_2 in the gas atmosphere (100ppm or greater) so that enough SO_3 can be created. The analysis of the corrosion microstructure and mechanism of each of the alloys selected was for the observed environment that caused the most corrosion. This is at 700^{o}C with the standard corrosion mix deposit for 160 hours in O_2 + 1000ppm SO_2 (p_{SO3} = 4.856 $\times 10^{-3}$atm). The platinum catalyst was in close proximity of the specimen hot zone so that enough SO_3 was getting equilibrated to corrode both specimens.

5.1.2 FeNiCr

The results of the fireside corrosion tests on the FeNiCr alloy in O_2 + 100ppm SO_2 and O_2 + 1000ppm SO_2 are shown below in Figures 44 and 45 respectively.

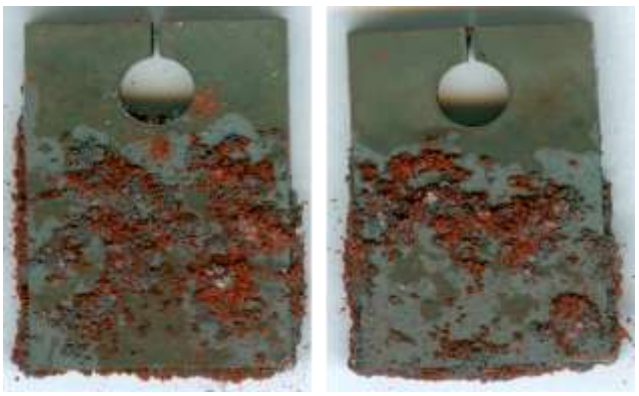

Figure 44: Fireside corrosion of FeNiCr at 700°C with the standard corrosion mix powder in a crucible for 160 hours in O_2 + 100ppm SO_2

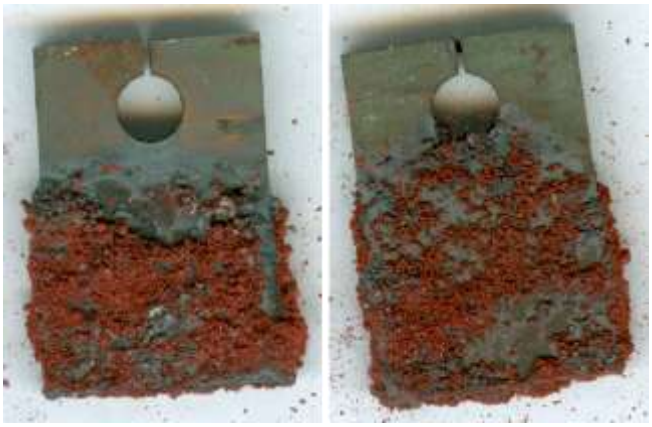

Figure 45: Fireside corrosion of FeNiCr at 700°C with the standard corrosion mix powder in a crucible for 160 hours in O_2 + 1000ppm SO_2

With the catalyst right next to the samples in the hot zone, both specimens corroded significantly, and there is corrosion even in the O_2 + 100ppm SO_2 gas atmosphere. The catalyst being closer to the hot zone is increasing the rate of reaction of the oxidation of SO_2 into SO_3.

This allows more SO_3 to be formed, and a lower amount of SO_2 is required in the gas atmosphere. The SO_2 threshold for the formation of sufficient amounts of SO_3 to cause alkali iron trisulfates to form must be close to 100ppm. At higher SO_2 concentrations, more SO_3 can form and the reactivity of the deposits increases rapidly causing more degradation. This also proves that the temperature of the catalyst plays a role in the amount of SO_3 that can form.

EDS analysis of microscopic images of the specimens showed that in the zone where there was no deposit and the specimens were exposed only to the gas atmosphere, a thin scale rich in Fe and Cr oxides grew, but there was spallation in this area as was discussed previously. It can be seen in Figures 44 and 45 that the entire deposit zone, from the region where the powder starts to cover the specimen to the region where the specimen is submerged in the deposit, was severely corroded. The corrosion morphology can be seen in Figure 46.

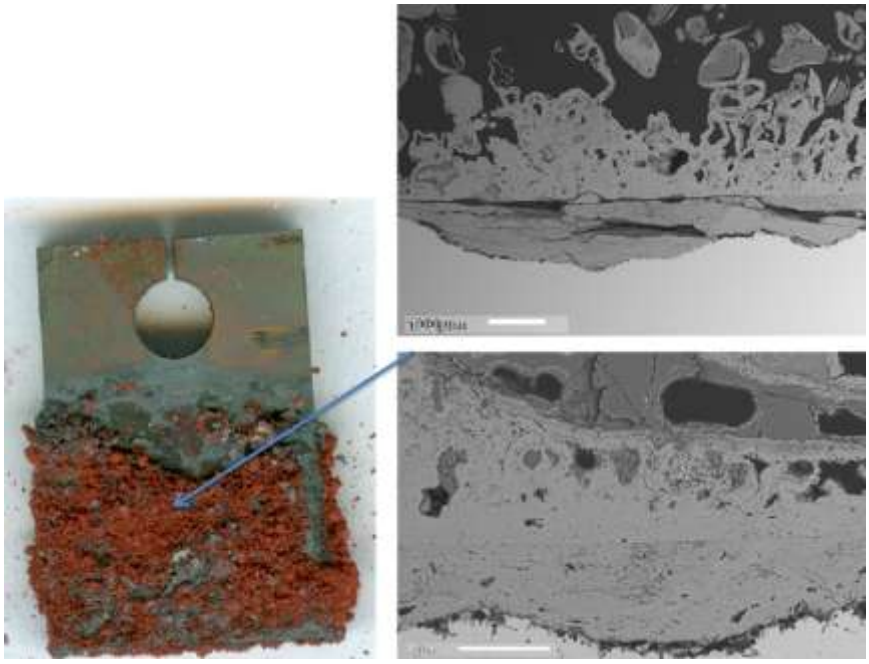

Figure 46: Fireside corrosion of FeNiCr at 700^{o}C with the standard corrosion mix powder in a crucible for 160 hours in O_2 + 1000ppm SO_2

Very thick, porous, non-protective, external Fe_2O_3 scales with some remnant deposit grew over more dense internal Cr-, S- and Fe- rich oxide scale forming pits that penetrate into the substrate. The more attack on the metal, the further into the substrate these pits penetrated. The chromium and sulfur content increases with depth into the pits until a layer of chromium sulfides form with some internal sulfidation.

The proposed corrosion mechanism for this alloy under these conditions can be described similarly to the images in Figure 12 and the description given from the work of Reid[14] in section 2.3.2. A transient iron oxide scale grows on the surface of the metal. The metal is covered by the standard corrosion mix deposit that consists of the alkali sulfates K_2SO_4 and Na_2SO_4 and iron oxide, Fe_2O_3. The gas atmosphere of $O_2 + SO_2$ flows over the platinum catalyst next to the hot zone where SO_3 is able to be formed. The SO_3 migrates through the deposit to the oxide/deposit interface where it reacts with the Fe_2O_3 oxide and the alkali sulfates in the deposit to form liquid alkali iron trisulfates. This consumes the protective iron oxide scale causing the metal to regrow a scale in the form of the porous non-protective iron oxide causing more metal wastage. This occurs by the reaction given in equation 18. The alkali iron trisulfates are consumed in regrowing the porous iron oxide scale. FeS and K_2SO_4 are also products of this reaction, and they are able to be recycled by oxidizing the FeS to SO_3 which will react with the K_2SO_4 and Fe_2O_3 to form more trisulfates. This cycle repeats indefinitely. The mechanism for the formation of the porous external Fe_2O_3 scale and the inward growing corrosion pits can be described similarly to the Type II hot corrosion mechanism for Co-based alloys described in Section 2.4.3.1. Inward migrating SO_3 can pass through the liquid alkali iron trisulfates via an

$S_2O_7^{2-}/SO_4^{2-}$ exchange reaction, where it will react with Cr in the substrate to form the inward growing Cr_2O_3 and CrS corrosion pits. The external Fe_2O_3 scale will simultaneously form via an $3Fe^{2+}/2Fe^{3+}$ exchange reaction similar to that for Co.

5.1.3 T92

The results of the fireside corrosion test with T92 at 700°C with the standard corrosion mix powder in a crucible for 160 hours in O_2 + 100ppm SO_2 and O_2 + 1000ppm SO_2 are shown below in the macroscopic images in Figures 47 and 48 respectively. There was noticeably more corrosion of T92 than of FeNiCr. T92 is a boiler steel that is not as corrosion resistant as the model Fe-12Ni-18Cr austenitic stainless steel. T92 has half of the amount of Cr (9%) and minimal amounts of Ni compared to the model FeNiCr. It was discussed previously that increasing chromium contents increases the corrosion resistance of the alloy. Ni also adds increased corrosion resistance to the FeNiCr alloy. With this information, T92 would not be expected to perform as well. Significant corrosion occurred even in the lower SO_2 atmosphere. It was determined that the SO_2 threshold for the formation of alkali iron trisulfates must be closer to 100ppm SO_2 based on the results of the FeNiCr alloy. Due to the decreased corrosion resistance of T92, once the alkali iron trisulfates formed, more degradation occurred.

Figure 47: Fireside corrosion of T92 at 700°C with the standard corrosion mix powder in a crucible for 160 hours in O_2 + 100ppm SO_2

Figure 48: Fireside corrosion of T92 at 700°C with the standard corrosion mix powder in a crucible for 160 hours in O_2 + 1000ppm SO_2

Observation of the micrographs of the corroded specimens and EDS analysis, indicated that the zone where there was no deposit, and the metal was exposed to the gas atmosphere only, still produced some significant corrosion with pits protruding into the substrate under a thick porous iron oxide scale. The entire zone covered in deposit was severely corroded, even where the deposit was thin. The morphology of the corrosion of the T92 specimens is similar to the FeNiCr alloy but more extreme as can be seen in Figure 49 below.

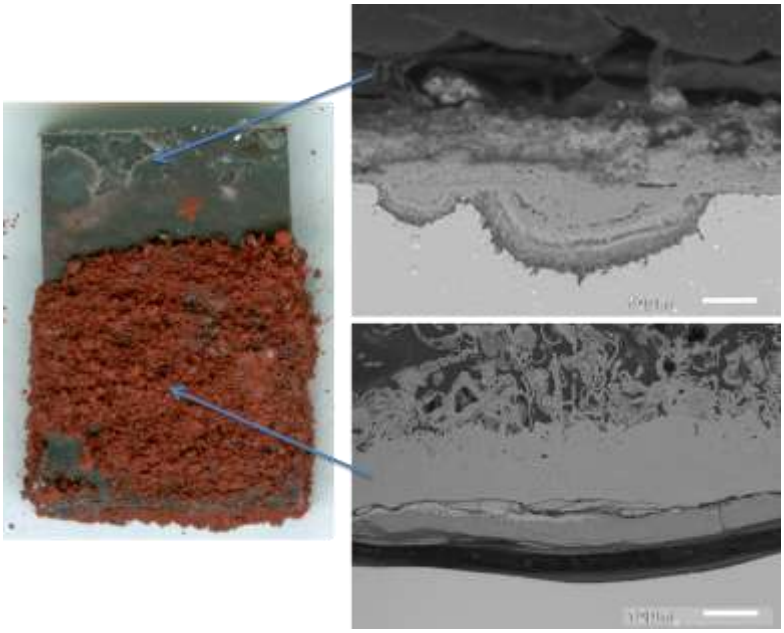

Figure 49: Fireside corrosion of T92 at 700°C with the standard corrosion mix powder in a crucible for 160 hours in O_2 + 1000ppm SO_2

The corrosion of T92 is much greater than that of the model FeNiCr alloy. Corrosion pits similar to those found in the deposit zone of the FeNiCr alloy can be seen in the zone where there is no deposit. In this zone, where there was no pitting, a thick non-protective iron oxide grew. The pits were composed of a very porous, non-protective, external iron oxide scale. This turns into an internal oxide scale that is more Cr and S rich. The chromium and sulfur contents increase with depth into the pit until, at the base, a layer of chromium sulfides forms. In the deposit zone, the corrosion is significantly worse. It appears as though such severe pitting occurred that the pits combined for a more frontal attack on the alloy forming a larger corrosion layer. The composition of the corrosion products are the same. A rather thick porous iron oxide grows over a scale with increased chromium and sulfur content, which increases until a chromium sulfide layer forms. The degradation and attack is much further into the substrate than the FeNiCr alloy, and therefore the corrosion is much more severe. The mechanism for the corrosion of the T92 alloy is believed to be the same as that for the FeNiCr alloy.

5.1.4 Ni-Cr

The results of the fireside corrosion test with Ni-22Cr at 700^{o}C with the standard corrosion mix powder in a crucible for 160 hours in O_2 + 100ppm SO_2 and O_2 + 1000ppm SO_2 are shown below in Figures 50 and 51 respectively. There was not as much degradation of the Ni-Cr alloy as there was in the Fe-based alloys. This is as expected. Ni-based alloys have better high temperature oxidation and corrosion resistance than Fe-based alloys due to their slower oxide growth rates. This alloy also has a higher chromium content (22%) than the Fe-based alloys providing it with even more corrosion resistance. There was also not as much corrosion in the O_2 + 100ppm SO_2 gas atmosphere. As was mentioned previously, the SO_2 threshold level for the formation of enough SO_3 to cause alkali iron trisulfates was determined to be close to 100ppm SO_2 based on the FeNiCr results. This threshold level should not change, but the increased corrosion resistance of the Ni-based alloys prevents the alkali iron trisulfates from causing severe degradation that occurred with the steel alloys. Higher SO_3 (1000ppm SO_2) concentrations causes the reactivity of the deposits to increase enough so that some degradation occurs. This was the case for all of the Ni-based alloys tested.

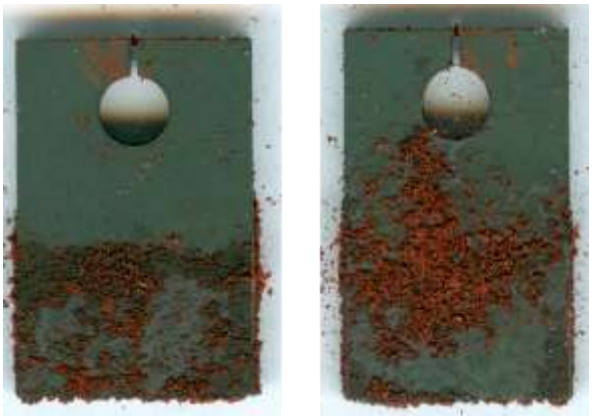

Figure 50: Fireside corrosion of Ni-22Cr at 700°C with the standard corrosion mix powder in a crucible for 160 hours in O_2 + 100ppm SO_2

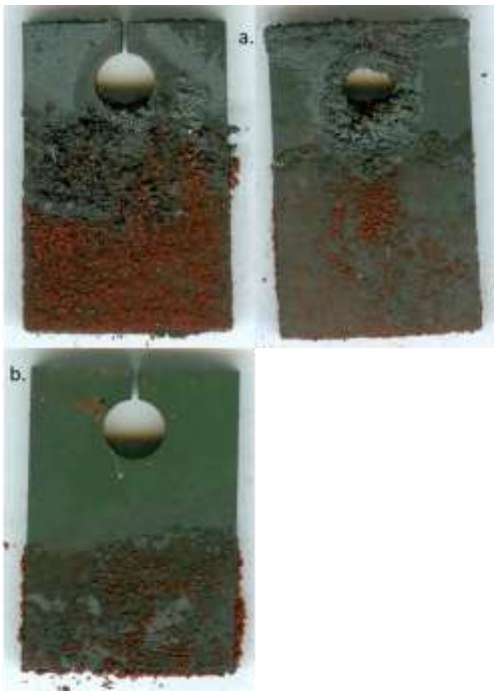

Figure 51: Fireside corrosion of Ni-Cr at 700°C with the standard corrosion mix powder in a crucible for 160 hours in O_2 + 1000ppm SO_2 (a.) before the platinum catalyst was moved next to the hot zone and (b.) after the platinum catalyst was moved next to the hot zone

The images shown in Figure 51 are of the specimens tested before and after the platinum catalyst was moved next to the hot zone. Before the catalyst was moved, corrosion was occurring in the deposit zone on one of the duplicate specimens only. This was not the case after

the catalyst was moved closer to the hot zone. Microscopic analysis showed that in the zone where there was no deposit and the metal specimen was exposed to the gas atmosphere only, a protective Cr_2O_3 scale grew. There was significant corrosion in the areas covered by the deposit with the most corrosion occurring where the deposit was the thinnest. The corrosion morphology is shown below in Figure 52.

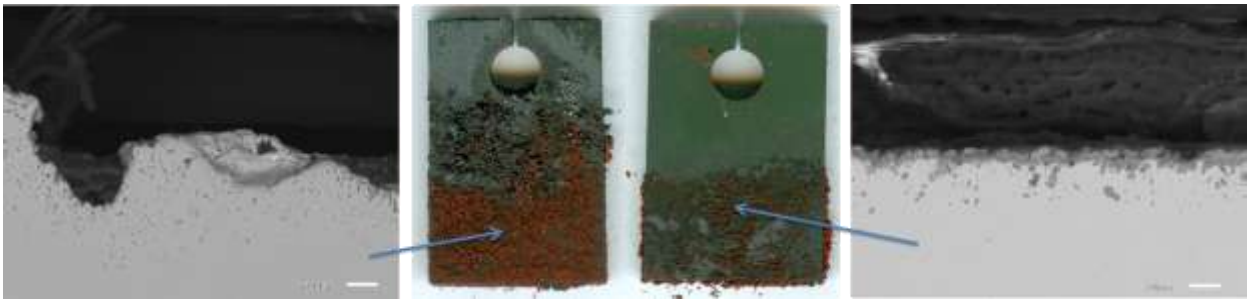

Figure 52: Fireside Corrosion of Ni-22Cr at 700°C with the standard corrosion mix powder in a crucible for 160 hours in O_2 + 1000ppm SO_2

The corrosion is similar in both the specimens before and after the catalyst movement. An external NiO scale grew over a thin Cr_2O_3 scale which turned into internal Cr_2O_3 growth with significant chromium sulfide formation penetrating into the substrate. The sulfides appear to be a precursor to further corrosion and pitting into the substrate. The micrographs in Figure 50 show that the pitting and corrosion was not as severe as the Fe-based alloys. As will be seen in a later section, the appearance of chromium sulfides is common for Ni-based alloys under hot corrosion conditions.

One of the specimens tested before the catalyst movement did not corrode significantly in the deposit zone, however it did show severe corrosion in the areas around the edges of the hole of the specimen and around the top edge. This can be seen in Figure 53.

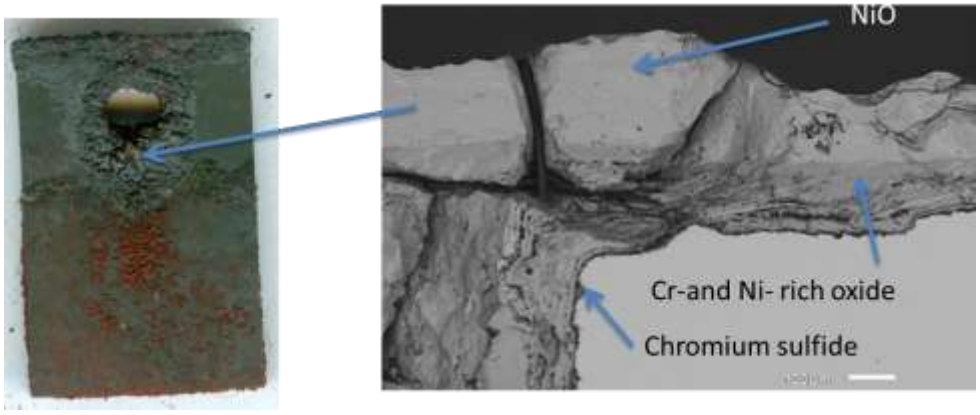

Figure 53: Fireside corrosion of Ni-22Cr at 700°C with the standard corrosion mix powder in a crucible for 160 hours in O_2 + 1000ppm SO_2

A very thick external NiO scale grew over an internal Cr- and Ni- rich oxide scale. The sulfur and chromium content increases with depth into the scale as with the FeNiCr and T92 alloys. At the metal/oxide interface, chromium sulfides form a layer that would penetrate and cause further attack with continued exposure to the environment. It is not known why the specimen suffered so much damage in the non-deposit zone. The edges of a specimen can be expected to corrode more due to a larger surface area, but not to this extent where there is no deposit.

The mechanism for corrosion under the tested conditions for the nickel-based alloys is not as clear as the steels. As was stated earlier, the conditions used for these tests are to simulate the environments that occur in actual coal-fired boilers. Ni-based alloys are not currently used in coal-fired boiler hardware, however with increasing temperatures and pressures, they may be needed for their increased corrosion resistance. The standard corrosion mix was determined from the stoichiometric values of the alkali iron trisulfates. This deposit was used in order to form these trisulfates on the steel alloys and cause corrosion. This same deposit was used on the nickel-based alloys, and it did cause corrosion of the specimens. The combination of the Ni-based alloys with the standard corrosion mix does not as accurately simulate the corrosion that

occurs in actual coal-fired boilers as with the steel alloys. The corrosion that is occurring with these alloys and this deposit under these conditions can possibly be described by the following mechanisms. The corrosion could be due to the reaction of the SO_3 in the gas with the Fe_2O_3 and the alkali sulfates in the deposit to form the alkali iron trisulfates, which is what the deposit was designed to do. In this case, the Fe_2O_3 comes entirely from the deposit, whereas with steels, Fe_2O_3 can come from the thermally grown oxide scale as well. Usually the liquid alkali iron trisulfates form at the expense of this thermally grown Fe_2O_3 scale, but with Ni-based alloys, this is not possible. A NiO scale also will prevent the alkali iron trisulfates from reacting with the base metal substrate, preventing serious corrosion that occurred with the steel alloys. With the formation of alkali iron trisulfates on the surface of the specimen, the corrosion mechanism could follow the mechanism proposed by Cain and Nelson[32] that was mentioned earlier, where the liquid trisulfates penetrate and reach the base metal surface through cracks or other defects in the scale. There they would react with the base metal and cause metal wastage in a reaction similar to that shown in equation 18. With this reaction, sulfides would form which was seen in the experimental results. The amount of corrosion caused by this mechanism would be less than for steels, because it requires the alkali iron trisulfates to react with the bare metal surface. There will be a protective NiO or Cr_2O_3 scale grown on the specimen surface, so the alkali iron trisulfates will have to penetrate the scale through cracks or other defects in order to get to the metal substrate. The amount of attack would be smaller and more localized than the previously described mechanism of attack for steels in which the trisulfates form on the surface at the expense of the thermally grown iron oxide scale. This could help explain why this alloy underwent less corrosion than the steel alloys.

The mechanism could also be similar to the corrosion mechanism for Type II hot corrosion. The mechanism for corrosion of Ni and Co-based alloys under Type II conditions was explained earlier. There is Na_2SO_4 in the standard corrosion mix, and along with SO_3 in the gas atmosphere, a eutectic liquid can form and cause corrosion. Although Co-based alloys are more susceptible to Type II hot corrosion, it can still occur with Ni-based alloys. This will be discussed in more detail in the Type II hot corrosion section. The appearance of sulfides at the metal/oxide interface is common for Ni- based alloys that undergo hot corrosion. The fireside corrosion mechanism for Ni-based alloys could also be a combination of corrosion occurring from alkali iron trisulfate formation and from Na_2SO_4-induced hot corrosion. A comparison of fireside corrosion and Type II hot corrosion of these alloys will be discussed in a future section.

5.1.5 IN-617

The results of the fireside corrosion test on IN-617 at 700^{o}C with the standard corrosion mix powder in a crucible for 160 hours in O_2 + 100 and O_2 + 1000ppm SO_2 are shown in Figures 54 and 55 respectively.

Figure 54: Fireside corrosion of IN-617 at 700^{o}C with the standard corrosion mix powder in a crucible for 160 hours in O_2 + 100ppm SO_2

Figure 55: Fireside corrosion of IN-617 at 700^{o}C with the standard corrosion mix powder in a crucible for 160 hours in O_2 + 1000ppm SO_2

As was the case with the Ni-22Cr alloy, there was not as much degradation as the Fe-based steel alloys. The pitting was not as severe. The alloy seems to have performed even better than the model NiCr alloy. IN-617 is also a Ni-based alloy, so its corrosion resistance should be greater than that of the steels, as was explained previously. It also has 22%Cr along with other element additions which give it its good corrosion resistance. The corrosion morphology can be seen in Figure 56. In the non-deposit zone, an oxide scale grew that consisted of external transient NiO with some Cr_2O_3 and internal Cr_2O_3. Corrosion occurred throughout the deposit zone, but as was

the case with the Ni-22Cr alloy, the most severe corrosion seems to have occurred where the deposit was the thinnest. EDS analysis showed that in the deposit zone, a thicker external NiO oxide scale grew over an internal Cr_2O_3 scale with some sulfidation penetrating into the substrate as with the Ni-22Cr alloy. Nickel-based alloys form inward penetrating sulfides, as will be seen in the Type II hot corrosion section described later. The sulfide penetration is not as pronounced as Ni-22Cr, which may be due to the Co addition. As will be seen in a later section, sulfides are not seen penetrating further into the substrate for Co-based alloys like they are for Ni-based alloys. The corrosion mechanism for IN-617 is believed to be similar to Ni-Cr.

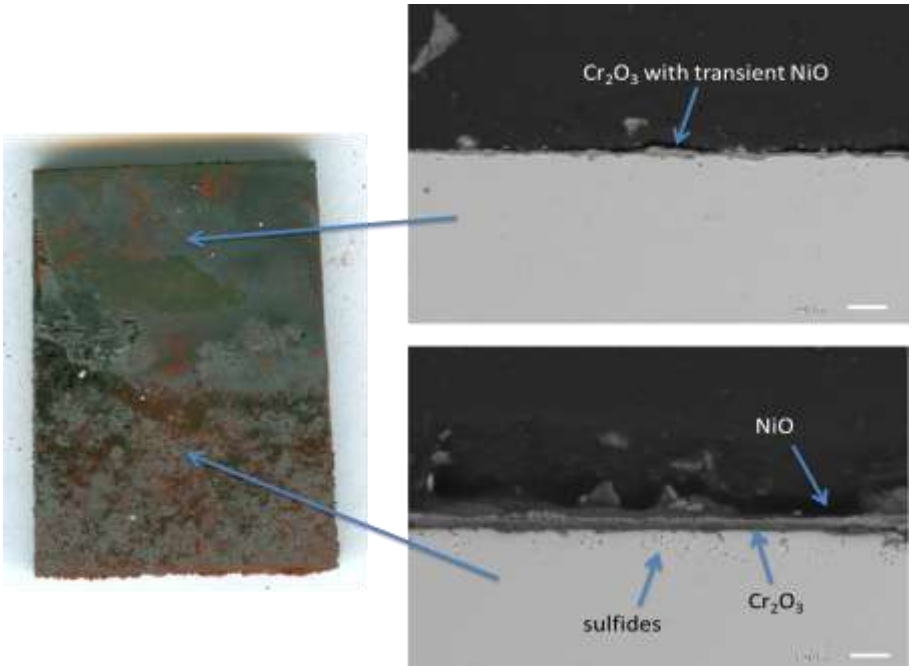

Figure 56: Fireside corrosion of IN-617 at 700°C with the standard corrosion mix powder in a crucible for 160 hours in O_2 + 1000ppm SO_2

5.1.6 NiCrAl

The results of the fireside corrosion test on NiCrAl at 700^{o}C with the standard corrosion mix powder in a crucible for 160 hours in O_2 + 100ppm SO_2 and O_2 + 1000ppm SO_2 can be seen in Figures 57 and 58 respectively.

Figure 57: Fireside corrosion of NiCrAl at 700^{o}C with the standard corrosion mix powder in a crucible for 160 hours in O_2 + 100ppm SO_2

Figure 58: Fireside corrosion of NiCrAl at 700^{o}C with the standard corrosion mix powder in a crucible for 160 hours in O_2 + 1000ppm SO_2

As was the case with the previous two nickel-based alloys, the amount of corrosion was less for NiCrAl than for the Fe-based steel alloys. NiCrAl is an alloy designed for coatings of turbine

engine hardware. It is typically an alumina former due to the "third element effect". The third element effect means that a third element, Cr in this case, is added to the alloy so that reduced amounts of the desired oxide element, Al in this case, can be added and still form a protective oxide scale. In this case, transient Cr_2O_3 grows on the surface. The oxygen partial pressure at the scale/alloy interface decreases to the dissociation pressure of Cr_2O_3 allowing only an oxide more stable than Cr_2O_3 to form. Al_2O_3 is the most stable oxide and forms a protective scale on the surface under the transient oxides. Because it is a Ni-based alloy and it can grow a Cr or Al oxide scale, NiCrAl should have rather good corrosion resistance. The corrosion morphology is shown below in Figure 59. As was the case for all of the other alloys tested, only a thin protective oxide scale consisting of transient NiO with some Al_2O_3 and Cr_2O_3 grew where there was no deposit. The entire deposit zone showed corrosion, but it appears as though more severe corrosion occurred at the non-deposit/deposit zone interface where the deposit was the thinnest, which was the case for the other alloys as well. The corrosion occurred in the form of localized pits that look like blisters forming on the surface of the specimen. This is because a thick mound-like external NiO scale grew on the surface. This turned into an internal scale with increasing Cr_2O_3, Al_2O_3, and sulfur contents with depth. Below the oxide scale at the base of the pit, chromium sulfides penetrate further into the metal substrate, which was the case with the other Ni-based alloys as well. The corrosion is similar to the pitting that occurred in the steel alloys. The composition and the presence of sulfides are also very similar to the other nickel-based alloys tested, and the corrosion mechanism should be the same as those alloys.

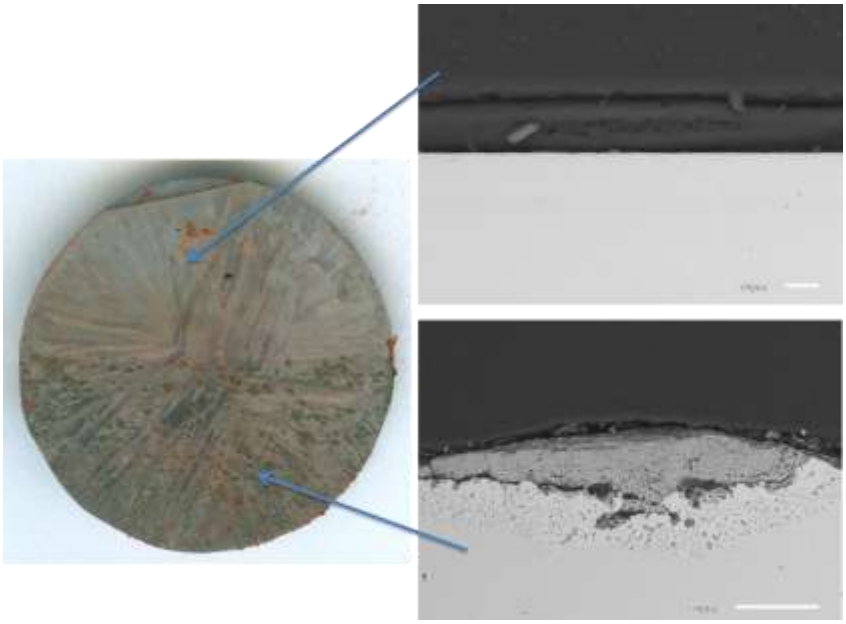

Figure 59: Fireside corrosion of NiCrAl at 700°C with the standard corrosion mix powder in a crucible for 160 hours in O_2 + 1000ppm SO_2

5.1.7 NiCrAlMo

The results of the fireside corrosion test with NiCrAlMo at 700°C with the standard corrosion mix powder in a crucible for 160 hours in O_2 + 100ppm SO_2 and O_2 + 1000ppm SO_2 can be seen in Figures 60 and 61 respectively.

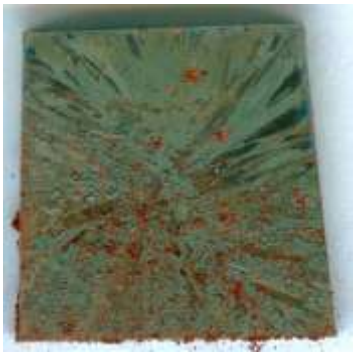

Figure 60: Fireside corrosion of NiCrAlMo at 700°C with the standard corrosion mix powder in a crucible for 160 hours in O_2 + 100ppm SO_2

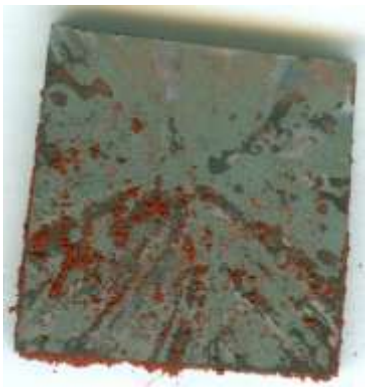

Figure 61: Fireside corrosion of NiCrAlMo at 700°C with the standard corrosion mix powder in a crucible for 160 hours in O_2 + 1000ppm SO_2

This alloy behaved similarly to the NiCrAl alloy and the other nickel-based alloys, in that it did not corrode as much as the Fe-based steel alloys. The corrosion microstructure is shown below in Figure 62. In the area where there was no deposit, a thin external NiO scale grew with some internal Al- and Cr- rich oxides. There were also some chromium sulfides penetrating into the substrate. The deposit zone corroded in a similar manner as the NiCrAl alloy. There were localized areas of pitting that could be seen as the dark areas on the macroscopic image in Figure 61. A thick NiO scale grew over pits that were rich in Ni,Cr,Al,S, and O. The sulfur content increases with depth into the pit until the base is reached where internal chromium sulfides formed and started to penetrate further into the substrate. The pitting attack is common for all of the alloys tested, and the appearance of the chromium sulfides is common with the other Ni-based alloys tested. The corrosion mechanism should be similar to that of the other Ni-based alloys as well.

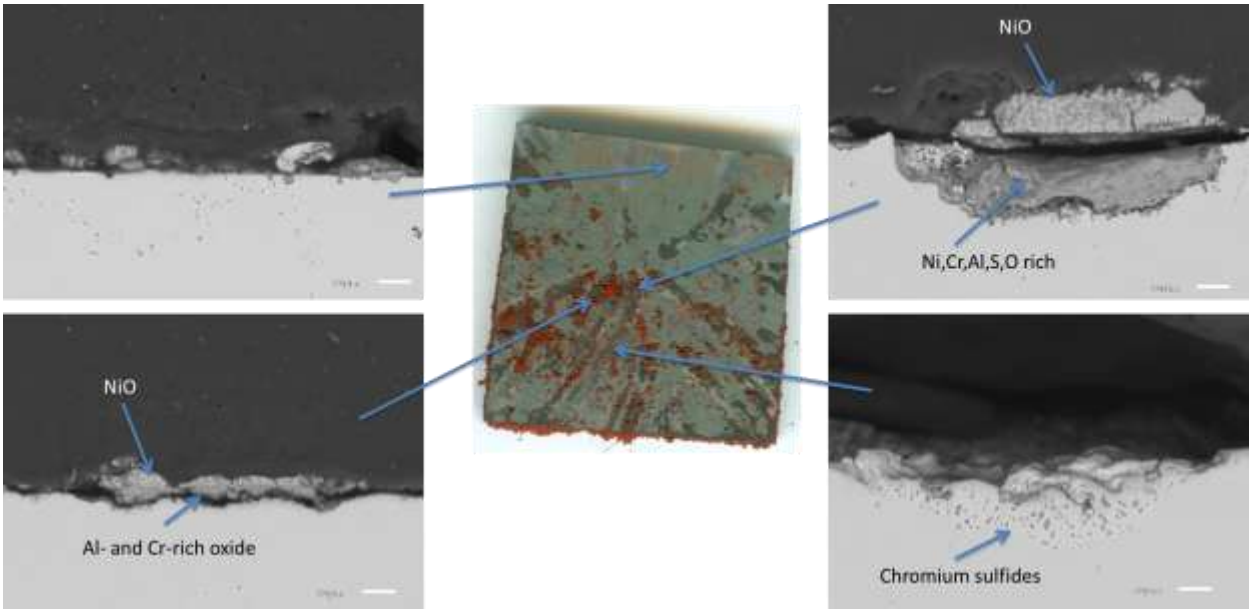

Figure 62: Fireside corrosion of NiCrAlMo at 700°C with the standard corrosion mix powder in a crucible for 160 hours in O_2 + 1000ppm SO_2

5.2 TYPE II HOT CORROSION

The Type II hot corrosion tests that will be described in this section were performed by Michael Task for his Master's Thesis at the University of Pittsburgh.[66] The results of this work will be compared to those for the performed fireside corrosion and disk corrosion tests. For his research, Michael exposed NiCrAlY and CoCrAlY alloys to the Type II hot corrosion conditions described previously in the experimental section ($p_{SO3} = 4.856\times10^{-3}$ atm) . These tests were only conducted for 10 hours. From these tests we can observe typical Type II hot corrosion microstructure. Cross-sectional images of the corrosion microstructures can be seen in Figure 63 below.[66]

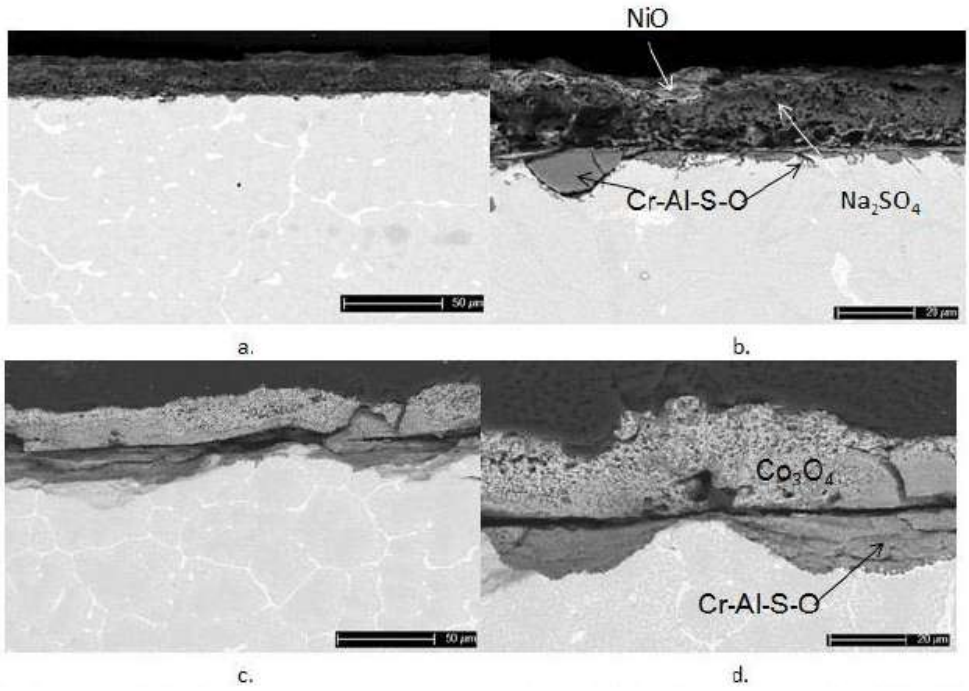

Figure 63: Type II hot corrosion microstructures: (a.-b.) NiCrAlY (c.-d.) CoCrAlY [74]

The NiCrAlY alloy did not corrode as much as the CoCrAlY alloy. A layer of Na_2SO_4 deposit can be seen still on the material, and some NiO has precipitated out to the scale/gas interface. External oxides of Ni, Cr, and Al grew on the surface, and some relatively small localized corrosion pits rich in Cr, Al, S, and O can be seen penetrating the specimen. They are not as deep compared to the CoCrAlY alloy. An oxidation/sulfidation attack occurred at the phase boundaries surrounding the alpha-Cr phase. This can be seen more clearly in Figure 64 below.[66]

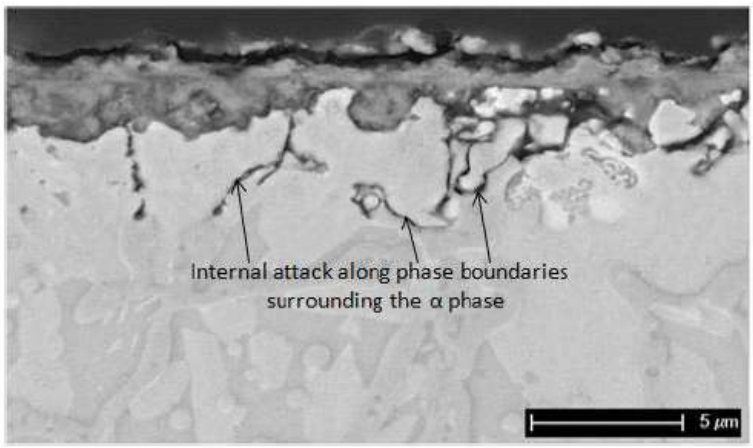

Figure 64: Type II hot corrosion microstructure of NiCrAlY demonstrating interphase attack[74]

The attack on the CoCrAlY alloy was much more severe and is typical for what has been seen in the literature for Type II hot corrosion of Co-based alloys.[59-62] There was extensive pitting rich in Cr, Al, S, and O with a layer rich in Al and S near the base of the pit. A thick Co-rich oxide layer was found over top of the pits that spalled very easily during cooling. The pitting attack seen in the images above are typical for that of Type II hot corrosion. The CoCrAlY alloy specimens corroded similarly to other cobalt based alloys tested under these Type II hot corrosion conditions in the past. The mechanism described earlier in section 2.4.3 from the work of Luthra and Chiang[62 and 64] adequately describes what occurred in the current work. The hot corrosion of metals below the melting point of Na_2SO_4 is dependent on the formation of a molten MSO_4-Na_2SO_4 eutectic. This was proven in Michael Task's PhD thesis. In his PhD thesis,[67] Michael pre-oxidized specimens and exposed them to the Type II hot corrosion conditions described earlier (pure Na_2SO_4 deposit) for 10 hours. This produced negligible corrosion because insufficient transient oxides grew following the pre-oxidation to cause a liquid eutectic melt. He had to use deposit mixtures containing Na_2SO_4-$NiSO_4$ and Na_2SO_4-$CoSO_4$, because they are already molten at 700^{o}C and do not need to react with the transient oxides to

form the liquid eutectic melt. Tests with the pre-oxidized specimens and the eutectic deposits produced localized penetration of the pre-formed Al_2O_3 oxide at Y/Hf rich regions in the scale and rapid corrosion in those areas. Without pre-oxidation and using the eutectic deposit produced severe corrosion. It was clear from these results that that pre-oxidation increased corrosion resistance and that a liquid eutectic deposit is needed for corrosion to occur. Sufficient transient oxides are needed to produce this.

CoCrAlY has less corrosion resistance to Type II degradation than NiCrAlY due to the greater stability of $CoSO_4$ than $NiSO_4$. The reaction given in equation 39 can be compared to that given below in equation 46.

$$NiO + SO_3 = NiSO_4 \qquad (46)$$

For the reaction given in equation 39, $CoSO_4$ forms from Co_3O_4 and ΔG_{700^oC} = -59.3 kJ/mol $CoSO_4$. For the reaction given in equation 46, $NiSO_4$ forms from NiO and ΔG_{700^oC} = -52.8 kJ/mol $NiSO_4$. From these values, it can be seen that $CoSO_4$ is more stable and will form at lower p_{SO3}. The solubility of MSO_4 can also be taken into account. Figure 65 shows the binary diagram for $NiSO_4$-Na_2SO_4.[30]

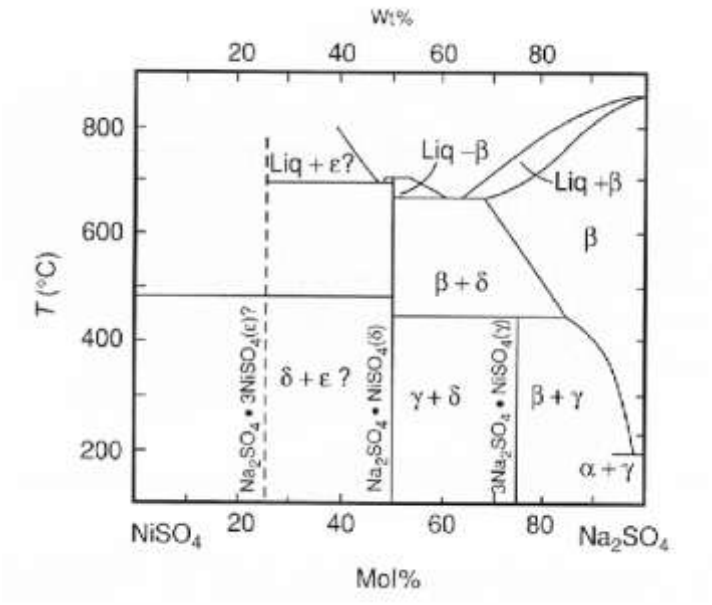

Figure 65: $NiSO_4$-Na_2SO_4 phase diagram

At 700°C, Na_2SO_4 is able to dissolve 22 mol% $NiSO_4$ before a liquid will form. Compare this with the $CoSO_4$-Na_2SO_4 phase diagram shown previously in Figure 26. According to this diagram only 19 mol% $CoSO_4$ can be dissolved before a liquid will form. Co is more stable when solubility is concerned as well, and therefore it has poorer Type II hot corrosion resistance than nickel-based alloys.

5.3 TYPE II HOT CORROSION OF DISK ALLOYS

5.3.1 Oxidation of Alloys in Air

Before any tests were conducted on the selected alloys with Na_2SO_4 deposits, each of the disk alloys was oxidized in air at 700°C for 100 hours isothermally without no deposit. This was used

as a baseline for comparison, so that the effect of the salt deposit could be determined. The results can be seen in Figure 67 below. Each of the alloys developed an extremely thin protective oxide as can be seen in the BSE micrographs. IN738 grew a very thin oxide scale consisting of NiO, Al_2O_3, and Cr_2O_3. The white areas in the substrate of the specimen are Laves phase. IN-617 and RR1000 both grew very thin oxide scales consisting of Cr_2O_3 and transient NiO. NiCrAl grew an oxide scale consisting of transient NiO over Al_2O_3. NiCrAlMo grew localized mounds of external NiO with internal Al_2O_3 underneath. It is not known exactly why there was an increase in oxidation rate for this alloy. The Mo addition could have caused this. The other Mo-containing alloys (RR1000 and IN-617) contain higher Cr and Al contents, so that the Mo addition may not have affected them as much. The oxidation microstructures shown in Figure 67 will be used for comparison with each of the following tests.

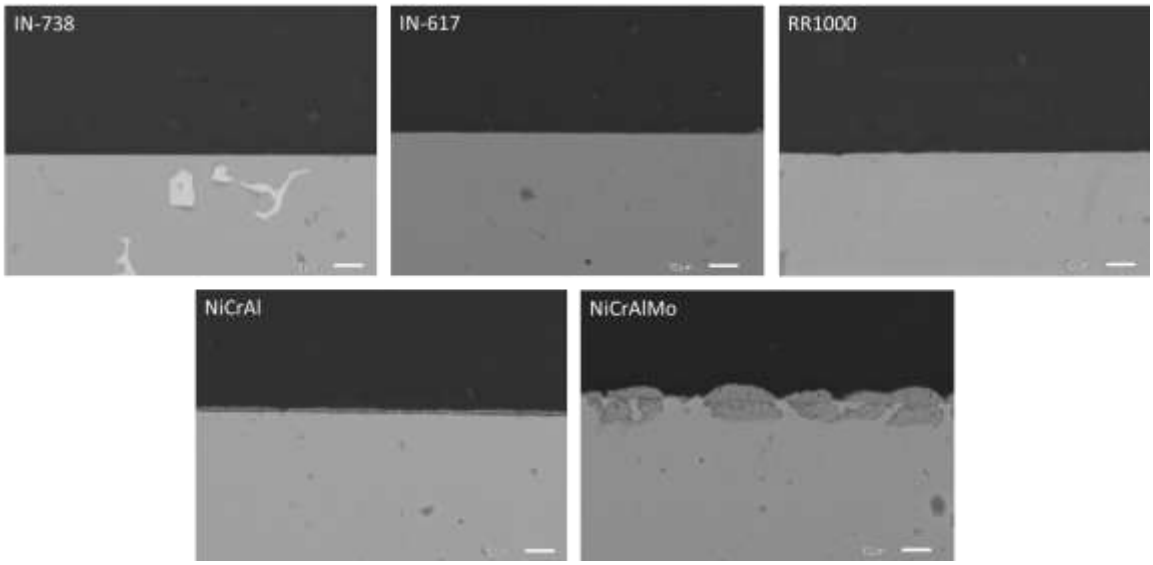

Figure 66: Cross-sections of selected disk alloys after oxidation in air

5.3.2 Oxidation of Alloys in Air with Na_2SO_4 Deposit

Each of the alloys selected was then tested at 700°C in air for 100 hours isothermally with the Na_2SO_4 deposit. The results can be seen in Figure 68 below. NiCrAl and IN-738 did not undergo any substantial attack. They grew a very thin oxide scale similar to the previous test without the deposit. There were some small localized areas of internal oxidation and sulfide penetration, but not to the extent of the other alloys tested.

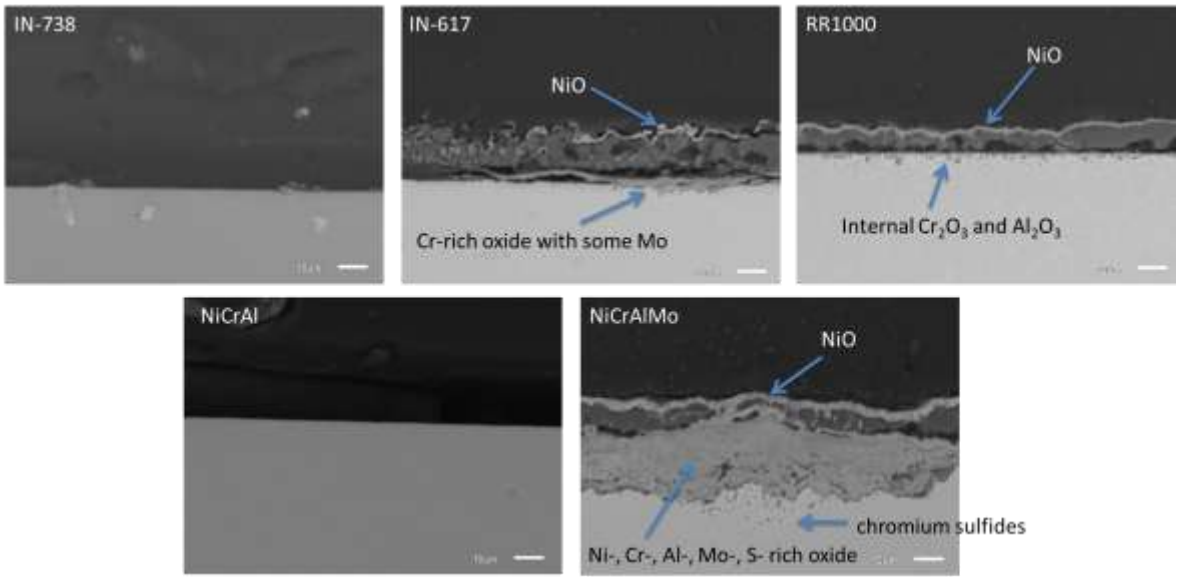

Figure 67: Oxidation of selected disk alloys in air with Na_2SO_4 deposit at 700°C

The Mo-containing alloys (NiCrAlMo, IN-617, and RR1000) produced more degradation. NiCrAlMo suffered the most corrosion as can be seen in Figure 68. A NiO scale grew on the outside over the salt deposit. An internal oxide scale grew consisting of NiO, Cr_2O_3, and Al_2O_3 with some chromium sulfides penetrating into the substrate. This appearance of internal chromium sulfides is similar to observations in previous Type II hot corrosion exposures. EDS

also indicated some Mo in the corrosion pit at the metal/oxide interface. IN-617 and RR1000 showed similar microstructures, but the degradation was not as severe. A NiO scale traveled through and formed over the deposit, which covered an internal scale of Cr_2O_3 and Al_2O_3. Traces of Mo could also be seen in the internal oxide scale. These microstructures show that the NiO is diffusing through the deposit and reforming over top of it and Mo was found at the scale/alloy interface. This is similar to a microstructure that might occur with alloy induced acidic fluxing Type I hot corrosion that was described earlier. Given enough time, it is believed that each of these three Mo-containing alloys would suffer severe degradation, and the microstructures would look like that of specimen that has undergone alloy-induced acidic fluxing. The temperatures used here are in the Type II hot corrosion range however. The presence of Mo is causing these alloys to corrode at 700^{o}C in air even without the presence of SO_3. Transient MoO_3 is possibly reacting with the salt to form sodium molybdate, releasing SO_2. This is shown by the reaction given in equation 47.

$$MoO_3 + Na_2SO_4 = Na_2MoO_4 + SO_2 + \tfrac{1}{2}O_2 \qquad (47)$$

The melting point of sodium molybdate is 687^{o}C, so at the temperature tested (700^{o}C) it becomes molten. The molten Na_2MoO_4 would then be able to penetrate the protective oxide scale and cause corrosion of the alloy substrate. The mechanism is similar to the mechanism for Type I alloy-induced acidic fluxing described earlier, and a comparison will be discussed in more detail in section 5.4.2.

To prove that it was the formation of liquid sodium molybdate could be causing the corrosion of the alloys at 700^{o}C, a test was conducted on the three Mo-containing alloys at 650^{o}C. This is below the melting point of sodium molybdate (687^{o}C), so a liquid should not form to cause severe corrosion. This was indeed the case, as can be seen from the results of this

test in Figure 69. Each of the alloys grew a thin oxide scale consisting of predominantly Cr_2O_3 and transient NiO. There were some small localized areas of internal Cr_2O_3 and Al_2O_3 growth, but the fluxing and the corrosion did not occur as at 700^oC.

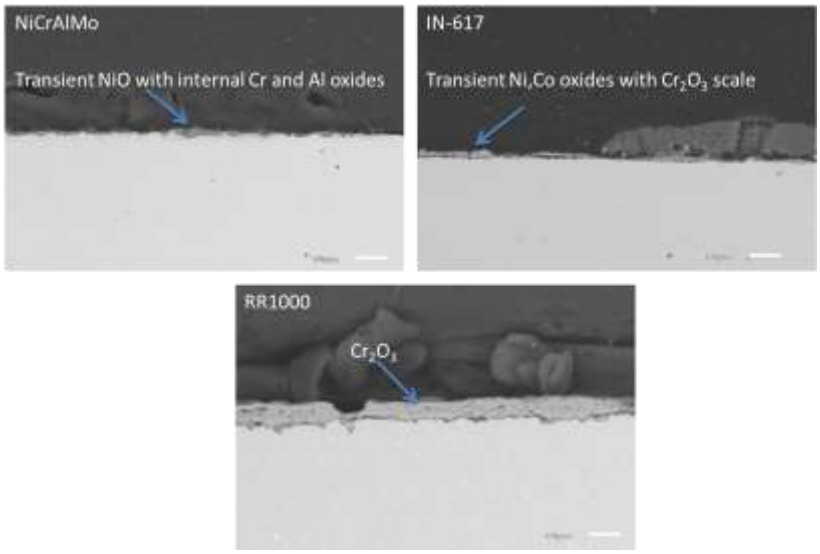

Figure 68: Oxidation of Mo-containing disk alloys in air with Na_2SO_4 deposit at 650^oC

5.3.3 Type II Hot Corrosion of Disk Alloys

The selected disk alloys were tested under the Type II hot corrosion conditions described in the experimental section (Na_2SO_4 deposit at 700^oC for 100hours isothermally in O_2 + 1000ppm SO_2). The results can be seen in Figure 70 below.

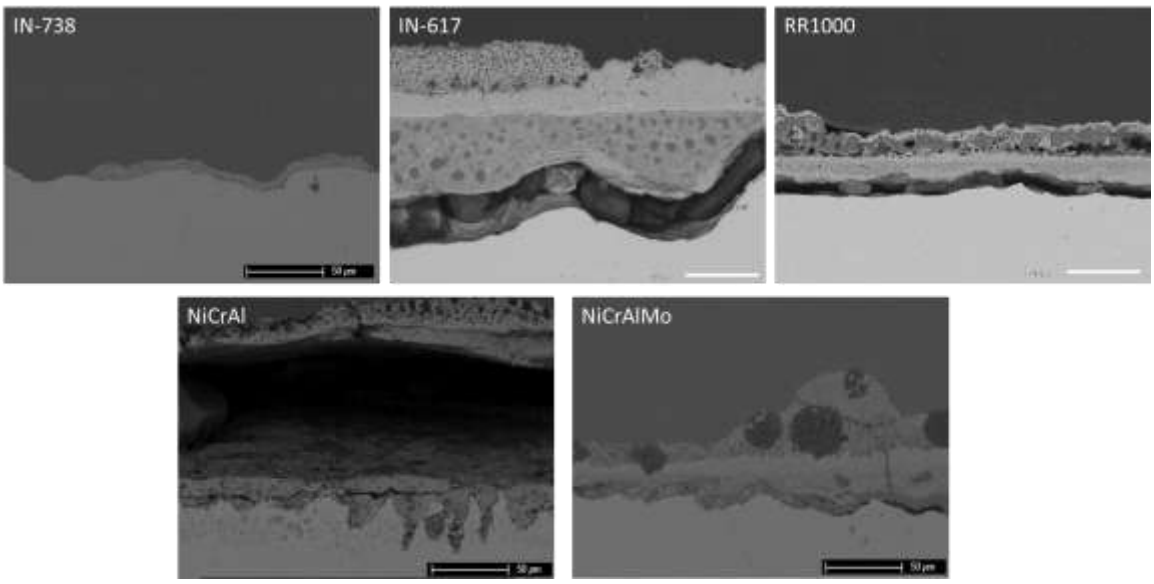

Figure 69: Type II hot corrosion of disk alloys at 700°C in O_2 + 1000ppm SO_2

The attack on each of the alloys tested was greater in an SO_2 atmosphere than when tested in air (Fig. 68). As was mentioned previously, SO_3 is required to cause the formation of the liquid eutectic Na_2SO_4-MSO_4 melt to cause Type II hot corrosion, and this appears to be more corrosive than the degradation caused on the Mo-containing alloys by the formation liquid Na_2MoO_4 in air.

The NiCrAl alloy developed a thick NiO scale that grew over top of internal oxide pits rich in Ni, Al, Cr, O, and S. The sulfur content increases with depth into the pits and chromium sulfides can be seen penetrating into the substrate. IN-738, NiCrAlMo, IN-617, and RR1000 suffered severe spallation upon cooling of the specimens. EDS analysis showed that where there was severe spallation, a layer rich in Al, S, and O remained. This is similar to the formation of the layer rich in Cr and S at the base of the pits found in previous fireside corrosion and Type II hot corrosion exposures. The spallation on the IN-738 alloy was so severe that no intact oxides or full corrosion product could be found. Where there was no spallation on the NiCrAlMo alloy,

a thick external NiO oxide scale grew with remnant Na_2SO_4 deposit intermixed into the scale. This turned into internal pits rich in Al, Cr, S, and O. The base of the pits was identical to the sulfide layer found where spallation occurred. IN-617 suffered an attack similar to the NiCrAlMo alloy, but the degradation was greater. Where the oxide had not spalled away, a thick NiO scale grew with similar circular remnant Na_2SO_4 deposits intermixed into the scale. This resulted in deeper internal pits than observed for the other alloys. These were rich in Cr, O, and S. Some circular Na_2SO_4 deposit could also be seen in the internal pits as well. At the base of the pits is a lighter region that contained large amounts of Cr and S. RR1000 also had an attack similar to IN-617 and NiCrAlMo. External NiO and Co_3O_4 grew over top of the sodium sulfate deposit. There were also internal pits rich in Cr_2O_3 and S. This is similar to what was seen in the absence of SO_2 as was described earlier. The deep pitting attack and the appearance of a sulfide layer at the base of the pits are similar to what was described for previous fireside corrosion and Type II hot corrosion tests.

The alloys that did not contain Mo were tested under Type II hot corrosion conditions, therefore the mechanism for corrosion of these alloys can also be adequately described by the Type II hot corrosion mechanisms proposed from Luthra[62] and Chiang[64] given in Section 2.4.3. The mechanism of corrosion for the alloys containing Mo can be described by a combination of the mechanisms given previously for the Mo-containing alloys in air and Type II hot corrosion. This will be described in section 5.4.3 in more detail, along with a comparison of the Type II hot corrosion of the disk alloys with that of the NiCrAlY.

5.4 COMPARISON OF THE CORROSION MICROSTRUCTURES AND MECHANSIMS

The mechanisms and characteristic microstructures of some of the various types of corrosion that can occur in coal-fired power plants and in turbine engine systems have been described in previous sections. The results of tests exhibiting these types of corrosion have also been described and compared with those found in the literature. Much of the work that was performed matched up well with the literature and with what has been seen in previous research. However, there are similarities between characteristics of different types of corrosion, or an aspect of a type of corrosion which is occurring in an environment that is not generally considered to be characteristic for that type. There may be a broader range in which we can define these different types of corrosion. We may be able to include some forms of corrosion into another. We may also need to identify new forms of corrosion that can combine characteristics from different known types. The purpose of the following sections is to compare and contrast the different types of corrosion tested for this work, and to gain a better understanding of the different corrosion mechanisms. A table summarizing the comparison of the characteristics, corrosion products, and mechanisms of each type of corrosion is shown below for reference.

Table 7: Comparison of the characteristics, corrosion products, and mechanisms for each type of corrosion tested at 700°C

Type Of Corrosion	Deposit	Liquid Melt	Gas Atmosphere	Test Duration (hours)	Corrosion Products	Corrosion Mechanism
Fireside Corrosion of Steels	K_2SO_4, Na_2SO_4, Fe_2O_3	Alkali Iron Trisulfates	$O_2 + SO_2$	160	Porous Fe_2O_3 over deep pits rich in Cr, S, and O with CrS at the base	Fireside Corrosion
Fireside Corrosion of Ni-Based Alloys	K_2SO_4, Na_2SO_4, Fe_2O_3	Alkali Iron Trisulfates or Na_2SO_4-Ni_2SO_4	$O_2 + SO_2$	160	NiO over internal scale (some times pits) rich in Cr, Al, S, and O with internal CrS	Fireside Corrosion and/or Type II Hot Corrosion
Type II Hot Corrosion of NiCrAlY and CoCrAlY	Na_2SO_4	Na_2SO_4-M_2SO_4	$O_2 + SO_2$	10	NiO or Co_3O_4 over deposit with some external Ni, Cr, Al rich oxides turning into pits rich in Al, Cr, S, and O with internal CrS in the NiCrAlY alloy	Type II Hot Corrosion
Corrosion of Mo-Containing Disk Alloys in Air	Na_2SO_4	Na_2MoO_4	Air	100	NiO over deposit with internal scale (some times pits) rich in Cr, Al, S, Mo, and O with internal CrS	Type I Hot Corrosion
Type II Hot Corrosion of Mo-Containing Disk Alloys	Na_2SO_4	Na_2MoO_4 and Na_2SO_4-Ni_2SO_4	$O_2 + SO_2$	100	Severe spallation, and NiO and Na_2SO_4 mixed over internal pits rich in Cr, S, and O with CrS at the base	Type I Hot Corrosion followed by Type II Hot corrosion
Type II Hot Corrosion of non-Mo-Containing Disk Alloys	Na_2SO_4	Na_2SO_4-Ni_2SO_4	$O_2 + SO_2$	100	Severe Spallation and NiO and Na_2SO_4 mixed over internal pits rich in Ni, Al, Cr, S, and O with CrS at the base and internal CrS	Type II Hot Corrosion

5.4.1 Fireside Corrosion and Type II Hot Corrosion

The results of the fireside corrosion tests for six different selected alloys was described in Sections 5.1.2-5.1.7, and the results from the Type II hot corrosion tests were described in sections 5.2.1-5.2.2. There were similarities in the results, even though they occur in different industrial applications. Fireside corrosion occurs in coal-fired power plants, while Type II hot corrosion usually occurs on gas turbine blade hardware. They both typically occur at temperatures near 700°C in gas atmospheres that contain sufficient amounts of SO_3 to cause corrosion. The main difference between the two is the type of deposit that is responsible for causing the liquid-phase corrosion. The deposits that form on the surface of boiler hardware and cause fireside corrosion are quite complex. They come from ash from burning coal, and can contain many different components. The main causes of corrosion in these deposits are complex sodium and potassium sulfates, which react with the gas atmosphere and the thermally grown

iron oxide scale to form liquid alkali iron trisulfates. The deposit that was used in the current research was designed to cause significant corrosion of the alloys tested. This was the standard corrosion mix which, as was stated earlier, contains K_2SO_4:Na_2SO_4:Fe_2O_3 in a 1.5:1.5:1.0 molar ratio. The corrosion environment was simulated, but it is believed that the results from these tests are relevant in describing the coal combustion atmosphere. The deposits that occur in Type II hot corrosion are also complex. Na_2SO_4 is the main contributor to corrosion and is the deposit that was used for this study. Na_2SO_4 reacts with SO_3 in the gas atmosphere and the oxide scale to form a liquid eutectic melt and causes degradation of the metal.

The typical microstructure of Type II hot corrosion can be seen in Figure 63. These are the results Michael Task obtained in exposing NiCrAlY and CoCrAlY alloys to Type II hot corrosion conditions for 10 hours. As was described earlier, the attack occurs in the form of localized pits. A thick oxide scale consisting of Ni or Co oxides, depending on the alloy formed over the corrosion pits. These oxide scales spalled easily upon cooling, and are therefore unprotective. The localized pits were rich in Al, Cr, S, and O and can be seen penetrating into the specimen. The NiCrAlY alloy produced some oxidation/sulfidation with sulfides penetrating into the substrate. The CoCrAlY alloy had a layer rich in Al and S at the base of the pits. These characteristics are similar to what occurred in the fireside corrosion tests.

The materials used in coal-fired power plants are typically steels; however the attack that occurred was in the form of pits similar to the NiCrAlY and CoCrAlY Type II hot corrosion tests. The corrosion microstructures for the fireside corrosion tests can be seen in Sections 5.1.2-5.1.7. The steel alloys produce pits that penetrate deep into the metal substrate. Just as in the Type II hot corrosion tests, a porous, non-protective scale, in this case consisting of iron oxide, formed over the pits which were more Cr, S, and O rich. The Cr and S content increased with

depth into the pits until a layer which was only rich in Cr and S formed with some internal sulfidation. This is almost exactly the same as the Type II hot corrosion tests described in the previous paragraph. The Ni-based alloys used in the fireside corrosion tests behaved somewhat similarly to the NiCrAlY alloy tested in Type II hot corrosion exposures. This can be seen in the comparison image in Figure 70 below. The corrosion was greater in the fireside corrosion tests, but this may be due to a longer duration test. Each produced Ni-rich oxide scale with some Cr- and Al oxides over top of a pit that was rich in Al, Cr, S, and O. Both also contained some internal sulfidation. The sulfides that formed in the fireside corrosion tests were more prevalent than in the Type II hot corrosion tests on NiCrAlY. There were no sulfides observed in the CoCrAlY alloy.

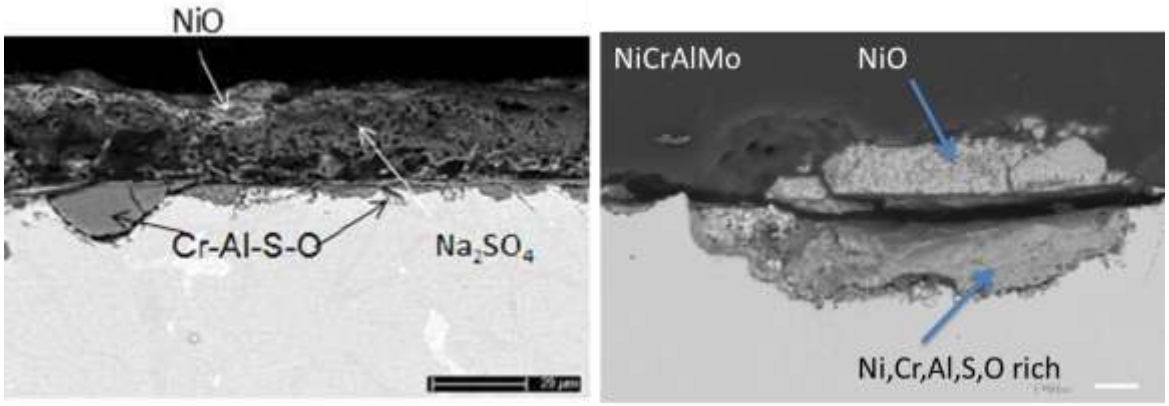

Figure 70: Comparison of type II hot corrosion of NiCrAlY to fireside corrosion of NiCrAlMo

Comparing both types of corrosion, it is easy to see that the effects of each on their respective alloy substrates are very similar. It could be argued that fireside corrosion is just a more severe form of Type II hot corrosion. Both forms of corrosion occur at the same temperature (700^{o}C) and in gas atmospheres containing SO_3. The main difference between the

two is that fireside corrosion has a more complex deposit and occurs typically on steel boiler tubes rather than Ni-based gas turbine hardware, which causes it to have a slightly different mechanism than Type II hot corrosion. The corrosion mechanisms for fireside corrosion of steel alloys and Type II hot corrosion of NiCrAlY and CoCrAlY were described in sections 2.3.2 and 2.4.3, respectively. Although the exact conditions of the two forms of corrosion are different, they both have the same effect on their respective alloy substrates. The pitting attack and the corrosion products that occur behave in a similar manner. The deposit that occurs in the fireside corrosion of steels becomes liquid due to reactions with the deposit and gas atmosphere and forms at the expense of the thermally grown transient iron oxide. This liquid penetrates to the substrate disrupting the formation of a protective scale causing corrosion. More of the harmful SO_3 in the gas atmosphere is then able to penetrate further and continue the corrosion pitting process creating further degradation. The same could be said of that for Type II hot corrosion. The deposit becomes liquid due to reactions with the deposit and the gas atmosphere and forms at the expense of the thermally grown transient nickel oxide. The liquid penetrates to the substrate disrupting the formation of a protective oxide scale and causing corrosion. More of the harmful SO_3 in the gas atmosphere can penetrate further and continue the corrosion process creating further degradation. In each form of corrosion, the SO_3 migration through the liquid deposit can be described by an $S_2O_7^{2-}/SO_4^{2-}$ exchange reaction. The SO_3 can react with Cr or Al in the metal substrate to form the inward growing corrosion pits rich in Cr_2O_3 or Al_2O_3, and CrS. Meanwhile, the formation of the porous non-protective Fe_2O_3 scale that occurred for fireside corrosion could be occurring via a $3Fe^{2+}/2Fe^{3+}$ exchange reaction similar to what occurs in Co for Type II hot corrosion. Because of the similar effects of the liquid deposit on the metal substrates, the corrosion products and microstructures are similar. Fireside corrosion of steels

appears to be more severe, and this may be due to the fact that the Ni-based alloys used in gas turbine hardware are typically more corrosion resistant than the steel alloys used in boiler hardware due to higher chromium contents and slower growing, more protective scales. The growth rate of NiO is slower than that of Fe-oxides.

The fireside corrosion tests on the Ni-based alloys also showed similar results to the Type II hot corrosion of the MCrAlY alloys as was described previously. The possible mechanisms for fireside corrosion of Ni-based alloys were described in section 5.1.4. The mechanism could be a combination of corrosion due to the formation of liquid alkali iron trisulfates (fireside corrosion) and corrosion due to the formation of liquid Na_2SO_4-$NiSO_4$ (Type II hot corrosion). This is due to the fact that the standard corrosion mix is designed to form liquid alkali iron trisulfates, but it also has Na_2SO_4 in the deposit that can form the liquid Na_2SO_4-$NiSO_4$ eutectic, and each of these would cause corrosion.

5.4.2 Corrosion of Mo-Containing Disk Alloys in Air and Alloy-Induced Acidic Fluxing Type I Hot Corrosion

Tests were conducted on Mo-containing disk alloys (NiCrAlMo, IN-617, and RR1000) at 700^{o}C with a sodium sulfate deposit in air for 100 hours. As was mentioned earlier, the alloys underwent some degradation even though the gas atmosphere was only air and did not contain any SO_2. The results from this test can be seen in Figure 68. The corrosion microstructures are somewhat similar to what may be seen for alloy-induced acidic fluxing Type I hot corrosion. A typical alloy-induced acidic fluxing Type I hot corrosion microstructure at 900^{o}C is shown below for Ni-8Cr-6Al-6Mo in Figure 71 compared to the results from the current tests.

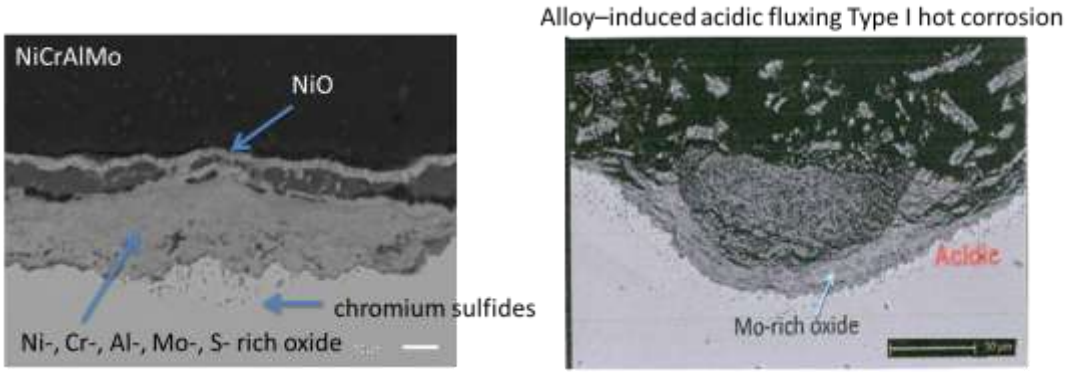

Figure 71: Comparison of corrosion of NiCrAlMo with a Na_2SO_4 deposit at 700°C in air to type I hot corrosion at 900°C [66]

In both images, a non-protective NiO scale can be seen either reprecipitated outside of the deposit or making its way through the melt. Below the deposit an internal corrosion pit rich in Cr-, Al-, Mo-, S-, and O can be seen. The appearance of Mo-rich oxides at the alloy/oxide interface is a key characteristic of alloy-induced acidic fluxing. The Mo-rich oxide is more pronounced on the alloy-induced acidic fluxing image, but Mo-rich oxide was detected in both cases. The degradation is also much greater for the Type I hot corrosion image, however this test was conducted at 900°C. The degradation caused by alloy-induced acid fluxing at 900°C appears to be greater than that caused by the Na_2SO_4-induced hot corrosion of Mo-containing alloys at 700°C in air.

The Type I hot corrosion mechanism for alloy-induced acidic fluxing was described in section 2.4.2.2. It was first incorrectly thought by Bornstein et al.[58] that transient acidic MoO_3 was reacting with the Na_2SO_4 salt deposit creating sodium molybdate and releasing SO_2 given by the reaction in equation 47. The released SO_2 would then dissolve the protective oxide scale, which is shown in the reaction given in equation 36 ($Al_2O_3 + 3SO_2 + 3/2\ O_2 = Al_2(SO_4)_3$). The amount of SO_2 released would have to be large in order for this to occur, but a sufficient amount of released SO_2 to cause equation 36 was not observed. This mechanism was therefore

concluded to be inaccurate. It was determined that at this temperature (900-1000^{o}C), transient MoO_3 becomes molten and is able to penetrate the protective oxide scale causing corrosion of the alloy substrate. The MoO_3 reduces the activity of the oxide ions in the Na_2SO_4 deposit enough so that the melt becomes highly acidic at the alloy/salt interface enabling equation 36 to occur and causing fluxing of the oxide scale. MoO_3 is found at the alloy/oxide interface, and the corrosion is initiated there because these are the regions that are the most acidic and cause a "negative solubility gradient" satisfying the Rapp-Goto Criterion for self-sustaining hot corrosion attack. The protective oxide metal ions migrate down the solubility gradient and are reprecipitated as a porous non-protective scale at the salt/gas interface where the p_{O2} is higher. This is the mechanism that adequately describes alloy-induced acidic fluxing.

The mechanism that could be occurring for the Mo-containing disk alloys at 700^{o}C with a Na_2SO_4 deposit in air can be described by a combination of the first incorrect mechanism described in the previous paragraph and the actual mechanism for alloy-induced acidic fluxing at 900^{o}C. Transient MoO_3 reacts with the salt deposit to form Na_2MoO_4 releasing SO_2 and oxygen as shown in the reaction given by equation 47. Sodium molybdate is molten under Type II hot corrosion temperatures (700^{o}), and is therefore able to penetrate the scale and cause the observed corrosion of the substrate. As was the case with the molten MoO_3 that occurs at 900^{o}C for alloy-induced acidic fluxing, the formation of molten Na_2MoO_4 causes the melt to become highly acidic at the alloy/salt interface establishing a "negative solubility gradient" and enabling equation 36 to occur, causing fluxing of the oxide scale. The appearance of Mo at the base of the corrosion pits indicates that the corrosion is initiated at these regions for this type of corrosion as well. The released SO_2 that occurs from the formation of sodium molybdate could be the cause

of the formation of internal sulfides that occurred. The tests performed at 650°C, below the melting point of sodium molybdate, which produced no severe corrosion, prove that Na_2MoO_4 is becoming liquid at 700°C and could be causing the observed corrosion.

Both the microstructures and the corrosion mechanisms are very similar for these two types of corrosion. It appears that Mo-containing Ni-based disk alloys with a Na_2SO_4 deposit can undergo alloy-induced acidic fluxing in air even at 700°C. The conditions needed for alloy-induced acidic fluxing hot corrosion may not be as clearly defined as previously thought. It appears as though it is possible for it to occur at lower temperatures on Mo-containing alloys under the right conditions.

5.4.3 Corrosion of Disk Alloys in SO_2 and Type II Hot Corrosion

The corrosion of disk alloys under Type II hot corrosion conditions was described in section 5.3.3. The results can be seen in Figure 70. These alloys suffered corrosion similar to that of the Type II hot corrosion tests on the NiCrAlY alloy in section 5.2.1. The results of those tests can be seen in Figure 65. The attack on the disk alloys is similar to the test on the NiCrAlY alloy; however the pitting and the corrosion appear to be much more severe. This may be due to the difference in the test durations, or depending on the alloy, it may be due to the mechanism of attack. The disk alloy specimens developed a thick, non-protective NiO external scale with remnant Na_2SO_4 mixed into the scale. This turned into internal pits rich in Al, Cr, S, and O, depending on the alloy, along with a layer rich in S and some internal sulfidation at the base of the pits. This is similar to what was described for Type II hot corrosion of NiCrAlY, and the pitting attack is the same as the results found for fireside corrosion of steels, which can be found in sections 5.1.2 and 5.1.3.

The corrosion mechanism for the disk alloys is dependent on the alloy. The disk alloys that do not contain molybdenum had the same deposit and were tested under the same conditions as the Type II hot corrosion of NiCrAlY, so it is expected that their corrosion products and attack would be similar. The mechanism for the corrosion of the non-Mo-containing disk alloys can therefore be adequately described by the proposed Type II hot corrosion mechanisms described in section 2.4.3 by Luthra and Chiang et al. [62, 64] The corrosion products are similar and the mode of attack is the same, therefore the corrosion of disk alloys that do not contain Mo under Type II hot corrosion conditions can be correctly labeled as Type II hot corrosion.

The disk alloys that contain Mo were more severely attacked than the other disk alloys and the Type II hot corrosion test on NiCrAlY. They even resembled the pitting attack that occurred for fireside corrosion. The mechanism of attack for these alloys is more complex. As was mentioned in the previous section (5.4.2), Mo containing alloys can undergo degradation at 700^{o}C in air without the presence of SO_3. This was due to the fact that transient MoO_3 reacts with Na_2SO_4 to form liquid Na_2MoO_4, which causes corrosion. The reaction is described by equation 47. This same type of degradation can occur for the Mo-containing disk alloys in the O_2 + SO_2 atmosphere at the start when the p_{SO3} is low, but when sufficient amounts of SO_3 fill the gas atmosphere, the form of attack changes to that for Type II hot corrosion that was described in the previous paragraph. The reaction in equation 47 ($MoO_3 + Na_2SO_4 = Na_2MoO_4 + SO_2 + ½O_2$) will proceed to the right. The SO_2 and O_2 on the right hand side of the equation will react to create SO_3, and once sufficient SO_3 has been formed, the reaction will go the other way and proceed to the left allowing Type II hot corrosion to occur. The corrosion mechanism will go from one form to another due to changes in the gas atmosphere. This may be the reason that these alloys suffered more corrosion than the Type II hot corrosion attack of NiCrAlY and

the disk alloys that do not contain Mo. This form of corrosion can be considered a combination of low temperature alloy-induced acidic fluxing hot corrosion and Type II hot corrosion, depending on how much SO_3 is in the gas atmosphere.

5.5 CONCLUSIONS

Tests were conducted under fireside corrosion conditions varying different test atmosphere variables on a model austenitic steel alloy in order to determine the environment that causes the most severe corrosion. Selected steel and Ni-based alloys were then tested under these determined highly corrosive fireside corrosion conditions. Tests were also conducted on selected Mo-containing and non-Mo-containing Ni-based disk alloys in air and under Type II hot corrosion conditions. The effect of alloy composition on the resistance to degradation as well as the corrosion mechanisms was described. The products and mechanisms of the different types of corrosion for the various types alloys were compared along with Type II hot corrosion tests on NiCrAlY and CoCrAlY alloys that were conducted by Michael Task.[66]

The most corrosive fireside corrosion test environment for the FeNiCr alloy was determined to be at 700^{o}C with the standard corrosion mix powder in crucibles for 160 hours in 20 hour cycles in an O_2 + 1000ppm SO_2 (p_{SO3} = 4×10^{-3} atm) gas atmosphere. There is a determined bell-shaped curve for which the largest amount of degradation under fireside corrosion conditions will occur. The temperature at which the bell-shaped curve is the highest and therefore the corrosion is the highest was found not to be at 650^{o}C but closer to 700^{o}C. It

was also determined that there is a threshold level of SO_2 in the gas atmosphere needed to oxidize sufficient amounts of SO_3 to allow the formation of alkali iron trisulfates, which can cause significant corrosion.

Each of the alloys suffered pitting attack. The steel alloys degraded much more severely than the Ni-based alloys. This is as expected, because the Ni-based alloys are typically more corrosion resistant than Fe-based alloys due to slower oxide growth rates, and the Ni-based alloys also had more Cr, which was found to be extremely beneficial for corrosion resistance. The SO_2 threshold level for corrosion was determined to be around 100ppm based on the results from the steel alloys. The mechanism for fireside corrosion of the steel alloys is similar to that proposed by Reid[14] described in section 2.3.2.2. The mechanism for fireside corrosion of Ni-based alloys is more complex. The corrosion may be due to the formation of liquid alkali iron trisulfates in the deposit from reactions of the gas atmosphere with the deposit, or it may be due to Na_2SO_4-induced hot corrosion due to reactions between transient NiO, Na_2SO_4 in the deposit, and the gas atmosphere. It may also be a combination of both.

The fireside corrosion tests were compared to the Type II hot corrosion of NiCrAlY and CoCrAlY tests performed by Michael Task. The degradation was more severe for fireside corrosion than for Type II hot corrosion of the MCrAlY alloys, but the corrosion products and the form of attack on the alloys were found to be very similar. The temperature and gas atmospheres used for both tests were the same, with the only difference coming from the type of deposit. Fireside corrosion uses a more complex deposit that forms liquid alkali iron trisulfates, while Type II hot corrosion uses a Na_2SO_4 deposit that forms liquid Na_2SO_4-M_2SO_4. This causes the exact mechanism of attack to be different, but the effect the deposits have on the alloys is the same. The liquid melt is formed from reactions with the deposit and the gas atmosphere at the

expense of grown transient oxides. SO_3 migrating through the liquid melt is then able to cause severe corrosion in the form of a pitting attack. The porous non-protective iron oxide scale that forms for fireside corrosion of steels can occur due to an $3Fe^{2+}/2Fe^{3+}$ exchange reaction similar to that for cobalt for Type II hot corrosion. It was determined that fireside corrosion of steel alloys is just a more severe form of Type II hot corrosion of MCrAlY alloys.

The Mo-containing Ni-based disk alloys suffered some corrosion in an air atmosphere even without the presence of SO_2, while those that do not contain Mo did not. The attack was similar to what would be seen for alloy-induced acidic fluxing Type I hot corrosion at 900°C, with Ni moving through the liquid deposit and forming NiO over top of it and Mo rich layer found at the base of corrosion pits. It was determined that Mo-containing disk alloys can suffer Type I alloy-induced acidic fluxing attack at 700°C in air. Transient MoO_3 can react with the Na_2SO_4 salt deposit to form Na_2MoO_4 (T_m = 687°C), which is liquid at this temperature. The liquid sodium molybdate then causes acidic corrosion similar to what would occur for alloy-induced acidic fluxing at 900°C. The reaction that forms sodium molybdate also releases SO_3 which can enhance then acidic fluxing of the protective oxide.

Each of the selected disk alloys was exposed to Type II hot corrosion conditions. The alloys had severe spallation upon cooling, but where there was not spallation, a pitting attack similar to what was seen with fireside corrosion and Type II hot corrosion of the MCrAlY alloys performed by Michael Task occurred. The degradation was more severe than the attack on the Mo-containing alloys in air. The mechanism for corrosion of the disk alloys was found to be dependent on alloy composition and gas atmosphere. Because the conditions were exactly the same, the mechanism for the corrosion of the alloys that do not contain Mo can adequately be described by the mechanism for Type II hot corrosion of MCrAlY alloys, and they can therefore

be categorized as the same thing. The corrosion of the Mo-containing alloys was found to be a combination of the alloy induced acidic fluxing mechanism described previously with the mechanism for Type II hot corrosion of MCrAlY alloys. It begins as alloy-induced acidic fluxing, and once enough SO_3 has entered the gas atmosphere, the reaction shifts the other way and Type II hot corrosion occurs.

BIBLIOGRAPHY

1. Stein-Brzozowska, G., Maier, J., Scheffknecht, G., *Impact of Oxy-Fuel Combustion on the Corrosion Behavior of Advanced Austenitic Superheater Materials.* Energy Procedia, 2011. 4: p. 2035-2042.

2. Syed, A.U., Simms, N.J., Oakey, J.E., *Fireside Corrosion of Superheaters: Effects of air and oxy-firing of coal and biomass.* Fuel, 2011.

3. Stringer, J., Wright, I.G., *Current Limitations of High-Temperatures Alloys in Practical Applications.* Oxidation of Metals, 1995. 44: p. 265-308.

4. Gagliano, M.S., Hack, H., Stanko, G., *Fireside Corrosion Resistance of Proposed USC Superheater and Reheater Materials: Laboratory and Field Test Results.* Presented at the 33th International Technical Conference on Coal Utilization and Fuel Systems, 2008.

5. Reid, W.T., Cohen, P. Trans. ASME, 1944. 66: p. 685.

6. Ely, F.G., Schueler, L.B., Furn. Perf. Factors Suppl. To Trans. ASME, 1944. 66: p. 23.

7. Bishop, R.J., J. Inst. Fuel, 1968. 41: p. 51-65.

8. Simms, N.J., Kilgallon, P.J., Oakey, J. E., *Fireside Issues in Advanced Power Generation Systems.* Energy Materials, 2007. 2: p. 154-160.

9. Otsuka, N., *Effects of fuel impurities on fireside corrosion of boiler tubes in advanced power generating systems – a thermodynamic calculation of deposit chemistry.* Corrosion Science, 2002. 44: p. 265-283.

10. Srivastava, S.C., Godiwalla, K.M., Banerjee, M.K., *Fuel Ash Corrosion of Boiler and Superheater Tubes.* Journal of Materials Science, 1997. 32: p. 835-849.

11. Yan, L., Gupta, R.P., Wall, T.F., *A Mathematical Model of Ash Formation During Pulverized Coal Combustion.* Fuel, 2002. 81: p. 337-344.

12. Tomeczek, J., Palugniok, H., *Kinetics of Mineral Matter Transformation During Coal Combustion.* Fuel, 2002. 81: p. 1251-1258.

13. Nelson, H.W. et al., *A Review of Available Information on Corrosion and Deposits in Coal- and Oil-Fired Boilers and Gas Turbines.* ASME, 1959. p. 7-12.

14. Reid, W.T., *External Corrosion and Deposits Boilers and Gas Turbines.* 1971, New York: American Elsevier Publishing Company, Inc.

15. Gluskoter, H.J., *Mineral Matter and Trace Elements in Coal.* American Chemical Society, 1975.

16. Smith, E.J.D., J. Inst. Fuel, 1956. 29: p. 253.

17. Natesan, K., Purohit, A., Rink, D.L., *Fireside Corrosion of Alloys for Combustion Plants.* Proc. 16th Annual Conference on Fossil Energy Materials, Baltimore, MD, April 22-24, 2002.

18. Hack, H., Stanko, G., *Experimental Results for Fireside Corrosion Resistance of Advanced Materials in Ultra-Supercritical Coal-Fired Power Plants.* Presented at the 32nd International Technical Conference on Coal Utilization & Fuel Systems, 2007.

19. Goebel, J.A., Pettit, F.S., Goward, G.W., *Mechanisms for the Hot Corrosion of Nickel-Base Alloys.* Metallurgical Transactions, 1973. 4: p. 261-278.

20. Goebel, J.A., Pettit, F.S., *Na_2SO_4-Induced Accelerated Oxidation (Hot Corrosion) of Nickel.* Metallurgical Transactions, 1970. 1: p. 1943-1955.

21. Levy, A., Merryman, E.L., Reid, W.T., *Mechanisms of Formation of Sulfur Oxides in Combustion.* Environmental Science and Technology, 1970. 4: No. 8 p. 653-662.

22. Dooley, A., Whittingham, G., Trans. Faraday Soc., 1942. 42: p.354.

23. Levy, A., Merryman, E.L., Combus. Flame, 1965. 9: p. 229.

24. Harlow, W.F., *Causes of High Dewpoint Temperatures in Boiler Flue Gases.* Proceedings of the Institution of Mechanical Engineers, 1944. 151: p. 293.

25. Cain Jr., C., Nelson, W., Trans. ASME, J. Eng. Power, 1967. 83 Series A: p. 468.

26. Corey, R.C., Cross, B.J., Reid, W.T., Trans. ASME, 1945. 67: p. 289.

27. Levy, A., Merryman, E.L., Trans. ASME, J. Eng. Power, 1967. 89 Series A: p. 297.

28. Coats, A.W., Dear, D.J.A., Penfold, D., J. Inst. Fuel, 1968. 41: p. 129.

29. Blough, J.L., *Fireside Corrosion Testing of Candidate Superheater Tube Alloys, Coatings, and Claddings – Phase II Field Testing.* Foster Wheeler Topical Report for Oak Ridge national Laboratory, 1996.

30. Birks, N., Meier, G.H., Pettit, F.S., *Introduction to the High Temperature Oxidation of Metals*. 2 ed2006, New York: Cambridge University Press.

31. Burrows, B.W., Hills, G.J., J. Inst. Fuel, 1966. 39: p. 168.

32. Cain Jr., C., Nelson, W., Trans. ASME, J. Eng. Power, 1961. 83 Series A: p. 468.

33. Corey, R.C., Grabowski, H.A., Cross, B.J., Trans. ASME, 1949. 71: p. 951.

34. Shi, L., Zhang, Y., Shih, S., *The Effect of K_2SO_4 Additive in Na_2SO_4 Deposits on Low Temperature Hot Corrosion of Iron-Aluminum Alloys.* Oxidation of Metals, 1992. 33: p. 385-405.

35. Viswanathan, R., Henry, J.F., Tanzosh, J., Stanko, G., Shingledecker, J., Vitalis, B., Purgert, R., *U.S. Program on Materials Technology for Ultra-Supercritical Coal Power Plants.* Journal of Materials Engineering and Performance, 2005. 14: p. 281-292.

36. Chi, C., Yu, H., Xie, X., *Advanced Austenitic Heat-Resistant Steels for Ultra-Supercritical (USC) Fossil Power Plants.* Alloy Steel – Properties and Use. p. 171-200.

37. Latham, E.P., Flatley, T., Morris, C.W., *Corrosion Resistant Materials for Coal Conversion Systems.* Applied Science Publishers. London, 1983. p. 137-158.

38. McCreath, C.G., *Hot Corrosion Site Environment in Gas Turbines.* Mater. Sci. and Technol., 1987. 3: p. 494-500.

39. Bornstein N.S., A., W.P., *The Chemistry of Sulfidation Corrosion-Revisited.* Mater. Sci. Forum, 1997. 127: p. 127-134.

40. Luthra, K.L., *Low Temperature Hot Corrosion of Cobalt-Base Alloys: Part I. Morphology of the Reaction Product.* Metallurgical Transactions A, 1982. 13: p. 1843-1852.

41. Giggins, C.S., Pettit, F.S. , *Hot Corrosion Degradation of Metals and Alloys - A Unified Theory*, 1979.

42. Deodeshmukh, V., Gleeson, B. *Environmental and Compositional Effects on the Hot-Corrosion Behavior of Ni-Based Alloys and Coatings*. in *Corrosion 2008*. New Orleans, LA: NACE International.

43. Inman, D., Wrench, N.S., *Corrosion in Fused Salts.* Brit. Corros. J., 1966, 1: p. 246-250.

44. Rapp, R.A., *Chemistry and Electrochemistry of the Hot Corrosion of Metals.* Corrosion, 1986. 42: p. 568-577.

45. Gupta, D.K., Rapp, R.A., *The Solubilities of NiO, Co3O4, and Ternary Oxides in Fused Na2SO4 at 1200°K.* J. Electrochem. Soc., 1980. 127: p. 2194-2202.

46. Jose, P.D., Gupta, D.K., Rapp, R.A., *The Solubility of α-Al2O3 in Fused Na2SO4 at 1200°K.* J. Electrochem. Soc., 1985. 132: p. 735-737.

47. Shi, D.Z., Rapp, R.A. , *The Solubility of SiO2 in Fused Na2SO4 at 900°C.* J. Electrochem. Soc., 1986. 133: p. 849-580.

48. Deanhardt, M.L., Stern, K.H., *Solubility Products of Metal Oxides in Molten Salts by Coulometric Titration of Oxide Ion Through Zirconia Electrodes.* J. Electrochem. Soc., 1982. 128: p. 2577-2582.

49. Rapp, R.A., Ostuka, N., *The Role of Chromium on the Hot Corrosion of Metals.* ECS Transactions, 2009. 16(49): p. 271-282.

50. Zhang, Z.S., *Solubilities of Cr2O3 in Fused Na2SO4 at 1200K.* J. Electrochem. Soc., 1986. 133: p. 655-657.

51. Zhang, Z.S., Rapp R.A., *Solubility of α-Fe2O3 in Fused Na2SO4 at 1200K.* J. Electrochem. Soc., 1985. 132: p. 734-735.

52. Rapp, R.A., Goto, K.S., *The Hot Corrosion of Metals by Molten Salts.* The Second International Symposium on Molten Salts, 1981.

53. Bornstein, N.S., DeCrescente, M.A., *The Relationship Between Compounds of Sodium and Sulfur and Sulfidation.* Trans. TMS AIME, 1969. 245: p. 1947-1952.

54. Rapp, R.A., *Hot Corrosion of Materials: A Fluxing Mechanism?*. Corrosion Science, 2002. 44: p. 209-221.

55. Pettit, F.S., Goebel, J.A., Goward, G.W., Corrosion Sci., 1969. 9: p.903-913.

56. Goebel, J.A., Pettit, F.S., *The Influence of Sulfides on the Oxidation Behavior of Nickel-Base Alloys*. Metallurgical Transactions, 1970. 1: p. 3421-3429.

57. Bornstein, N.S., DeCrescente, M.A., *The Role of Sodium in the Accelerated Oxidation Phenomenon Termed Sulfidation.* Metallurgical Transactions, 1971. 2: p. 2875-2883.

58. Bornstein, N.S., DeCrescente, M.A., Roth, H.A. *Accelerated Corrosion in Gas Turbine Engines*. *In Gas Turbine Materials Conference*. 1972. Washington, D.C.

59. Wortman, D.J., Fryxell, R.E., Luthra, K.L., Bergman, P.A., *Mechanism of Low-Temperature Hot Corrosion: Burner Rig Studies.* Thin Solid Films, 1979. 64: p. 281-288.

60. Luthra, K.L., Shores, D.A., *Mechanism of Na2SO4 Induced Corrosion at 600°-900°C.* J. Electrochem. Soc., 1980. 127: p. 2202-2210.

61. Barkalow, R.H., Goward, G.W., *Microstructural Features of Low Temperature Hot Corrosion in Nickel and Cobalt Base MCrAlY Coating Alloys.* R.A. Rapp, Editor 1983, National Society of Corrosion Engineers: Houston. p. 502-506.

62. Chiang, K.T., Pettit, F.S., Meier, G.H., *Low Temperature Hot Corrosion.* R.A. Rapp, Editor 1983, National Society of Corrosion Engineers: Houston. p. 519-530.

63. Jones, R.L., *Cobalt Oxide-SO_2/SO_3 Reactions in Cobalt-Sodium Mixed Sulfate Formation and Low Temperature Hot Corrosion.* R.A. Rapp, Editor 1983, National Society of Corrosion Engineers: Houston. p. 513-518.

64. Luthra, K.L., *High Temperature Hot Corrosion of Cobalt-Base Alloys: Part II. Reaction Mechansim.* Metallurgical Transactions A, 1982. 13: p. 1853-1864.

65. Encinas-Oropesa, A., Simms, N.J., Nicholls, J.R., Drew, G.L., Leggett, J., Hardy, M.C., *Evaluation of Oxidation Related Damage Caused to a Gas Turbine Disc Alloy Between 700 and 800^oC.* Materials At High Temperatures, 2009. 26(3): p. 241-249.

66. Task, M.N., *The Effects of Composition and Microstructure on the Reaction Behavior of MCrAlY Alloys Under A Variety of Aggressive Environmental Conditions*. Master's Thesis, University of Pittsburgh. November, 2009.

67. Task, M.N., *Assessment of the Factors Affecting Protective Alumina Formation Under Hot Corrosion Conditions*. Ph.D. Thesis, University of Pittsburgh. May 2012.

68. Niles, W.D., Siegmund, C.W., *The Mechanism of Corrosion by Fuel Impurities,* Butterworths, London, 1963. p. 332-346.

69. Corey, R.C., Cross, B.J., and Reid, W.T., Trans. ASME, 1945. 67: p. 289.